

THREE-DIMENSIONAL STRESS FIELDS AND SLIP SYSTEMS FOR SINGLE  
CRYSTAL SUPERALLOY NOTCHED SPECIMENS

By

SHANNON M. MAGNAN

A THESIS PRESENTED TO THE GRADUATE SCHOOL  
OF THE UNIVERSITY OF FLORIDA IN PARTIAL FULFILLMENT  
OF THE REQUIREMENTS FOR THE DEGREE OF  
MASTER OF SCIENCE

UNIVERSITY OF FLORIDA

2002

I would like to dedicate this work to my family here in Gainesville, Creekside Community Church, whose members have taught me many things I could not have learned in school.

## ACKNOWLEDGMENTS

I would like to thank my advisor, Dr. Nagaraj Arakere, and Dr. Fereshteh Ebrahimi for providing much-needed background information, guidance and encouragement. The work presented here is not only my own, but a collaboration with these two professors and another student, Luis Forero. Luis' experimental work was of great help, and also made me appreciate the advantages of computer modeling. Thanks are also due to my roommate, Jen, for putting up with me and for culturing me through bizarre movies and plays over the last two years. Finally, I thank God for leading me here and sustaining me each day; I hope this work is worthy.

## TABLE OF CONTENTS

	<u>Page</u>
ACKNOWLEDGEMENTS.....	iii
TABLE OF CONTENTS.....	iv
LIST OF TABLES.....	vi
LIST OF FIGURES.....	vii
ABSTRACT.....	x
CHAPTERS	
1 INTRODUCTION.....	1
Project Background and Goals.....	1
Test Methods.....	13
2 LITERATURE REVIEW.....	16
Slip Activation and Deformation.....	16
Anisotropy of Elasticity.....	19
Notch Tip Deformation.....	23
3 ANALYTICAL PROCEDURE.....	43
Coordinate System Transformation.....	43
Slip System Shear Stresses and Strains.....	54
4 NUMERICAL SOLUTION: FINITE ELEMENT METHOD.....	57
Finite Element Model.....	57
Model Characteristics.....	61
Solution Location.....	65
Assumptions.....	66
5 RESULTS AND DISCUSSION.....	68



Specimen A.....	68
Specimen B.....	79
Specimen C.....	89
Specimen/Orientation Comparison.....	99
Experimental Results.....	100
Application.....	103
 6 CONCLUSIONS.....	 107
 7 RECOMMENDATIONS FOR FUTURE WORK.....	 108
 APPENDIX A Coordinate Transformation Test.....	 109
 REFERENCES.....	 111
 BIOGRAPHICAL SKETCH.....	 114

## LIST OF TABLES

<u>Table</u>	<u>Page</u>
1-1 Slip systems in an FCC crystal.....	5
2-1 Atomic density on FCC crystal planes.....	20
2-2 Symmetry in various crystal structures.....	21
2-3 Stress subscripts.....	21
2-4 Experimental sector boundary angles.....	30
2-5 Orientation II sector boundary angle comparisons.....	32
2-6 Sector boundary angles for Crone and Shield .....	36
2-7 Slip sectors for plane stress and plane strain assumptions.....	40
2-8 Slip sectors for plane stress and experimental results.....	41
3-1 Direction cosines.....	49
4-1 Analytical and numerical component stresses for Specimen A.....	58
4-2 Analytical and numerical component strains for Specimen A.....	59
4-3 Actual (Specimen A) and finite element specimen geometry.....	61
5-1 Specimen A dominant slip system sectors.....	78
5-2 Specimen B dominant slip system sectors.....	88
5-3 Specimen C dominant slip system sectors.....	98
5-4 Specimen A experimental results.....	102

## LIST OF FIGURES

<u>Figure</u>	<u>Page</u>
1-1 Helical mold cast turbine blade .....	2
1-2 Primary and secondary turbine blade crystallographic orientations.....	3
1-3 Slip lines on the surface of a [100] loaded tensile specimen .....	6
1-4 Turbine blade failure on a {111} octahedral plane.....	6
1-5 Radial arcs for numerical stress field calculations.....	9
1-6 Slip sectors occurring under plastic deformation .....	10
1-7 Microstructure of PWA 1480.....	11
2-1 Primary resolved shear stress planes and directions .....	17
2-2 Load and slip directions and angles .....	18
2-3 Octahedral slip bands.....	18
2-4 FCC crystal structure .....	19
2-5 Notch direction terminology.....	24
2-6 Yield surface based on plane strain component stresses .....	25
2-7 Specimen orientation for Shield's test specimen.....	27
2-8 Slip systems predicted by Rice.....	28
2-9 Four-point bending setup used by Crone and Shield.....	29
2-10 Moiré interferometry strain field.....	29
2-11 Orientations experimentally tested by Crone and Shield .....	32
2-12 Experimental slip sectors from Crone and Shield .....	33
2-13 Full field slip sectors and slip line traces from Crone and Shield.....	34

2-14 Schulson and Xu's specimen orientation .....	37
2-15 Slip sectors under [-10-1] load.....	39
2-16 Maximum RSS slip system plots.....	40
3-1 Material ( $x_o, y_o, z_o$ ) and specimen ( $x'', y'', z''$ ) coordinate systems .....	45
3-2 First rotation about the $z_o$ -axis .....	46
3-3 Original and rotated axes projection.....	46
3-4 Second rotation about the y-axis.....	47
3-5 Third rotation about the $x'$ -axis .....	48
3-6 Load in the [213] direction .....	50
3-7 Two step coordinate transformation .....	50
4-1 Finite element analysis specimens and orientations .....	57
4-2 Specimen dimensions.....	60
4-3 Global and material coordinate systems .....	62
4-4 Finite element mesh about the notch tip .....	63
4-5 Element sizing on the front face and through the thickness .....	64
4-6 ANSYS SOLID95 element.....	64
4-7 Radial arcs used for element location and sizing.....	65
5-1 Specimen A primary resolved shear stresses; $r = 0.25 \cdot \rho$ .....	70
5-2 Specimen A primary resolved shear stresses; $r = 0.5 \cdot \rho$ .....	71
5-3 Specimen A primary resolved shear stresses; $r = 1.0 \cdot \rho$ .....	72
5-4 Specimen A primary resolved shear stresses; $r = 2.0 \cdot \rho$ .....	73
5-5 Specimen A primary resolved shear stresses; $r = 3.0 \cdot \rho$ .....	74
5-6 Specimen A primary resolved shear stresses; $r = 5.0 \cdot \rho$ .....	75

5-7 Specimen A complete resolved shear stress field .....	77
5-8 Specimen B primary resolved shear stresses; $r = 0.25*\rho$ .....	80
5-9 Specimen B primary resolved shear stresses; $r = 0.5*\rho$ .....	81
5-10 Specimen B primary resolved shear stresses; $r = 1.0*\rho$ .....	82
5-11 Specimen B primary resolved shear stresses; $r = 2.0*\rho$ .....	83
5-12 Specimen B primary resolved shear stresses; $r = 3.0*\rho$ .....	84
5-13 Specimen B primary resolved shear stresses; $r = 5.0*\rho$ .....	85
5-14 Specimen B complete resolved shear stress field .....	87
5-15 Specimen C primary resolved shear stresses; $r = 0.25*\rho$ .....	90
5-16 Specimen C primary resolved shear stresses; $r = 0.5*\rho$ .....	91
5-17 Specimen C primary resolved shear stresses; $r = 1.0*\rho$ .....	92
5-18 Specimen C primary resolved shear stresses; $r = 2.0*\rho$ .....	93
5-19 Specimen C primary resolved shear stresses; $r = 3.0*\rho$ .....	94
5-20 Specimen C primary resolved shear stresses; $r = 5.0*\rho$ .....	95
5-21 Specimen C complete resolved shear stress field .....	97
5-22 Experimental load for Specimen A.....	101
5-23 Experimental tensile test specimen Material A.....	102
5-24 Tensile test specimen and surface slip lines.....	103
5-25 Numerical plot adjusted for example load; yield stress indicated.....	104
5-26 Numerical plot adjusted for example load; maximum RSS changes with theta....	105

Abstract of Thesis Presented to the Graduate School  
of the University of Florida in Partial Fulfillment of the  
Requirements for the Degree of Master of Science

THREE-DIMENSIONAL STRESS FIELDS AND SLIP SYSTEMS FOR SINGLE  
CRYSTAL SUPERALLOY NOTCHED SPECIMENS

By

Shannon M. Magnan

May 2002

Chairman: Nagaraj Arakere, Ph.D.

Major Department: Mechanical Engineering

Single crystal superalloys have become increasingly popular for turbine blade and vane applications due to their high strength, and creep and fatigue resistance at elevated temperatures. The crystallographic orientation of a single crystal material greatly affects its material properties, including elastic modulus, shear modulus, and ductility. These directional properties, along with the type of loading and temperature, dictate an anisotropic response in the yield strength, creep resistance, creep rupture ductility, fatigue resistance, etc.. A significant amount of research has been conducted to determine the material properties in the  $\langle 001 \rangle$  orientation, yet the material properties deviating from the  $\langle 001 \rangle$  orientation have not been assessed for all cases. Based on the desired application and design criteria, a crystal orientation is selected to yield the maximum properties. Currently, single crystal manufacturing is able to control the

primary crystallographic orientation within  $15^\circ$  of the target orientation, which is an acceptable deviation to meet both performance and cost guidelines; the secondary orientation is rarely specified.

A common experiment is the standard load-controlled tensile test, in which specimens with different orientations can be loaded to observe the material response. The deformation behavior of single-crystal materials under tension and compression is known to be a function of not only material orientation, but also of varying micro-deformation (i.e. dislocation) mechanisms. The underlying dislocation motion causes deformation via slip, and affects the activation of specific slip systems based on load and orientation. The slip can be analyzed by observing the visible traces left on the surface of the specimen from the slip activity within the single crystal material. The goal of this thesis was to predict the slip systems activated in three-dimensional stress fields of a notched tensile specimen, as a function of crystal orientation, using finite element analysis without addressing microstructural deformation mechanisms that govern their activation. Out of three orientations tested, the specimen with a  $[110]$  load orientation and a  $[001]$  growth direction had the lowest maximum resolved shear stress; this specimen orientation appears to be the best design candidate for a tensile application.

## CHAPTER 1 INTRODUCTION

### Project Background and Goals

#### Single Crystal Superalloys

Nickel-base single crystal superalloys have become increasingly popular, particularly in turbine blade applications, because of their exceptional thermo mechanical fatigue properties at high temperature. Unlike the more commonly used isotropic alloys, these superalloys are orthotropic and have highly directional material properties because they are grown as single crystals (i.e. as one grain). The most common primary growth direction for the nickel-base superalloys is the  $\langle 001 \rangle$  direction;  $\langle 001 \rangle$  is not only the most easily grown, but is also the direction with the most desirable combined strength properties. This is advantageous because many parts are cast, or grown, rather than manufactured from a larger single crystal sample with a specific orientation. Currently we are most interested in one particular alloy, which will be referred to here as “Material A,” because of its use in advanced aircraft engines. (Note: Currently we are unable to disclose the specific alloy due to security restrictions.) These superalloys play an important role in commercial and military propulsion systems as well.

Single crystals are manufactured by selecting grains with a desired orientation and then “growing” the part in one of two ways. The first method uses a helical mold, commonly called a “pigtail,” placed between a chill plate and the part casting. As a grain



moves through the mold, the helix enables selection of grains with a  $\langle 001 \rangle$  orientation, which then grow through the coils and up through the mold itself. Although some

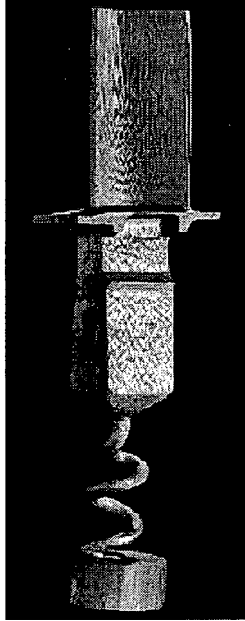


Figure 1-1 Helical mold cast turbine blade.  
Source: Deluca, 2001.

undesirable grains may initially form at the starter plate, after building up through the coils only the  $\langle 001 \rangle$  grain orientation remains (Figure 1-1). The coils are later removed to leave the desired part geometry. The helical mold is frequently used to manufacture turbine blades, but it can only be used to cast parts with a primary orientation along one of the  $\langle 100 \rangle$  directions due to the helix restrictions combined with the material's orthogonal grain growth (Davis, 1997). The second method uses a grain starter, or seed, and is consequently termed "seeding." Like the helical mold, this method can also be used to grow  $\langle 100 \rangle$  primary orientations, but it can also produce  $\langle 011 \rangle$  and  $\langle 111 \rangle$  crystals as well. In fact, a properly chosen seed grain can produce any desired primary

and secondary orientation combination. The seed is placed on a chill plate at the base of a casting filled with the molten material. The temperature is tightly controlled to prevent the seed from melting, and the alloy in the mold conforms to the seed alignment as the material cools.

Currently, the primary direction (i.e. growth direction) can be controlled relatively well, but still has an allowable deviation of  $15^\circ$  in any direction. Although it is possible to reduce this deviation by simply discarding those parts with larger variations, the cost in wasted materials would be too great and would result in a significant percentage of scrapped parts. Nonetheless, the material properties vary greatly as the primary direction deviates from the  $\langle 001 \rangle$  orientation, and it is important to quantify the effect of other

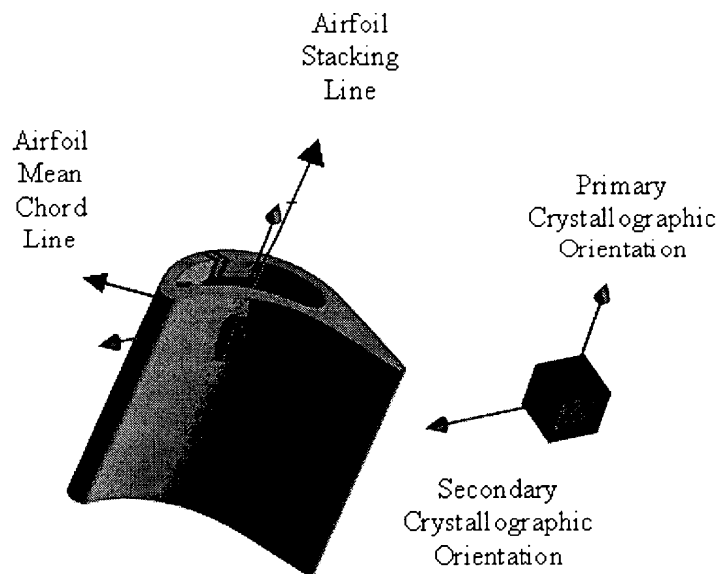


Figure 1-2 Primary and secondary turbine blade crystallographic orientations.  
Source: Moroso, 1999.

orientations on material properties. The secondary orientation can also be controlled during casting (Figure 1-2), however most manufacturers choose to ignore this control to achieve greater productivity. The material can, however, be examined after casting to determine secondary orientation, and if a particular secondary orientation has beneficial material properties for the specific application the part can then be further manufactured by cutting from the cast piece. When it becomes possible to more tightly control the manufacturing process, both the primary and secondary orientations with the best material properties can be combined and applied. Although  $\langle 001 \rangle$  is well known to be the strongest orientation in terms of yield strength (Davis, 1997), the underlying dislocation and slip deformation mechanisms, with respect to the primary orientation, are still under study.

### Slip Deformation

Nickel-base superalloys have a basic face centered cubic (FCC) structure in the matrix phase. These superalloys undergo the usual method of plastic deformation by slip, where separate parts of the crystal structure slide over one another along definite crystallographic, or slip, planes in specific directions (Dieter, 1986). When a load is applied to an FCC single crystal specimen, the first slip systems to be activated are those termed the “easy glide” systems (Table 1-1), or the primary octahedral slip systems. Typically, these are the planes with the greatest atomic densities. As deformation and slip activity continue, the material begins to exhibit physical evidence of this slip at the surface (Figure 1-3). Slip occurs so that the energy of the high shear stress within these 12 primary slip systems (known as the “resolved shear stress” or RSS) is alleviated; the

Table 1-1 Slip systems in an FCC crystal.

Slip Number	Slip Plane	Slip Direction
Octahedral Slip $a/2\{111\}\langle 110 \rangle$		
1	(111)	[10-1]
2	(111)	[0-11]
3	(111)	[1-10]
4	(-11-1)	[10-1]
5	(-11-1)	[110]
6	(-11-1)	[011]
7	(1-1-1)	[110]
8	(1-1-1)	[0-11]
9	(1-1-1)	[101]
10	(-1-11)	[011]
11	(-1-11)	[101]
12	(-1-11)	[1-10]
Octahedral Slip $a/2\{111\}\langle 112 \rangle$		
13	(111)	[-12-1]
14	(111)	[2-1-1]
15	(111)	[-1-12]
16	(-11-1)	[121]
17	(-11-1)	[1-1-2]
18	(-11-1)	[-2-11]
19	(1-1-1)	[-11-2]
20	(1-1-1)	[211]
21	(1-1-1)	[-1-21]
22	(-1-11)	[-21-1]
23	(-1-11)	[1-2-1]
24	(-1-11)	[112]
Cubic Slip $a/2\{100\}\langle 110 \rangle$		
25	(100)	[011]
26	(100)	[01-1]
27	(010)	[101]
28	(010)	[10-1]
29	(001)	[110]
30	(001)	[-110]

Source: Stouffer and Dame, 1996.

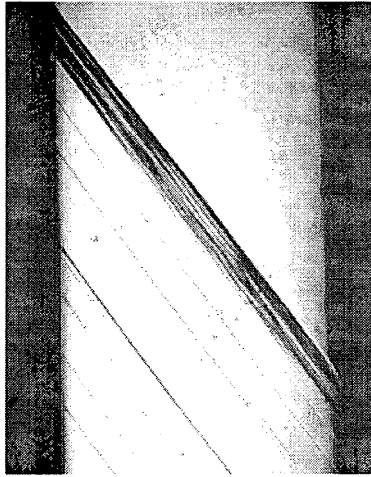


Figure 1-3 Slip lines on the surface of a  $[100]$  loaded tensile specimen.  
Source: Forero and Ebrahimi, 2002.

slip, or dislocation motion, results in a more energetically stable system. Therefore, materials typically fail along one of the primary  $\{111\}$  octahedral planes (Figure 1-4). As the applied stress continues to rise, or with changes such as loading type/direction, time or temperature, the activation of 12 secondary slip systems may occur. At low

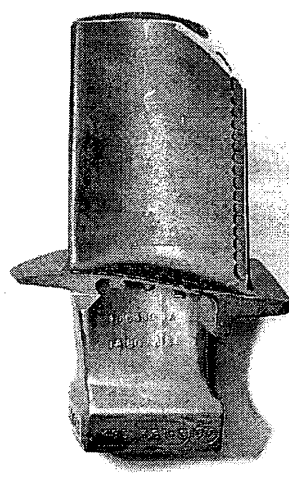


Figure 1-4 Turbine blade failure on a  $\{111\}$  octahedral plane. This particular turbine blade failed because the attached machine's frequency was equivalent to the turbine blade's natural frequency (upper right corner).  
Source: Deluca, 2001.

modulus orientations, or at extreme temperature/load conditions, the initiation of six cubic slip systems may also occur (Table 1-1). These secondary and cubic systems are not typically activated initially, because slip along the primary systems requires less energy to alleviate the high RSS. In addition to load and temperature conditions, the shift in slip from the primary to secondary or cubic slip systems is based on specific microstructural behaviors, such as the pinning or locking of dislocations, and will be discussed later only at a cursory level.

Slip will occur when the RSS exceeds the yield strength of the material. However, nickel-base superalloys have been shown to exhibit different yield strengths in tension versus compression, a behavior known as tension/compression asymmetry. The  $\langle 001 \rangle$  orientation exhibits its highest yield strength in tension, while its compressive yield strength is lower. Conversely, a sample loaded in the  $\langle 110 \rangle$  direction is stronger in compression rather than tension, while the  $\langle 111 \rangle$ -loaded material has virtually no tension/compression asymmetry. Extended dislocations are dislocations whose parts separate to reach a lower energy state; these dislocations, as on octahedral slip planes in superalloys, must recombine into a single dislocation before cross-slip can occur. Cross-slip is the process where a dislocation moves from one plane to another, again to reduce the energy of the system. As Lall, et al. (1979) proposed, an applied load will either aid or hinder recombination of the dislocation parts. Since the material orientation affects the magnitude of the resolved shear stresses, it will also affect this process of recombination. For example, if a compressive load is applied and two partial dislocations are at an interface where cross-slip can occur, the applied load can overcome the force separating the two partials, and combine them to form a single dislocation. The

unified dislocation can then move by cross-slip. If, however, a tensile load is applied to the same extended dislocation, the load will aid the force separating the partials and make cross-slip more difficult.

Asymmetrical load behavior becomes extremely important when designing a part that must accept both tensile and compressive loads, for example parts under cyclical loading. However, the priority given to compressive stress analysis is a distant second behind tensile stress analysis with respect to fracture research, because compressive stresses are generally beneficial. Rather than causing cracks to initiate or propagate, compressive stresses usually either have no effect or may even arrest cracks that developed under tensile stresses. Therefore our focus on tensile testing is practical and relevant.

Nickel-base superalloys exhibit another abnormal yield characteristic called “anomalous yield behavior.” Normal yield behavior shows decreasing yield strength with increasing temperature. As the temperature rises, diffusion enables cross-slip to occur more easily and the dislocations encounter fewer energy-based restrictions; the overall force required to produce deformation is reduced. The nickel-base superalloy matrix and precipitate show the opposite trend: as temperature increases their yield strength increases, up to a critical temperature. This behavior is a result of dislocation mechanisms and, like tension/compression asymmetry, is also affected by orientation. As the temperature increases and enables cross-slip to cubic planes, the dislocations dissociate to lower their energy and may form “locks,” (Kear-Wilsdorf locks, among others (Zhu, et al., 1998)). The term “lock” is used because the dislocation separates in such a way, on two separate planes, that no further motion can take place. Other

dislocations then begin to build up at these locks, which act as barriers to further slip and raise the yield stress by impeding motion. Anomalous yield behavior is an important consideration for fracture and fatigue analysis, particularly at high temperatures, in order to understand mechanisms that increase strength and their limitations. For this behavior to occur, the RSS on the cubic planes will, presumably, be higher than the octahedral planes; if the cubic planes are taking more of the stress, and are able to contain it with the locks, slip will only be achieved when a sufficient stress is resolved onto the octahedral planes. If, however, the stress on the octahedral planes is higher it should result in the traditional yield behavior and “easy glide” slip regardless of the dislocations on the cubic planes.

Our focus will be on the variation of the 12 primary resolved shear stresses in a notched specimen, and to determine the activity of the specific slip systems with respect to radial and angular distances from the notch tip for specific orientations (Figure 1-5).

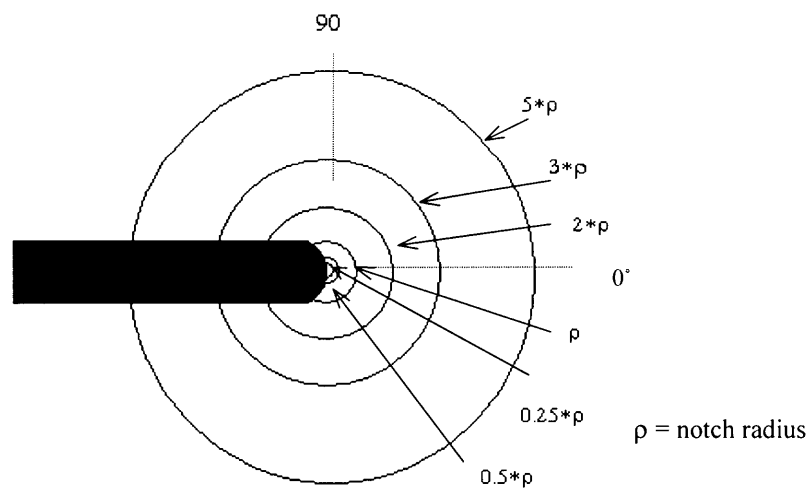


Figure 1-5 Radial arcs for numerical stress field calculations.



The slip systems will be examined both near the notch tip and at far-field to observe changes associated with the high stress gradients prevalent in close proximity to the notch tip. The variation of the RSS with respect to theta will show which systems are most active at various locations around the notch. What we expect to see, along a line of constant radius, is shifting maximum RSS values and slip systems, indicating a shift in

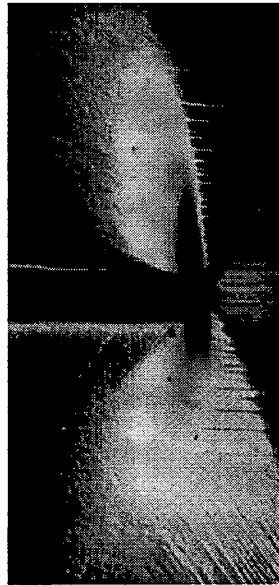


Figure 1-6 Slip sectors occurring under plastic deformation.  
Source: Crone and Shield, 2001.

the state of stress. These different slip systems can be clearly seen as “sectors” surrounding the notch tip in actual material tensile testing (Figure 1-6). The goal of this paper is to predict slip system activity, indicated by the maximum RSS, as a function of the radial and angular distances from the notch tip and the resulting slip sectors.

Slip deformation is generally considered a stress-controlled process; the critical resolved shear stress (CRSS), or the stress at which the material is predicted to slip on any particular slip plane, is the controlling value. The CRSS is the shear stress that

equals the material's yield strength, and is a function of the applied load and direction, specimen geometry, and crystal structure. Therefore the RSS is a function of geometry, and the CRSS is a function of geometry and yield stress; neither are directly related to the material's anisotropy.

### Material Characteristics

The microstructure of nickel-base superalloys consists of a  $\gamma$ -matrix and a fine dispersion of hard,  $\gamma'$ -precipitates. The matrix, mainly nickel, is heavily alloyed with other elements that vary with the given alloy, including cobalt, chromium, tungsten and tantalum; the precipitate is the intermetallic compound  $\text{Ni}_3\text{Al}$ . These superalloys have evolved in three "generations," thus far. The most advanced, or third-generation, superalloys include René N4, CMSX-4, and others, and have a high volume fraction of  $\gamma'$ , around 60% (Figure 1-7). (Note: The prefixes denote the company that manufactures

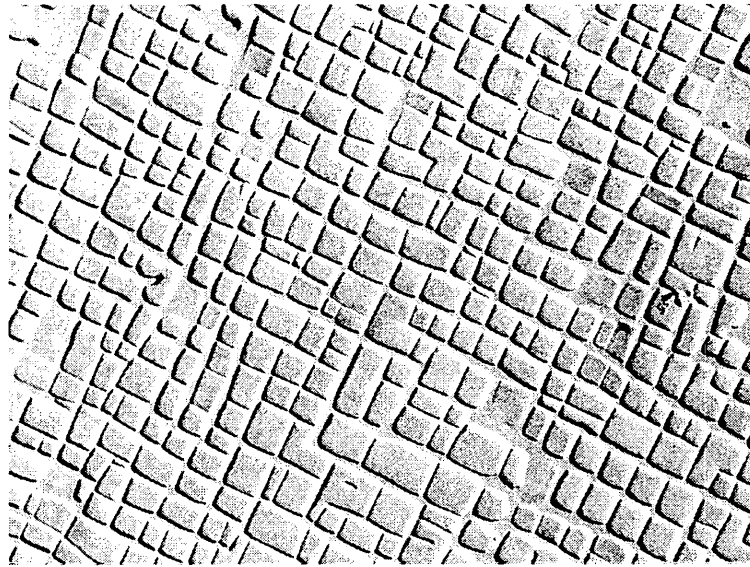


Figure 1-7 Microstructure of Material A. The  $\gamma'$  precipitate (approximately  $0.5\mu\text{m}$  in length) forms in the  $\gamma$  matrix and comprises nearly 60% of the material.  
Source: Deluca and Annis, 1995.

the material; e.g. CMSX = Cannon-Muskegon, where SX represents *single crystal*. The numbers are somewhat arbitrary depending on the particular manufacturer.) Although the majority of deformation occurs in the softer matrix (Svoboda and Lukáš, 1998), the precipitate has a pronounced effect on the superalloy's overall performance, especially at such high volume fractions.

### Temperature Effects

One of the primary reasons for the popularity of Material A and other nickel-base superalloys is their high temperature capabilities. As noted previously, dislocation mechanisms can change with temperature, and a significant amount of research has been conducted on their behavior. Most notched tensile tests conducted to study slip sectors have been performed at standard room temperature; room temperature is in the low temperature regime, well below the transition temperature for superalloys. As Stouffer and Dame (1996) report, octahedral plane slip deformation usually dominates, and theoretically exclusively controls, low temperature deformation. As the temperature rises the secondary planes may be activated, and beyond  $T > 600^{\circ}\text{C}$  thermally activated cube slip begins and acts along with octahedral slip. As the temperature further increases beyond approximately  $850^{\circ}\text{C}$ , climb and cross-slip dominate deformation and the material's strength dependence on orientation is greatly reduced. Miner, et al. (1986) also found that near  $\langle 111 \rangle$  only cubic deformation was evident, while near  $\langle 110 \rangle$  and  $\langle 100 \rangle$  only octahedral slip was present. Our study will focus on  $\langle 110 \rangle$  and  $\langle 100 \rangle$  orientations, supporting our focus on octahedral slip.

### Test Methods

Several analytical and numerical solutions have been developed for the elastic response of isotropic notch specimens in tension, particularly in the field of linear elastic fracture mechanics. However, the isotropic analytical models have been very difficult to develop into three-dimensional anisotropic models; the current solutions rely on many simplifications that give inaccurate results when compared to experimental data. However, the capabilities of three-dimensional finite element analysis (FEA) can account for the current limitations in the elastic models and enable a solution that should correlate well to actual experimental results. Both the numerical and experimental specimens may include notches, which act as very simplified cracks to model fracture behavior. The effect of anisotropy is of great interest because many materials, although designed for primary strength in one direction, must withstand multi-axial loading.

### Analytical Approach

Analytical solutions have the ideal trait of providing an exact solution to a problem. However, very complex problems often do not have exact analytical solutions; many approaches represent a combination of theoretical and empirical solutions, or close approximations. For the notched tensile specimen, an analytical mechanics solution is not available (much less one that can account for material variations) that correctly predicts slip sectors or slip activity about the notch tip. The current analytical solutions incorporate many assumptions, including plane strain, which will be discussed in depth in Chapter 2.

### Numerical Approach

Finite element analysis is able to account for gross isotropic material properties, such as modulus of elasticity and Poisson's ratio, as well as their directional counterparts in anisotropic materials. However, FEA typically does not account for the microstructural properties that dictate yield strength, such as dislocation mechanisms, nor can it predict other microstructural behavior. Small-scale atomistic simulations are capable of predicting dislocation generation, interaction, etc., however it would be much too costly to analyze even a very small specimen with actual dimensions on the atomic level. Limiting the size for a reasonable atomistic simulation would distort the model to the degree that the validity of the results would be highly questionable. Therefore, FEA is the only feasible type of computer simulation currently available to model notched single crystal specimens. Because it neglects microstructural behavior, FEA can also determine what influence the specimen's geometry and anisotropy have alone on material property behavior, without the additional consideration of atomic interactions.

### Experimental Approach

Tensile testing has long been used to measure material properties such as stress-strain behavior, yield strength, etc. and is common in many materials testing laboratories. A widely used experimental test sample is the notched specimen, loaded to observe the effect on the material's overall displacement, stress and strain fields, and of particular interest here, slip line deformation. The notch introduces a triaxial state of stress in the proximity of the notch, thus providing an environment to study slip system formation in three-dimensional stress fields. Future tensile tests will be carried out for the single crystal superalloy Material A to observe the effect of the load orientation on the active

slip regions, or “sectors,” about the notch to compare with FEA results. Using a constant load several tests specimens with different crystallographic orientations will be tested to failure to observe the active slip planes. Although this is clearly a different procedure than the purely elastic response measured by FEA, the magnitude of the applied elastic stress is an indication of which planes will first allow plastic deformation. If the most highly-stressed planes in the elastic analysis do not correlate to the slip lines observed from the tensile specimens, it will support the influence of other dislocation mechanisms on fracture.

## CHAPTER 2 LITERATURE REVIEW

An analysis of the stress-field at a single crystal notch involves two main components: incorporating the correct component and RSS calculations, and then defining the resulting slip zones around the notch. For a solid (i.e. no notch) specimen, the stresses can be precisely calculated using an analytical approach. Obviously there are not sectors defined for this solid material. However, the more complex, and relatively unexplored, study of the stresses and sectors around a notch tip is of recent origin; despite the analytical and experimental investigations by researchers (Rice, 1987; Shield, 1996; Schulson and Xu, 1997; Crone and Shield, 2001) an accurate single crystal model is far from complete.

### Slip Activation and Deformation

Slip in single crystals should theoretically occur on octahedral planes (Chapter 1). In an isotropic material the twelve primary slip systems (or fewer depending on orientation), should be activated simultaneously based on equal Schmid factors (Figure 2-1). The Schmid factor,  $m$ , is a function of the load orientation, the slip plane orientation and the slip direction:

$$m = \cos \lambda \cdot \cos \phi \quad (2-1)$$

$$\tau_{RSS} = m \cdot \sigma \quad (2-2)$$

Where  $\sigma$  is the applied load,  $\tau_{\text{RSS}}$  is the RSS component in a given slip plane and direction,  $\lambda$  is the angle between the direction of the applied load and the shear direction, and  $\phi$  is the angle between the applied load and the normal to the slip plane (Figure 2-2).

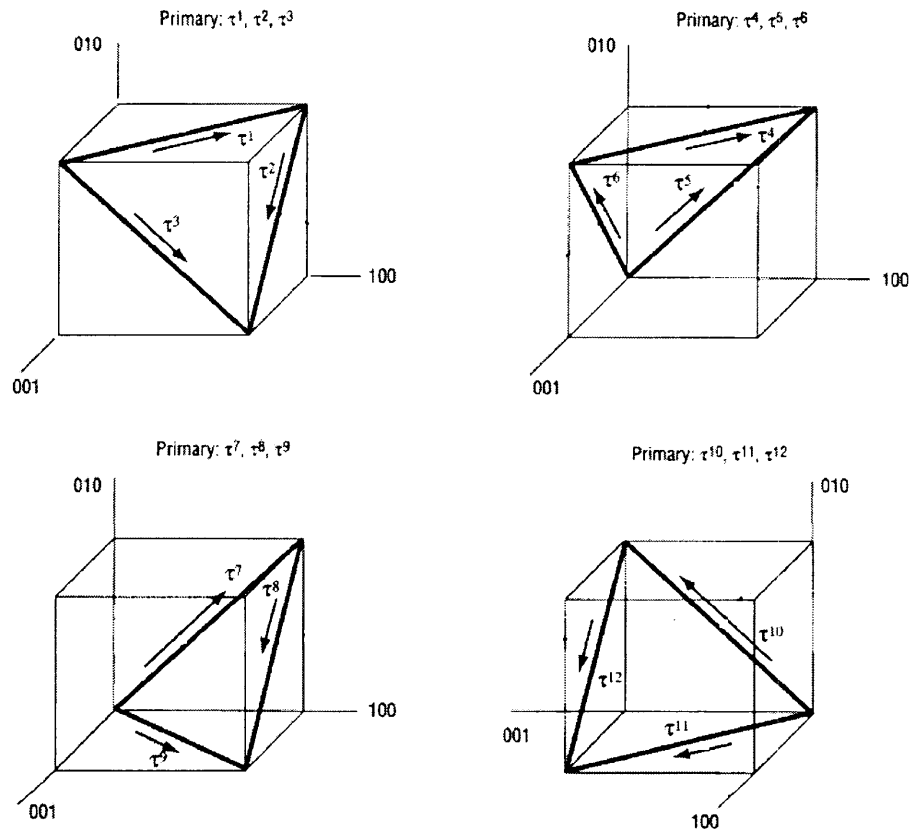


Figure 2-1 Primary resolved shear stress planes and directions.  
Source: Modified from Stouffer and Dame, 1996.



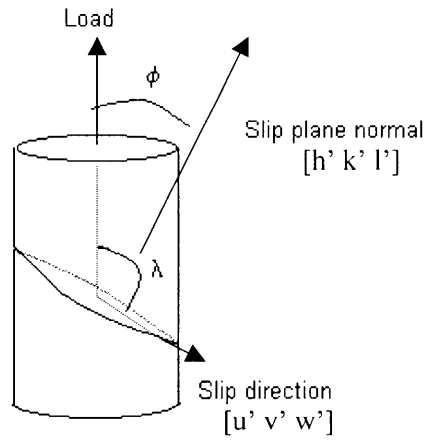


Figure 2-2 Load and slip directions and angles.



Figure 2-3 Persistent slip bands in an FCC specimen. Slip lines, formed by octahedral slip system activity, are clearly visible as the specimen undergoes plastic deformation.  
Source: Deluca and Annis, 1995.

Following Dieter (1986) the cosine of the angle between two directions  $[h_1 k_1 l_1]$  and  $[h_2 k_2 l_2]$  can be found using the direction indices:

$$\cos \theta = \frac{h_1 \cdot h_2 + k_1 \cdot k_2 + l_1 \cdot l_2}{\sqrt{h_1^2 + k_1^2 + l_1^2} \cdot \sqrt{h_2^2 + k_2^2 + l_2^2}} \quad (2-3)$$

Since the CRSS is reached when the RSS is equal to the yield stress of the material, the slip systems with the highest Schmid factors will reach the CRSS first: This is the so-called “Schmid Law” (Figure 2-3). However, compliance to Schmid Law has been proven only with isotropic materials, and its correlation to single crystals is not yet known. Therefore, another method must be used to predict RSS values and slip activation for these anisotropic materials.

### Anisotropy of Elasticity

#### Elasticity

Elasticity is defined by specific elastic constants that relate to atomic strength and spacing (Dieter, 1986). Elasticity, therefore, varies with orientation. In any given direction the spacing between atoms in an FCC unit cube is different. For example, in Figure 2-4 the distance from A to B is  $a_0/2$ , while the distance from A to C is  $a_0\sqrt{2}/2$ .

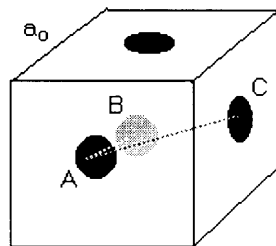


Figure 2-4 FCC crystal structure.

Another way of expressing the relative spacing between atoms is by the atomic density, or number of atoms per unit area (Table 2-1). The term  $a_0$  refers to the unit atomic spacing, therefore  $a_0^2$  is the area of the  $\{100\}$  planes, etc. The greatest atomic density correlates to the least distance between atoms, and the most likely planes for slip. Planes such as the  $\{111\}$  planes are called “close-packed planes,” because they minimize the spacing between atoms; they are the most common slip planes because the atoms do not

Table 2-1 Atomic density on FCC crystal planes.

FCC Plane	Atom/Area	Atom/Area
$\{100\}$	$2/a_0^2$	2
$\{110\}$	$2/\sqrt{2} \cdot a_0^2$	1.414
$\{111\}$	$4/\sqrt{3} \cdot a_0^2$	2.309

Source: Dieter, 1986.

have to travel great distances to reach another atomic position. Close-packed directions, like close-packed planes, minimize the distance between atoms. Therefore slip often occurs along close-packed directions in close-packed planes to minimize the amount of energy needed for displacement.

### Elasticity Matrix

The energy needed to move in any direction is related to the elastic constants, and any material can be completely defined with 36 separate elastic constants. However, most material structures obey some type of symmetry, which reduces the number of independent constants. As indicated in Table 2-2 isotropic materials have only two

Table 2-2 Symmetry in various crystal structures.

Crystal Structure	Rotational Symmetry	No. Independent Elastic Constants
Tetragonal	1 fourfold rotation	6
Hexagonal	1 sixfold rotation	5
Cubic	4 threefold rotations	3
Isotropic		2

Source: Dieter, 1986.

independent elastic constants. Two of the three: E, modulus of elasticity; G, shear modulus or  $\nu$ , Poisson's ratio will completely define the material properties in any direction. Cubic structures are highly symmetrical and require only one additional elastic constant, which reduces the overall elasticity matrix considerably.

The process of reducing the original 36 constants down to three independent cubic constants begins with the original full elasticity matrix,  $[a_{ij}]$ :

$$[a_{ij}] = \begin{bmatrix} a_{11} & a_{12} & a_{13} & a_{14} & a_{15} & a_{16} \\ a_{21} & a_{22} & a_{23} & a_{24} & a_{25} & a_{26} \\ a_{31} & a_{32} & a_{33} & a_{34} & a_{35} & a_{36} \\ a_{41} & a_{42} & a_{43} & a_{44} & a_{45} & a_{46} \\ a_{51} & a_{52} & a_{53} & a_{54} & a_{55} & a_{56} \\ a_{61} & a_{62} & a_{63} & a_{64} & a_{65} & a_{66} \end{bmatrix} \quad (2-4)$$

The subscripts correlate to the stress and strain components; the strain then is:

$$\epsilon_i = a_{ij} \sigma_j \quad (2-5)$$

CHAPTER 3 Assuming elastic potential exists (i.e. isothermal deformation) the following relationship is achieved in equilibrium:

$$a_{ij} = a_{ji} \quad (2-6)$$

Therefore the most general matrix is reduced to 21 components:

$$\begin{aligned}
& a_{11} \ a_{12} \ a_{13} \ a_{14} \ a_{15} \ a_{16} \\
& a_{12} \ a_{22} \ a_{23} \ a_{24} \ a_{25} \ a_{26} \\
[a_{ij}] = & a_{13} \ a_{23} \ a_{33} \ a_{34} \ a_{35} \ a_{36} \\
& a_{14} \ a_{24} \ a_{34} \ a_{44} \ a_{45} \ a_{46} \\
& a_{15} \ a_{25} \ a_{35} \ a_{45} \ a_{55} \ a_{56} \\
& a_{16} \ a_{26} \ a_{36} \ a_{46} \ a_{55} \ a_{66}
\end{aligned} \tag{2-7}$$

CHAPTER 4 Nickel-base superalloys are orthotropic, meaning they have three orthogonal planes of elastic symmetry. Including the effects of cubic elastic symmetry, also called “cubic syngony” (Lekhnitskii, 1963) reduces the number of independent constants to

three for the final elasticity matrix:

$$\begin{aligned}
& a_{11} \ a_{12} \ a_{12} \ 0 \ 0 \ 0 \\
& a_{12} \ a_{11} \ a_{12} \ 0 \ 0 \ 0 \\
[a_{ij}] = & a_{12} \ a_{12} \ a_{11} \ 0 \ 0 \ 0 \\
& 0 \ 0 \ 0 \ a_{44} \ 0 \ 0 \\
& 0 \ 0 \ 0 \ 0 \ a_{44} \ 0 \\
& 0 \ 0 \ 0 \ 0 \ 0 \ a_{44}
\end{aligned} \tag{2-8}$$

The constants are defined by the modulus of elasticity, the shear modulus, and Poisson’s ratio along given directions:

$$a_{11} = \frac{1}{E_{xx}} \tag{2-9}$$

$$a_{44} = \frac{1}{G_{yz}} \tag{2-10}$$

$$a_{12} = -\frac{\nu_{yx}}{E_{xx}} = -\frac{\nu_{xy}}{E_{yy}} \tag{2-11}$$

For Material A the reported elasticity constant values are (Swanson and Arakere, 2000):

$$a_{11} = 6.494 \text{E} - 8 \quad a_{44} = 6.369 \text{E} - 8 \quad a_{12} = -2.603 \text{E} - 8 \quad (\text{psi})$$

Using these elastic constants and the direction cosines for a given orientation, it is possible to calculate the modulus of elasticity of the material in any direction (Dieter, 1986):

$$\frac{1}{E_{uvw}} = a_{11} - 2 \cdot (a_{11} - a_{12}) - \frac{1}{2} \cdot a_{44} \cdot (\alpha_3^2 \cdot \beta_3^2 + \beta_3^2 \cdot \gamma_3^2 + \alpha_3^2 \cdot \gamma_3^2) \quad (2-12)$$

Where  $\alpha_3$ ,  $\beta_3$  and  $\gamma_3$  are the direction cosines from the load direction to the x, y and z-axes, respectively (often called  $l$ ,  $m$  and  $n$ ). Some materials, such as tungsten, are essentially isotropic, even in single-crystal form, because their elasticity is nearly constant in any direction. Others, like nickel-base superalloys, vary considerably.

#### Notch Tip Deformation

The behavior of an ideal material, one that has an infinite body free from any irregularities or stress concentrations, is very different from the typical superalloy applications. A turbine blade, for example, has a complex geometry, is exposed to multiaxial, centrifugal, and contact stresses; and must withstand extreme temperature gradients, among other complex conditions. In an attempt to study the state of stress for more complex specimens, notched tensile specimens are often used to represent either areas of stress concentration or theoretical fracture conditions.

#### Rice (1987)

Rice provided the foundation for much recent and current work in the area of crack/notch tip stress and strain analysis by examining the mechanics of both FCC and BCC (body-centered cubic) notched specimens loaded in tension. Rice introduced the use of a plane

strain assumption, which he combined with the CRSS criteria to predict specific zones, or “sectors.” These angular regions radiating from the notch tip characterize different regions where specific deformation mechanisms are at work. He began with two commonly studied orientations (later further studied by Crone and Shield, Figure 2-11) and derived an analytical solution to predict the active slip systems around a notch, as

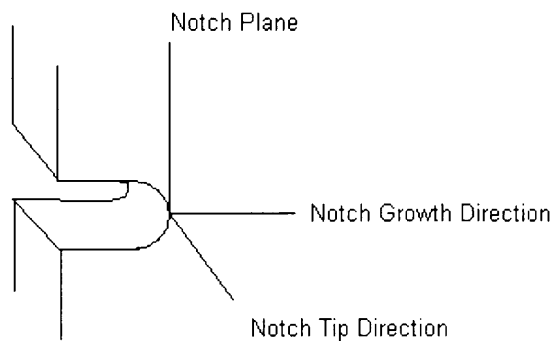


Figure 2-5 Notch direction terminology.

well as the specific angles defining the boundaries between sectors. Rice, and others who follow his work, typically refer to tensile test specimen orientations in terms of notch plane, notch growth direction, and notch tip direction (Figure 2-5). His terms will be maintained throughout this discussion to prevent confusion.

Based on the plane strain assumption, the yield criteria can be presented in terms of a “yield area,” which outlines the boundaries where the state of stress will correspond to the yield stress of the material (Figure 2-6). The slip activity is limited to certain allowable slip systems, which combine to produce large in plane strains in accordance with the plane strain assumption (i.e.  $\epsilon_{zz} = \gamma_{yz} = \gamma_{zx} = 0$ ). The plastic field Rice constructs

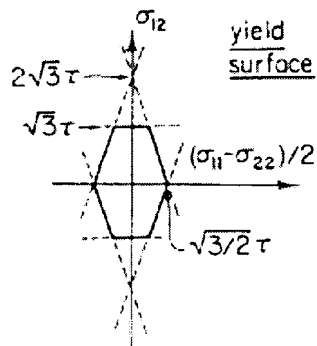


Figure 2-6 Yield surface based on plane strain component stresses.  
Source: Rice, 1987.

at the crack tip also correlates to a plane strain state of stress in an isotropic material. By essentially eliminating the effect of single crystal anisotropy, this solution likely would not correlate well to experimental data. Another effect of the simplified elasticity of Rice's solution is the inability to solve for a detailed strain field based on the state of stress near the tip. Assuming the out of plane stress and strain is equal to zero near the notch tip, the effect of the notch on creating a triaxial state of stress is essentially nullified.

Rice's solution represents a continuous solution in terms of the radius and angular displacement from the tip, where the state of stress is constant within each sector. The solution is symmetric about the growth axis for each case based on crystal lattice structure, so only the positive half-plane will be discussed. Rice notes the only way all the notch surface boundary conditions can be met for all angles is if 1) the stresses in some sectors are below yield, or 2) there are discontinuities at certain angles. Rice assumes a perfectly plastic stress field, so all sectors must be at yield or past, and the first condition cannot be changed. (Note: this assumption is contrary to varying elastic and



plastic sectors commonly observed during fracture testing.) Therefore the boundaries are defined as the radial lines where a discontinuity occurs at specific angles where the slip shifts from one system to another. (Note: Rice also solves for the second condition, maintaining continuity in order to later apply his solution to a separate crack growth model. For this case, some angular sectors may be elastic while others are plastic, corresponding to those locations where the solution intersects the aforementioned yield surface.)

Rice's solution makes no distinction between the two orientations' sector boundaries, or between FCC or BCC crystal structure. Both crystal orientations and structures predict boundaries at  $55^\circ$ ,  $90^\circ$ , and  $125^\circ$ . The slip systems do change between orientations and corresponds to a switch between the slip system shear and normal directions; thus orientation predicts no effect on the yield surface or sector boundaries. Rice notes the weakness of this attribute, based on contradictory experimental studies, which is tied to the actual rotation of the crystal lattice he has ignored. He also acknowledges the simplification of the plane strain assumption, which was intended only as a starting point. Finally, Rice neglects strain hardening, but encourages incorporating all simplifications into future models.

#### Shield, Cu (1996)

Shield conducted several tests of notched single crystal copper specimens to correlate Rice's analytical models with his experimental observations. Based on symmetry and the previous work done by Rice, Shield chose to test two identical specimens with a notch in the  $[011]$  plane and a  $[100]$  notch direction (Figure 2-7, matching with the later "Orientation II" in work by Crone and Shield, 2001); the sectors

and boundaries are symmetrical about the  $[100]$  axis, therefore only the upper half-plane ( $+\theta$ ) will be discussed. Following Rice, four sectors were predicted with boundaries at  $0^\circ$ ,  $55^\circ$ ,  $90^\circ$ ,  $125^\circ$ , and  $180^\circ$ . Recall, Rice chose these angles based on his plane strain assumption: the active slip planes must actually represent a combination of slip systems that result in plane strain deformation for his assumption to be valid. Furthermore, the

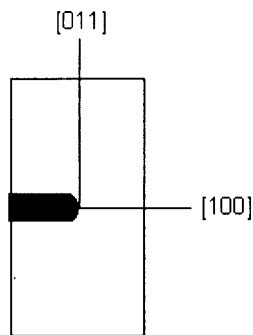


Figure 2-7 Specimen orientation for Shield's Cu test specimen.

sector boundaries can only occur at angles that correspond to the active slip system directions or their normals within the adjacent sectors. For example, if the active slip directions in a given sector are at  $55^\circ$  and  $125^\circ$  to the  $[100]$  axis, then that sector's boundary angles must be from the set:  $55^\circ$ ,  $125^\circ$  (both slip),  $-35^\circ$ ,  $145^\circ$ ,  $35^\circ$  or  $215^\circ$  (all normals). One conclusion that must follow from Rice's assumptions is that  $0^\circ$  and  $180^\circ$  cannot be actual boundaries unless the slip or normal matches those angles, which it does not (Figure 2-8). Therefore, the first and fourth sectors really span from  $-55^\circ$  to  $55^\circ$  and  $125^\circ$  to  $-125^\circ$ , respectively, which gives six sectors total in both half-planes versus eight.

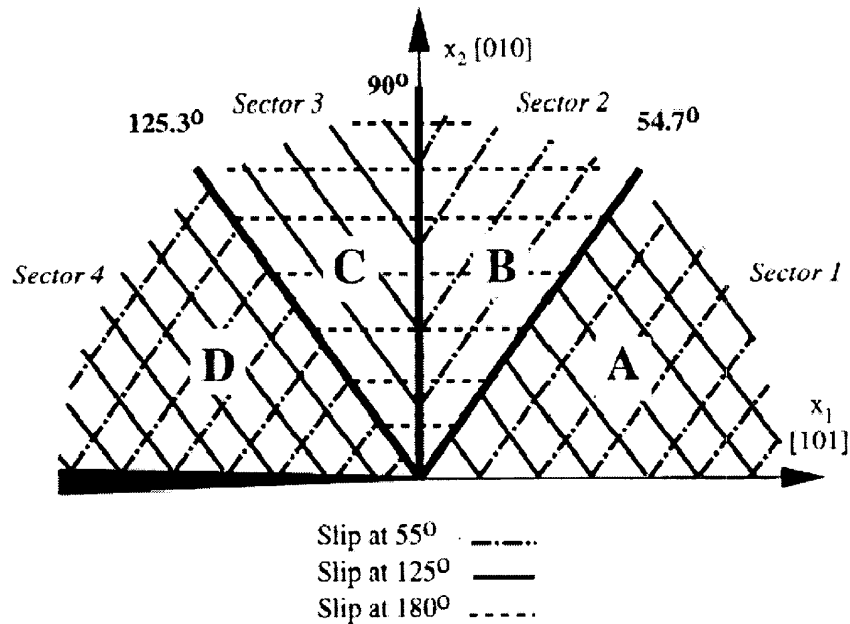


Figure 2-8 Slip systems predicted by Rice.  
Source: Crone and Shield, 2001.

The experiments done by Shield, and Crone and Shield, use four-point bending to deform the single crystal specimens plastically near the notch tip (Figure 2-9). Moiré interferometry analysis is then used to determine the strain fields and sectors. Shield's prediction of slip sectors, like Rice, is then based on plastic strain fields, rather than yield-inducing shear stresses. Shield assumes the elastic strain is negligible and the total strain is therefore equivalent to the plastic plane strain (i.e. a perfectly plastic state). The interferometry analysis technique uses a grid-like diffraction grating applied to the surface of the specimen. A laser works in combination with several mirrors to resolve the strains into u-field and v-field component fringe patterns (Figure 2-10), which are used to calculate the actual strain values. Moiré interferometry is a well-established

technique and has been verified in several similar applications (Mollenhauer, et al., 1995).

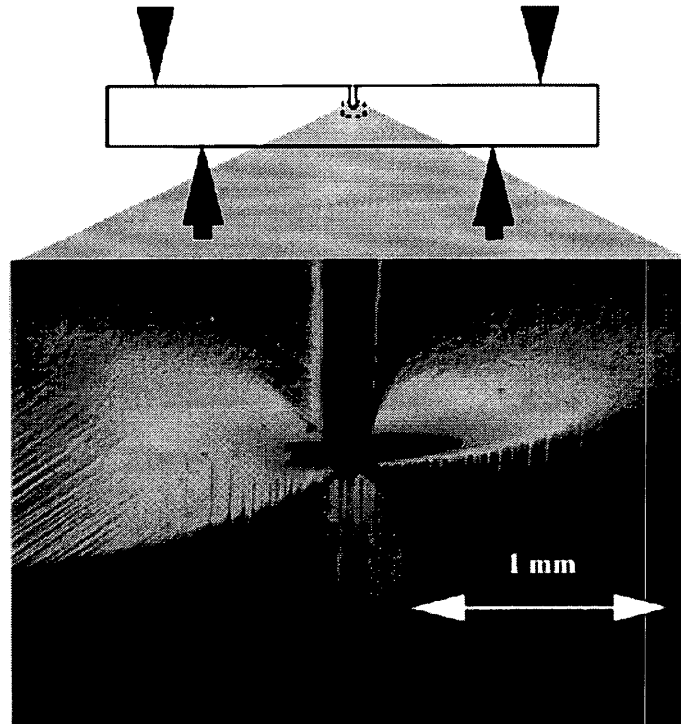


Figure 2-9 Four-point bending setup used by Crone and Shield.  
Source: Crone and Shield, 2001.

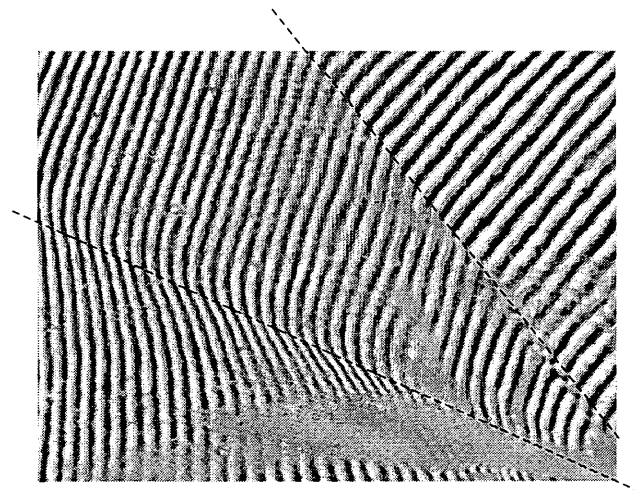


Figure 2-10 Moiré interferometry strain field. Shield determined the sector boundaries based on the obvious visible patterns; line emphasis mine.

Source: Shield, 2002.

Shield experimentally tested two separate specimens and measured the boundary angles, based on strain fields (Table 2-4). Applying several load levels, beginning at the yield point, he observed whether the load had any effect on the sector boundary angles.

Table 2-4 Experimental sector boundary angles.

Sector Boundary	Angle $\theta$ (deg)
1-2	43
2-3	62
3-4	100

No significant sector changes were observed as the load increased, indicating that the sectors are independent of the load level. However, as the load increased the amount of plasticity near the notch tip increased as well, allowing for some stress relaxation as the material responds. The high plasticity near the notch tip also has an impact on the method of measuring the sector angles. To avoid the large deformations near the tip, which do not represent the desired strain fields from which the sectors are determined, the origin for angular measurements are offset by  $50\mu\text{m}$  and the strains are presented along a  $400\mu\text{m}$  arc. Note: with the notch's mean width of  $100\mu\text{m}$  these measurements are taken at  $8\rho$ , where  $\rho$  is the notch radius. This is a significant distance from the notch tip, regardless of elastic versus plastic conditions, and seems disproportionate to get an accurate account of the behavior due to the notch.

Shield's results from the low load levels show similarities to Rice's model, however Shield's experimental results do not correlate to Rice's model at high plastic

strains (Figure 2-8 and Table 2-4). As would be expected in a plastic model, these strains are not proportional (i.e. they do not have a linear response). In fact, they do not even maintain the same order in their relative level of activity: Sector 2 initially shows the most activity, while at higher strains Sector 3 becomes more dominant. This changing slip activity (with load level) seems inconsistent with the constant sector boundaries. Constant angles indicate the boundaries are independent of the active slip within the sector; perhaps the boundaries appear constant due to relaxation in the material between the load steps. Between the two samples the boundary angles were similar but not constant, highlighting the variance that can result from the material structure alone and any flaws that may be present, despite a constant specimen orientation and test conditions. The precise notch geometry also a factor is, which is extremely difficult to duplicate accurately.

Plastic deformation at large strains is easily observed through slip lines; Shield used this visible slip evidence to compare the strain sectors determined by Moiré interferometry. The resulting sector boundary angles matched well with the strain field images. Since the activated slip systems are a function of the RSS, and because they correlate well to interferometry results, the sectors determined by strain field analysis appear to be analogous to those determined by a stress-field analysis. Shield's experimental results, and their dissimilarity to Rice's analysis, again highlight the need for a more accurate predictive model.

#### Crone and Shield, Cu and Cu-Be (2001)

Extending the work of Shield (1996), Crone and Shield continued experimental studies of notch tip deformation in two different orientations of single crystal copper and

copper-beryllium tensile specimens (Figure 2-11). (Orientation II will be presented first due to the widespread use of this orientation in other studies). Again using Moiré interferometry strain fields and visible slip evidence to determine sectors, sector boundaries are defined as the obvious visible changes from one area to another. The visible slip patterns determine slip activity, but as the authors note, a lack of visible slip does not rule out any activity. Slip systems may be activated internally, rather than at the surface, or may show varying patterns on the surface as deformation continues.

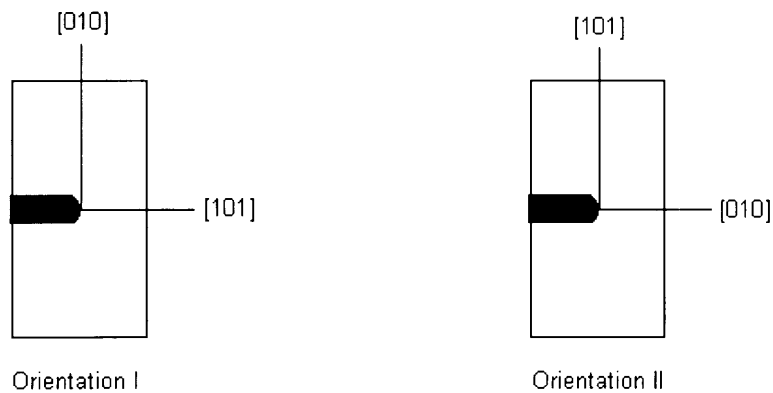


Figure 2-11 Orientations experimentally tested by Crone and Shield.

Crone and Shield compared their experimental results with Rice's analytical solution, as well as numerical FEA solutions by Mohan, et al. (1992) and Cuitino and Ortiz (1996) (Table 2-5). Both numerical models run on the plane strain assumption, although Cuitino and Ortiz later conclude the problem cannot truly be plane strain

Table 2-5: Orientation II sector boundary angle comparisons.

Sector boundary	Experimental	Analytical	Numerical	
*Boundary angles in degrees	Crone and Shield (2001)	Rice (1987)	Mohan, et al. (1992)	Cuitino and Ortiz (1996)
1-2	50-54	54.7	40	45

2-3	65-68	90	70	60
3-4	83-89	125.3	112	100
4-5	105-110		130	135
5-6	150			

Source: Modified from Crone and Shield, 2001

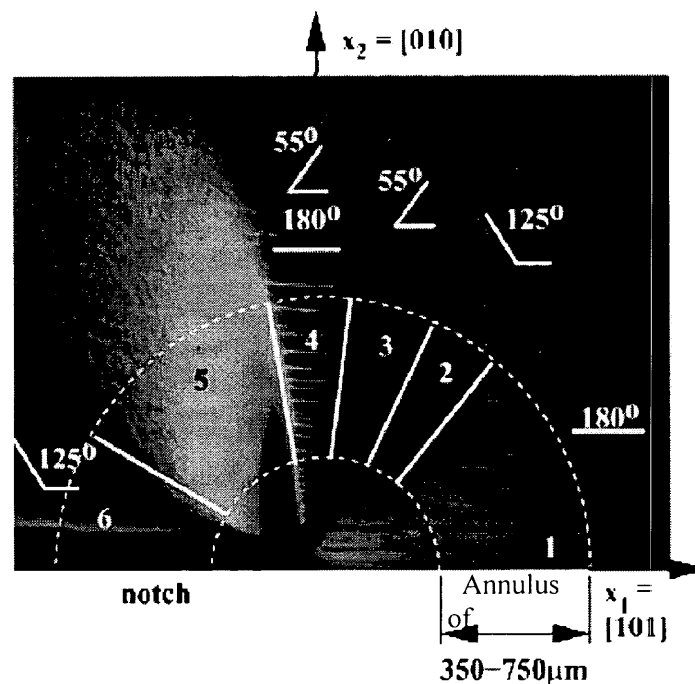


Figure 2-12 Experimental slip sectors from Crone and Shield.

Source: Modified from Crone and Shield, 2001.

due to large strain differences internally and at the surface. Even with the same plane strain assumption as Rice, the numerical and analytical models do not match; all three differ from the experimental results (Figure 2-12 and Figure 2-13). Like Shield's earlier results, the experimental results are somewhat ambiguous due to the "annulus of validity," where Crone and Shield take their measurements (Figure 2-12). This annulus, following Shield and Kim (1994) corresponds to the radial area from 350-750μm from the notch tip. The notch width is between 100-200μm, making the notch radius between



50-100 $\mu\text{m}$ . Therefore the annulus, and the region where the sectors are measured, is anywhere from 3.5-7.0 and 7.5-15.0 times the notch radius from the tip. These distances would place the sectors well out of the range of any elastic deformation and clearly can only be used where extreme plastic deformation exists. However, Crone and Shield preserve this annulus to avoid material too close to the notch tip, which is dominated by geometry, and a larger annulus which would begin to impose on these particular specimens' boundaries.

Crone and Shield describe the observed slip activity as it begins in a single sector; as deformation proceeds, more slip lines become visible in the same sector at further.

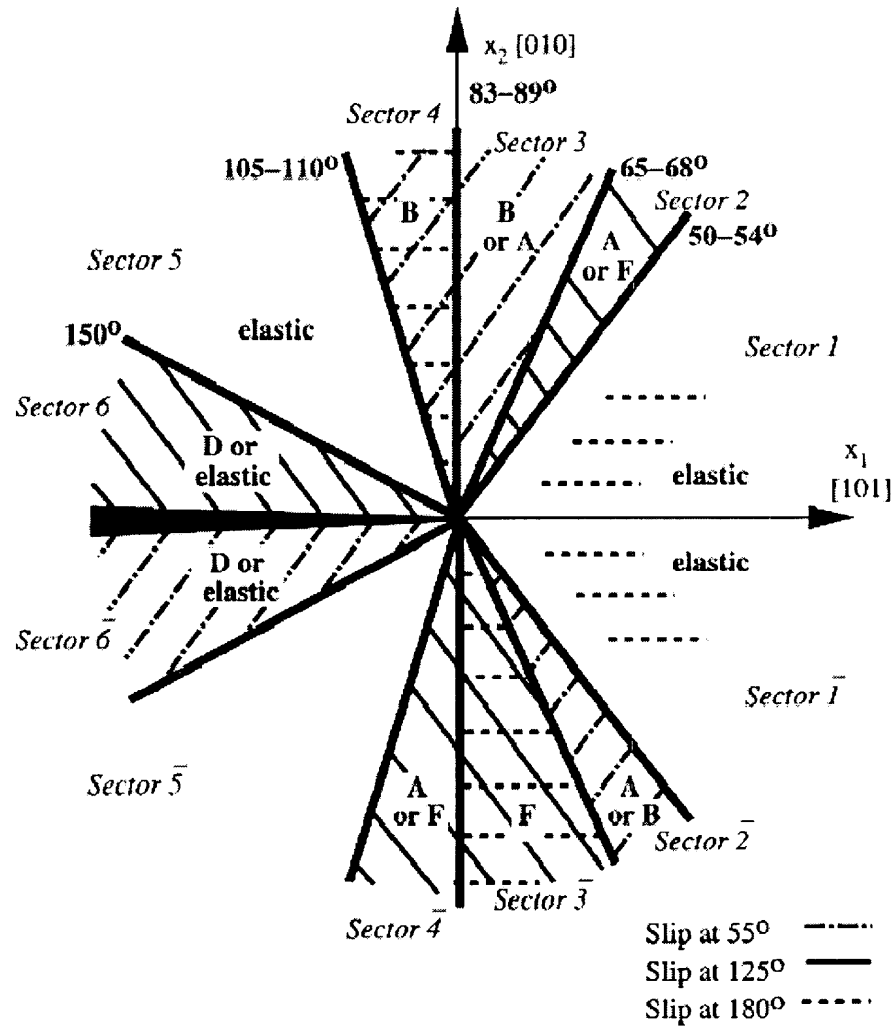


Figure 2-13 Full field slip sectors and slip line traces from Crone and Shield. Note: these sectors differ from Rice (1987) and Shield (1996).  
Source: Crone and Shield, 2001.

radial distances from the notch. This result is intuitive because a larger load will allow higher stresses even as distances from the notch tip increase. The number of slip lines then grows until the sector is “filled”. Although it is unclear what exactly is meant by “filled”, it is clear that, either the initially visible slip system, or another with the same

visible trace, remains active throughout the experiment. Crone and Shield clearly observe horizontal slip traces directly ahead of the notch (Sector 1) for Orientation II, however they discount their observations and instead label the slip as “elastic” in order to compare their solution to other perfectly plastic sharp crack solutions (Figure 2-13). Citing Saeedvafa and Rice (1989) they further explain these traces as a function of hardening and not plastic deformation, but they do not make such accounts for the other sectors. The only other sector determined to be elastic is Sector 5, and this is due to its lack of any visible slip activity as well as low strain measurements. Consequently, their determination of an elastic zone directly ahead of the tip is not consistent with their visible experimental results. As predicted, the experimental sectors are symmetric about the [101] axis. Only Sectors 3/-3 and 4/-4 show variation between  $+\theta$  and  $-\theta$  (Figure 2-13); the apparent asymmetry in these sectors is likely caused by specific notch geometry/irregularities, material defects, etc., or by a slightly inaccurate notch plane direction.

Orientation I represents Orientation II rotated by  $90^\circ$  about the notch tip direction, such that the notch plane and the notch tip/crack growth directions are switched. Contrary to the equivalent sectors predicted by Rice, Crone and Shield’s observed sectors show a marked difference with orientation, varying in both specific boundary angles and in the number of sectors (Table 2-6). Along with Rice’s prediction, none of the numerical solutions correspond to Orientation II, which they were designed for, or for Orientation I. The numerical finite element models, however, agree more closely than

Table 2-6 Sector boundary angles for Crone and Shield.

Sector boundary	Orientation I	Orientation II
*Boundary angles in degrees	(101) Plane	(010) Plane
1-2	35-40	50-54
2-3	54-59	65-68
3-4	111-116	83-89
4-5	138	105-110
5-6		150

Source: Crone and Shield, 2001

the others. Despite the disagreement of the experimental work to analytical and numerical solutions, Crone and Shield again support a plane strain assumption based on the numerical results from Cuitino and Ortiz (1996). The FEA results on a central plane of the model appeared to correspond more closely to the experimental results. Crone and Shield assert this agreement to the central plane FEA results suggests that plane strain is accurate for specific locations. However, obtaining results only from a central plane does not represent the true specimen being modeled. In fact, if there is a preference it should be for the model to be more accurate at the surface; where slip is thought to originate and actually observed, allowing a better comparison.

#### Schulson and Xu, Ni<sub>3</sub>Al (1997)

A recent study by Schulson and Xu (1997) examined the state of stress at a notch tip for single crystal Ni<sub>3</sub>Al, the  $\gamma'$ -component of Material A. Using three-point bending, two crystals were deformed at first elastically, then plastically until a crack formed, and finally through a small degree of crack propagation. Both samples were oriented with the growth direction [010], the notch plane direction [-10-1] and the notch tip direction

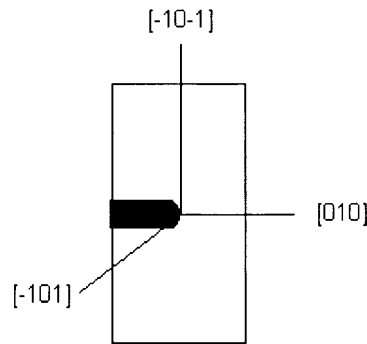


Figure 2-14 Schulson and Xu specimen orientation.

[-101] (Figure 2-14). To solve an analytical model to compare their experimental results to, they assumed elastic isotropic material conditions and calculated the stress field around the notch based on the equations for a sharp notch (Anderson, 1995). Although these equations may have been accurate for previous experiments they conducted with polycrystalline  $\text{Ni}_3\text{Al}$  (Xu and Schulson, 1996), the isotropic assumption is not valid for their single crystal specimens. Schulson and Xu carry out two sets of stress calculations, one based on plane stress conditions and another with plane strain. The plane stress assumption can be used for large, thin plates with in-plane loading, where only  $\sigma_x$ ,  $\sigma_y$ , and  $\tau_{xy}$  are present (Bickford, 1998); the thickness must be small compared to the height and width of the specimen. However, as Schulson and Xu note in their paper, the notch causes a triaxial state of stress, where out of plane material stresses exist. Therefore, the plane stress assumption is not valid for a single crystal material. The plane strain assumption also relies on isotropic material conditions and can be applied when the out of plane strain is zero. A typical application where the plane strain assumption is applied is a hollow cylinder, in which the radial strain is assumed to be zero when the length of the cylinder is sufficient. However, for anisotropic single crystal materials the strain is

greatly affected by the material orientation. The simplified stress tensor matrix (Eq. 2-8) is valid only when the specimen is loaded parallel the FCC lattice edges (Swanson and Arakere, 2000). Assuming the direction of their test specimens is accurate, Schulson and Xu may use this basic transformation. However, the true component stresses will have out-of-plane components; therefore plane stress is not valid. Using Eq. 2-5 the strain is equal to the stress tensor matrix multiplied by the stress:

$$\begin{array}{rcl}
 \epsilon_x & a_{11} & a_{12} & a_{12} & 0 & 0 & 0 & \sigma_x \\
 \epsilon_y & a_{12} & a_{11} & a_{12} & 0 & 0 & 0 & \sigma_y \\
 \epsilon_z & a_{12} & a_{12} & a_{11} & 0 & 0 & 0 & \sigma_z \\
 \gamma_{yz} & 0 & 0 & 0 & a_{44} & 0 & 0 & \tau_{yz} \\
 \gamma_{zx} & 0 & 0 & 0 & 0 & a_{44} & 0 & \tau_{zx} \\
 \gamma_{xy} & 0 & 0 & 0 & 0 & 0 & a_{44} & \tau_{xy}
 \end{array} = \quad (2-13)$$

$$\begin{array}{rcl}
 \epsilon_x & a_{11} \cdot \sigma_x + a_{12} \cdot \sigma_y + a_{12} \cdot \sigma_z \\
 \epsilon_y & a_{12} \cdot \sigma_x + a_{11} \cdot \sigma_y + a_{12} \cdot \sigma_z \\
 \epsilon_z & a_{12} \cdot \sigma_x + a_{12} \cdot \sigma_y + a_{11} \cdot \sigma_z \\
 \gamma_{yz} & a_{44} \cdot \tau_{yz} \\
 \gamma_{zx} & a_{44} \cdot \tau_{zx} \\
 \gamma_{xy} & a_{44} \cdot \tau_{xy}
 \end{array} = \quad (2-14)$$

Since out of plane strain is present ( $\epsilon_z$ ,  $\gamma_{zx}$ ,  $\gamma_{yz}$ ) the plane strain assumption is not valid.

Cuitino and Ortiz (1996) also came to this conclusion after observing differing stress fields at the interior and surface of their FEM, as well as slip that would produce out of plane strains.

Using the plane stress and plane strain assumptions, Schulson and Xu calculated two sets of resolved shear stresses for the 12 primary “easy slip” systems. They then normalized these resolved shear stresses with respect to  $K_I$ , the mode I stress intensity

factor, and  $r$ , the radial distance from the tip. Plotting the normalized shear stresses against the angular displacement from the notch tip resulted in a series of shifting maximum stresses, corresponding to the different sectors (Figure 2-15 and Figure 2-16). Although they achieved similar slip system results for each assumption (Table 2-7), the exact systems differ in certain sectors (II, III, IV, V), and the sector angles are very different in some cases (I/II, IV/V). The sector I slip systems are equal under both assumptions, but the stress is different. The difference in the specific slip systems in

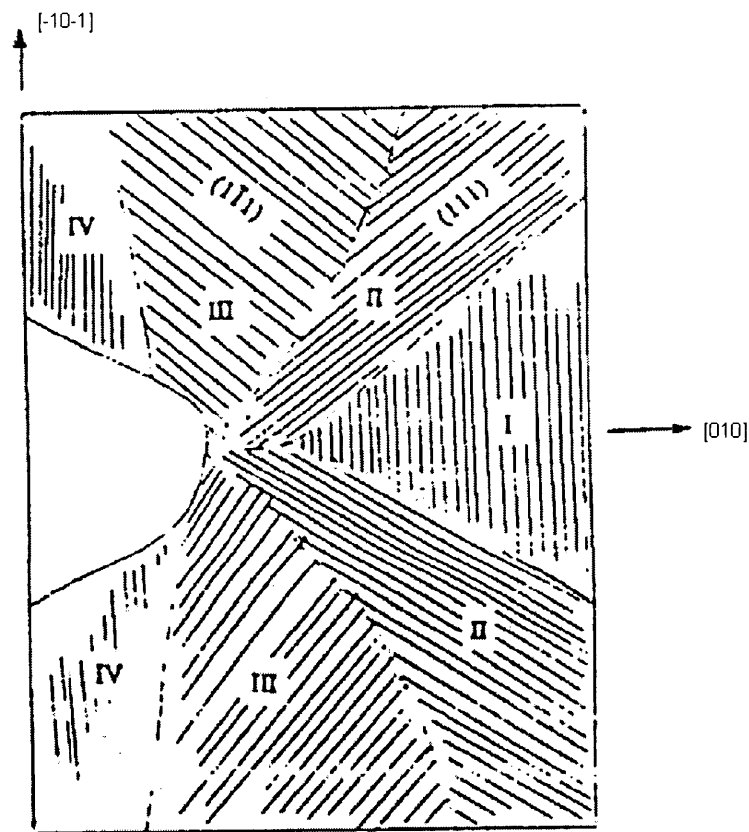


Figure 2-15 Slip sectors under  $[-10-1]$  load. Actual experimental results.  
Source: Modified from Schulson and Xu, 1997.

sectors II-III is of interest, but the systems under plane strain are merely the symmetrical

systems from those of plane stress, except IIb. In sector IV however, although the maximum stresses are resolved onto the same planes, the directions do not match between the two conditions. Finally, in sector V the plane strain stresses jump back to

Table 2-7 Slip sectors for plane stress and plane strain assumptions.

Sector	Plane Stress		Plane Strain	
	$\theta$ (deg)	slip systems	$\theta$ (deg)	slip systems
I	0-43	(11-1)[-110] (-111)[01-1]	0-23	(11-1)[-110] (-111)[01-1]
II	43-60	(111)[1-10] (111)[01-1]	23-60	(-1-1-1)[-110] (-1-1-1)[01-1]
III	60-103	(1-11)[110] (1-11)[011]	60-107	(-11-1)[-1-10] (-11-1)[0-1-1]
IV	103-180	(11-1)[011] (-111)[110]	107-133	(11-1)[101] (-111)[101]
V	--	--	133-180	(-1-1-1)[0-11]

Source: Modified from Schulson and Xu, 1996.

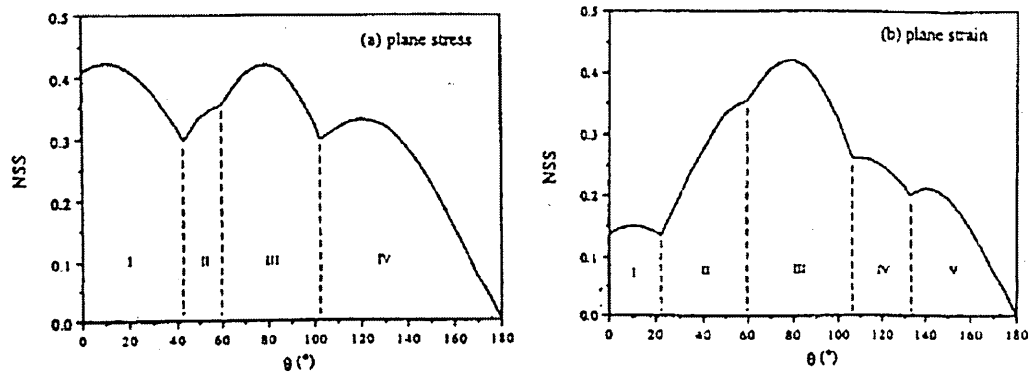


Figure 2-16 Maximum RSS slip system plots. Note the difference between the plane stress and plane strain assumptions.

Source: Schulson and Xu, 1997.

the  $\{111\}$  systems, as in sector II, yet at these same angles the plane stress is still on the  $\{-111\}$  planes (Table 2-7). The data correlates well for the elastic region, the “early slip” (sectors II and III) between approximately  $43-100^\circ$ , but greatly diverges in stress level in



sectors I, I/II, and IV/V. Although Schulson and Xu use alternate assumptions of plane stress and plane strain for their component stress calculations under isotropic conditions, the close agreement between the two predicts initial slip on the  $\{111\}$  and  $\{-111\}$  planes.

Table 2-8 Slip sectors for plane stress and experimental results.

Sector	Plane Stress		Sector	Experimental	
	$\theta$ (deg)	slip systems		$\theta$ (deg)	slip systems
I	0-43	(11-1)[-110] (-111)[01-1]	I	0-38	(11-1)
II	43-60	(111)[1-10] (111)[01-1]	II	38-58	(111)
III	60-103	(1-11)[110] (1-11)[011]	III	58-100	(1-11)
IV	103-180	(11-1)[011] (-111)[110]	IV	100-notch	(11-1)

Source: Modified from Schulson and Xu, 1996.

Experimental results after significant plastic deformation reveal results that deviate from those predicted by either plane stress or plane strain, but are remarkably closer to the plane stress assumption (Table 2-8). Note, under the plane stress assumption, out-of-plane strain is still present. Sectors II and III underwent early slip nearly equally in both the  $+\theta$  and  $-\theta$  half-planes (which are symmetrical), with Sectors I and IV being activated at later stages. Although the slip plane family can be determined visually, some specific slip systems appear the same at the surface; in these cases transmission electron microscopy (TEM) must be employed to detect the specific slip system. Using TEM at the II/III boundary, Schulson and Xu observed [01-1] and [011] dislocations, which confirms the good correlation to the plane stress model.

Noting the scarcity of work in this field Shield (1996) calls for further experiments, particularly in pure tensile testing (versus three/four-point bending), to

observe the details of the applied stress on the strain field. Also of interest is the observation of slip activity ahead of the notch, versus at large angles from the notch tip; numerical calculations predict plasticity in both regions, but Shield observed a higher degree of plasticity largely ahead of the notch tip. An ideal test would incorporate parameters for specimen size, type of test, plasticity, hardening, lattice rotation, etc., and eventually a fatigue crack rather than a notch. However, before incorporating such complexity the basic model must be better understood. Based on the assumption that stress and strain fields will correlate well, and on the assumption that yielding is a stress-controlled process alone (CRSS), this thesis builds off previous work by introducing an elastic analysis of a notched single crystal superalloy material. The resulting resolved shear stresses predict active slip systems and can be used to determine sector boundaries. The model presented here also branches into the tensile testing setup, verses the major bending models created thus far.

## CHAPTER 3

### ANALYTICAL PROCEDURE

This study's goal is to find the state of stress in the material coordinate system of a notched single crystal superalloy test specimen, and then use those stresses to calculate the resolved shear stresses in the 12 primary slip systems. For an isotropic material a single elastic constant governs the transformation from stress to strain (Eq. 2-5). However, the elasticity of an anisotropic material is not constant, and analyzing the stress and strain fields in a single crystal material must first begin with determining the specific material properties in a desired orientation. The stress-strain relation for an anisotropic solid with cubic symmetry has three independent constants in the material coordinate system, as well as a "stress tensor matrix," instead of a single elasticity constant, that varies with orientation. Since test specimen orientation can vary, we need requisite equations to convert between the specimen and material coordinate systems.

#### Coordinate System Transformation

The first step in defining the elasticity matrix is to determine the precise orientation of the actual specimen, either in terms of the material Miller indices (direction indices) or angular measurements. In a physical material test specimen, it is nearly impossible to cut a sample such that the x, y, and z test axes are perfectly aligned to the material axes: [100], [010] and [001] respectively. Therefore, a transformation is needed to convert the known specimen stresses to the material coordinate system. The applied

stresses are a measure of force per unit area, and are a product of the slip plane geometry. In other words, the stresses vary by slip plane and direction according to a particular plane's cross-sectional area and its given orientation within a unit cube of the material. Therefore, these stresses are not affected by anisotropy. However, only two material properties are independent without anisotropic effects; the shear coupling induced in the three-dimensional model, and resulting component stresses, will not be properly accounted for without the third independent constant to define the single crystal material. Lekhnitskii's book on the *Theory of Elasticity of an Anisotropic Elastic Body* is a good reference on this subject.

The transformation equations presented here follow the procedures outlined in Lekhnitskii (1963) and Stouffer and Dame (1996). The transformation from the specimen to the material coordinate system can be accomplished by two methods. In the first approach, the angles between the original and transformed coordinate systems may be directly measured to find the direction cosines. This method is preferable if the angles are easily found. The second method, based on rigid body rotations, may be used for more complex orientations, where the angles between the two coordinate systems are not as obvious; here the Miller indices of the transformed axes must be known. In this process, the axes are rotated through a series of steps to arrive at the final transformed destination. As far as preference, neither method is more correct than the other, but in experimental specimens it is often quite difficult to determine the exact Miller indices; and it can be more convenient to measure the angles.

Coordinate transformations may be performed as long as the orientation of the sample is known, and the transformation matrices can then be used to determine the

stresses and strains resolved on any given plane or slip system. The original coordinate system will be defined as the material coordinate system:  $x_o = [100]$ ,  $y_o = [010]$ , and  $z_o = [001]$  (Figure 3-1). The transformed coordinate system is defined as the specimen coordinate system, and is offset by some angular displacement from the original axes. The specimen axes are denoted by  $x''$ ,  $y''$  and  $z''$ ; all properties associated with the offset system are also denoted by the double-prime symbol.

### Three-Step Coordinate Axes Transformation

As noted above, the initial, or material, coordinate system is denoted by  $x_o$ ,  $y_o$ , and  $z_o$ -axes:

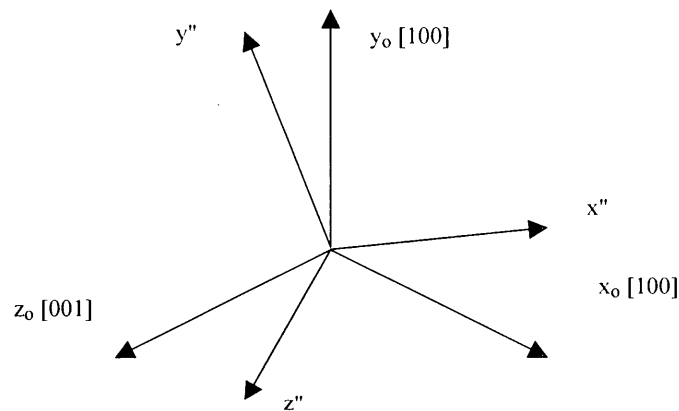


Figure 3-1 Material ( $x_o$ ,  $y_o$ ,  $z_o$ ) and specimen ( $x''$ ,  $y''$ ,  $z''$ ) coordinate systems.

The easiest way to complete the total transformation to the specimen coordinate system is to break it into several rigid body rotations; here we will use a three-step process. The first transformation, to the  $x$ ,  $y$  and  $z$  axes, is performed by rotating by  $\psi_o$  about the  $z_o$ -axis (positive is defined as  $x_o$  toward  $y_o$ ) (Figure 3-2).

$y_o [010]$

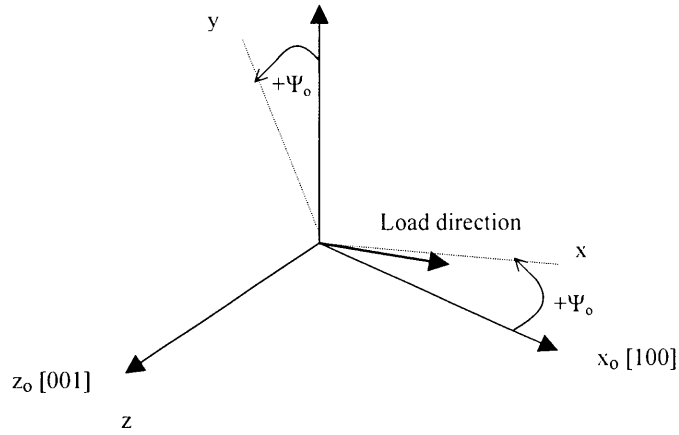


Figure 3-2 First rotation about the  $z_0$ -axis.

Looking at the x-y projection clarifies the direction cosines needed to move from the original to the rotated system (Figure 3-3).

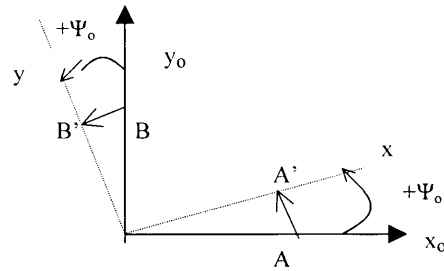


Figure 3-3 Original and rotated axes projection.

The transformed coordinates, in terms of the original coordinates, are:

$$x = x_0 \cdot \cos(\psi_0) + y_0 \cdot \sin(\psi_0) \quad (3-1)$$

$$y = -x_0 \cdot \sin(\psi_0) + y_0 \cdot \cos(\psi_0) \quad (3-2)$$

$$z = z_0 \quad (3-3)$$

Writing the transformation for step one in matrix form is:

$$\begin{matrix} x \\ y \\ z \end{matrix} = \begin{bmatrix} \cos(\psi_0) & \sin(\psi_0) & 0 \\ -\sin(\psi_0) & \cos(\psi_0) & 0 \\ 0 & 0 & 1 \end{bmatrix} \begin{matrix} x_0 \\ y_0 \\ z_0 \end{matrix} \quad (3-4)$$

The second transformation, to the  $x'$ ,  $y'$  and  $z'$  axes, is accomplished by reflecting the load vector onto the  $x$ - $z$  plane and rotating  $\psi_1$  about the  $y$ -axis (positive defined as  $z$  toward  $x$ ) (Figure 3-4).

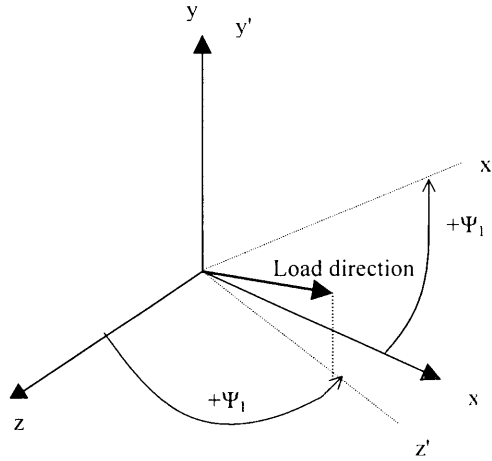


Figure 3-4 Second rotation about the  $y$ -axis.

Following the same process as step one, the second transformation in matrix form is:

$$\begin{matrix} x' \\ y' \\ z' \end{matrix} = \begin{bmatrix} \cos(\psi_1) & 0 & -\sin(\psi_1) \\ 0 & 1 & 0 \\ \sin(\psi_1) & 0 & \cos(\psi_1) \end{bmatrix} \begin{matrix} x \\ y \\ z \end{matrix} \quad (3-5)$$

The final transformation to the specimen coordinate system, or the  $x''$ ,  $y''$  and  $z''$  axes, occurs by rotating the  $y'$  and  $z'$ -axes by  $\psi_2$  about the  $x'$ -axis (positive defined as  $y'$  toward  $z'$ ) (Figure 3-5).

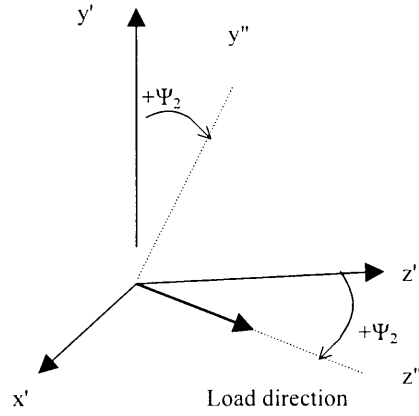


Figure 3-5 Third rotation about the x'-axis.

The third transformation in matrix form is:

$$\begin{matrix} x'' & 1 & 0 & 0 & x' \\ y'' & = & 0 & \cos(\psi_2) & \sin(\psi_2) & y' \\ z'' & & 0 & -\sin(\psi_2) & \cos(\psi_2) & z' \end{matrix} \quad (3-6)$$

The total transformation can then be calculated by multiplying the three individual step matrices together (Note: the first transformation becomes the last one multiplied):

$$\begin{matrix} x'' & \alpha_1 & \beta_1 & \gamma_1 & x_0 \\ y'' & = & \alpha_2 & \beta_2 & \gamma_2 & y_0 \\ z'' & & \alpha_3 & \beta_3 & \gamma_3 & z_0 \end{matrix} \quad (3-7)$$

where

$$\begin{matrix} \alpha_1 & \beta_1 & \gamma_1 & 1 & 0 & 0 & \cos(\psi_1) & 0 & -\sin(\psi_1) & \cos(\psi_0) & \sin(\psi_0) & 0 \\ \alpha_2 & \beta_2 & \gamma_2 & = & 0 & \cos(\psi_2) & \sin(\psi_2) & 0 & 1 & 0 & -\sin(\psi_0) & \cos(\psi_0) & 0 \\ \alpha_3 & \beta_3 & \gamma_3 & & 0 & -\sin(\psi_2) & \cos(\psi_2) & \sin(\psi_1) & 0 & \cos(\psi_1) & 0 & 0 & 1 \end{matrix} \quad (3-8)$$

The resulting values represent the cosines of the angles between the material and specimen coordinate system axes (Table 3-1).



Table 3-1 Direction Cosines

	$x_o$	$y_o$	$z_o$
$x''$	$\alpha_1$	$\beta_1$	$\gamma_1$
$y''$	$\alpha_2$	$\beta_2$	$\gamma_2$
$z''$	$\alpha_3$	$\beta_3$	$\gamma_3$

Solving for the direction cosines, or the final transformation matrix:

$$\alpha_1 \quad \beta_1 \quad \gamma_1$$

$$\alpha_2 \quad \beta_2 \quad \gamma_2 = \mathbf{I}$$

$$\alpha_3 \quad \beta_3 \quad \gamma_3$$

$$\begin{array}{ccc} \cos(\psi_1) \cdot \cos(\psi_0) & \cos(\psi_1) \cdot \sin(\psi_0) & -\sin(\psi_1) \\ \sin(\psi_2) \cdot \sin(\psi_1) \cdot \cos(\psi_0) - \cos(\psi_2) \cdot \sin(\psi_0) & \sin(\psi_2) \cdot \sin(\psi_1) \cdot \sin(\psi_0) + \cos(\psi_2) \cdot \cos(\psi_0) & \sin(\psi_2) \cdot \cos(\psi_1) \\ \cos(\psi_2) \cdot \sin(\psi_1) \cdot \cos(\psi_0) + \sin(\psi_2) \cdot \sin(\psi_0) & \cos(\psi_2) \cdot \sin(\psi_1) \cdot \sin(\psi_0) - \sin(\psi_2) \cdot \cos(\psi_0) & \cos(\psi_2) \cdot \cos(\psi_1) \end{array} \quad (3-9)$$

When fewer than three steps are used, the selection of primary and secondary rotation axes is somewhat arbitrary and it is important to verify the results. Several checks based on perpendicularity can be calculated to ensure a proper orthogonal coordinate transformation has been performed (Appendix A).

### Example Transformation

To illustrate a two-step transformation we will consider a load applied in the [213] direction (Figure 3-6). This transformation is reduced to two steps by eliminating the first

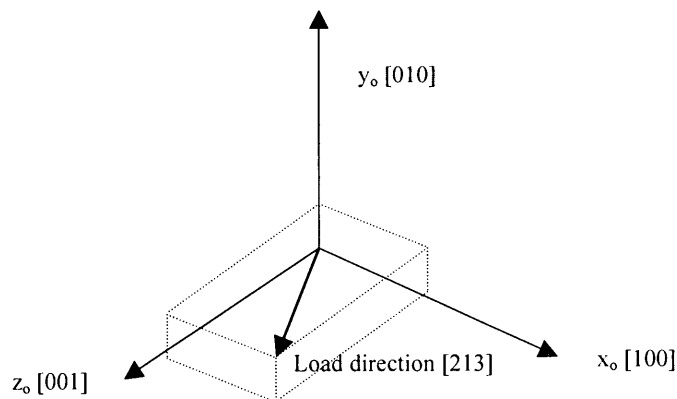


Figure 3-6 Load in the [213] direction.

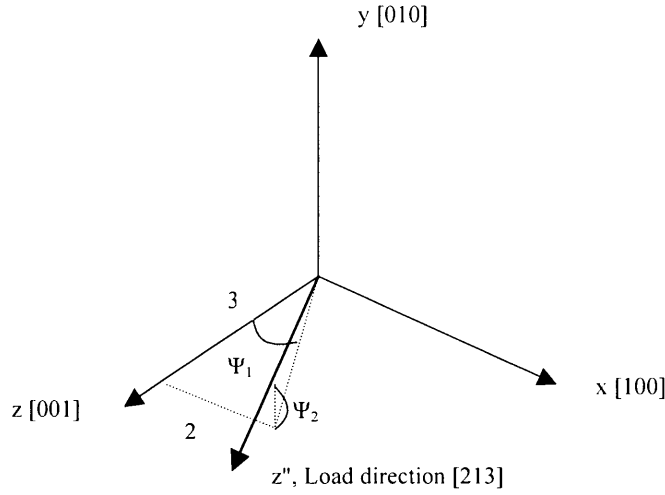


Figure 3-7 Two step coordinate transformation.

step (i.e.  $\psi_0 = 0$ ), and step two begins by reflecting the load vector onto the x-z plane.

The reflection shows a triangle whose sides are the x and z Miller indices:  $x = 2$ ,  $z = 3$ .

The first angular translation,  $\psi_1$ , is:

$$\psi_1 = \text{atan} \frac{2}{3} \quad (3-10)$$

$$\psi_1 = 33.69^\circ$$

In the same way, the second angle,  $\psi_2$ , forms a triangle with the hypotenuse,  $h$ , of the first

reflection and the y-translation:  $h = \sqrt{13}$ ,  $y = 1$ . Therefore, the second angular translation

is:

$$\psi_2 = \text{atan} \frac{1}{\sqrt{13}} \quad (3-11)$$

$$\psi_2 = 15.50^\circ$$

(Note:  $\psi_2$  must be negative for the [213] orientation.) Solving for the direction cosines:

$$\begin{matrix} \alpha_1 & \beta_1 & \gamma_1 \\ \alpha_2 & \beta_2 & \gamma_2 \\ \alpha_3 & \beta_3 & \gamma_3 \end{matrix} = \begin{matrix} 1 & 0 & 0 \\ 0 & \cos(\psi_2) & \sin(\psi_2) \\ 0 & -\sin(\psi_2) & \cos(\psi_2) \end{matrix} \cdot \begin{matrix} \cos(\psi_1) & 0 & -\sin(\psi_1) \\ 0 & 1 & 0 \\ \sin(\psi_1) & 0 & \cos(\psi_1) \end{matrix} \quad (3-12)$$

$$\begin{matrix} \alpha_1 & \beta_1 & \gamma_1 \\ \alpha_2 & \beta_2 & \gamma_2 \\ \alpha_3 & \beta_3 & \gamma_3 \end{matrix} = \begin{matrix} 0.832 & 0 & -0.555 \\ -0.148 & 0.964 & -0.222 \\ 0.535 & 0.267 & 0.802 \end{matrix}$$

Following Appendix A all accuracy checks confirm a proper orthogonal transformation.

### Stress and Strain Transformation

Once the direction cosines between the material and specimen coordinate axes are known, the load conditions can be applied and incorporated into separate matrices to correctly transform the individual stresses and strains. These transformed matrices are then used to solve for the resolved stresses and strains in each desired slip system.

Following Lekhnitskii (1963) the stress transformation is:

$$\{\sigma''\} = [Q']\{\sigma\} \quad (3-13)$$

$$\{\sigma\} = [Q']^{-1}\{\sigma''\} = [Q]\{\sigma''\} \quad (3-14)$$

Here  $[Q]$  is the stress transformation matrix, a function of the direction cosines:

$$\begin{aligned}
[Q] = & \begin{matrix} \alpha_1^2 & \alpha_2^2 & \alpha_3^2 & 2\alpha_3\alpha_2 & 2\alpha_1\alpha_3 & 2\alpha_2\alpha_1 \\ \beta_1^2 & \beta_2^2 & \beta_3^2 & 2\beta_3\beta_2 & 2\beta_1\beta_3 & 2\beta_2\beta_1 \\ \gamma_1^2 & \gamma_2^2 & \gamma_3^2 & 2\gamma_3\gamma_2 & 2\gamma_1\gamma_3 & 2\gamma_2\gamma_1 \\ \beta_1\gamma_1 & \beta_2\gamma_2 & \beta_3\gamma_3 & (\beta_2\gamma_3 + \beta_3\gamma_2) & (\beta_1\gamma_3 + \beta_3\gamma_1) & (\beta_1\gamma_2 + \beta_2\gamma_1) \\ \gamma_1\alpha_1 & \gamma_2\alpha_2 & \gamma_3\alpha_3 & (\gamma_2\alpha_3 + \gamma_3\alpha_2) & (\gamma_1\alpha_3 + \gamma_3\alpha_1) & (\gamma_1\alpha_2 + \gamma_2\alpha_1) \\ \alpha_1\beta_1 & \alpha_2\beta_2 & \alpha_3\beta_3 & (\alpha_2\beta_3 + \alpha_3\beta_2) & (\alpha_1\beta_3 + \alpha_3\beta_1) & (\alpha_1\beta_2 + \alpha_2\beta_1) \end{matrix} \quad (3-15)
\end{aligned}$$

The state of stress is defined in terms of the specimen  $\{\sigma\}$  or material  $\{\sigma''\}$  stresses by:

$$\begin{aligned}
\{\sigma\} = & \begin{matrix} \sigma_x \\ \sigma_y \\ \sigma_z \\ \tau_{yz} \\ \tau_{zx} \\ \tau_{xy} \end{matrix} \quad \{\sigma''\} = \begin{matrix} \sigma'_x \\ \sigma'_y \\ \sigma'_z \\ \tau'_{yz} \\ \tau'_{zx} \\ \tau'_{xy} \end{matrix} \quad (3-16)
\end{aligned}$$

The strain transformation is carried out in much the same manner:

$$\{\epsilon''\} = [Q'_\epsilon]\{\epsilon\} \quad (3-17)$$

$$\{\epsilon\} = [Q'_\epsilon]^{-1}\{\epsilon''\} = [Q_\epsilon]\{\epsilon''\} \quad (3-18)$$

The strain transformation matrix,  $[Q_\epsilon]$ , is also a function of the direction cosines, but differs from the stress matrix,  $[Q]$ :

$$\begin{aligned}
[Q_\epsilon] = & \begin{matrix} \alpha_1^2 & \alpha_2^2 & \alpha_3^2 & \alpha_3\alpha_2 & \alpha_1\alpha_3 & \alpha_2\alpha_1 \\ \beta_1^2 & \beta_2^2 & \beta_3^2 & \beta_3\beta_2 & \beta_1\beta_3 & \beta_2\beta_1 \\ \gamma_1^2 & \gamma_2^2 & \gamma_3^2 & \gamma_3\gamma_2 & \gamma_1\gamma_3 & \gamma_2\gamma_1 \\ 2\beta_1\gamma_1 & 2\beta_2\gamma_2 & 2\beta_3\gamma_3 & (\beta_2\gamma_3 + \beta_3\gamma_2) & (\beta_1\gamma_3 + \beta_3\gamma_1) & (\beta_1\gamma_2 + \beta_2\gamma_1) \\ 2\gamma_1\alpha_1 & 2\gamma_2\alpha_2 & 2\gamma_3\alpha_3 & (\gamma_2\alpha_3 + \gamma_3\alpha_2) & (\gamma_1\alpha_3 + \gamma_3\alpha_1) & (\gamma_1\alpha_2 + \gamma_2\alpha_1) \\ 2\alpha_1\beta_1 & 2\alpha_2\beta_2 & 2\alpha_3\beta_3 & (\alpha_2\beta_3 + \alpha_3\beta_2) & (\alpha_1\beta_3 + \alpha_3\beta_1) & (\alpha_1\beta_2 + \alpha_2\beta_1) \end{matrix} \quad (3-10)
\end{aligned}$$

According to Hooke's law, an isotropic material's stress and strain for a uniaxial state of stress are related by:

$$\sigma = E \cdot \epsilon \quad (3-20)$$

The generalized Hooke's law for a homogeneous anisotropic body is:

$$\{\sigma\} = [A_{ij}] \{\epsilon\} \quad (3-21)$$

where the  $[a_{ij}]$  and  $[A_{ij}]$  matrices are the elastic constant matrices and:

$$[A_{ij}] = [a_{ij}]^{-1} \quad (3-22)$$

and  $[a_{ij}]$  is a symmetric matrix such that:

$$[a_{ij}] = [a_{ji}] \quad (3-23)$$

Therefore

$$\{\epsilon\} = [a_{ij}] \{\sigma\} \quad (3-24)$$

and

$$\{\epsilon''\} = [a'_{ij}] \{\sigma''\} \quad (3-25)$$

The elasticity matrix also undergoes transformation, but it remains symmetric. A maximum of 21 individual constants may be present, depending on the specimen orientation:

$$[a'_{ij}] = [Q]^T [a_{ij}] [Q] \quad (3-26)$$

Now, once the component stresses are known in the specimen coordinate system, the above equations can be applied to solve for the component stresses in the material coordinate system.

### Slip System Shear Stresses and Strains

The component stresses define the complete state of stress of the material, but these values alone reveal little about individual slip systems or RSS activity. The 12 primary slip systems (Table 1-1) are defined by both a slip plane and direction. Incorporating their geometry is analogous to performing a separate transformation, and allows all individual resolved shear stresses to be determined.

### Resolved Shear Components

Following Stouffer and Dame (1996), the resolution of stress to the slip systems is calculated:

$$\{\tau\} = c[S]\{\sigma\} \quad (3-27)$$

Here  $c$  and  $[S]$  are constants defined by the slip plane and direction:

$$c_i = \frac{1}{\sqrt{h_i'^2 + k_i'^2 + l_i'^2} \sqrt{u_i'^2 + v_i'^2 + w_i'^2}} \quad (3-28)$$

$$S_i = (h_i' \ u_i' \ k_i' \ v_i' \ l_i' \ w_i' \ -w_i' \ -v_i' \ -u_i') \quad (3-29)$$

Here,  $[u' \ v' \ w']$  is the slip direction and  $(h' \ k' \ l')$  is the slip plane (recall Figure 2-2). For the 12 primary systems,  $c$  is constant and the full RSS matrix becomes:

$$\begin{array}{rcll}
\tau_1 & h'_1 \cdot u'_1 & k'_1 \cdot v'_1 & l'_1 \cdot w'_1 & -w'_1 & -v'_1 & -u'_1 & \\
\tau_2 & h'_2 \cdot u'_2 & k'_2 \cdot v'_2 & l'_2 \cdot w'_2 & -w'_2 & -v'_2 & -u'_2 & \\
\tau_3 & h'_3 \cdot u'_3 & k'_3 \cdot v'_3 & l'_3 \cdot w'_3 & -w'_3 & -v'_3 & -u'_3 & \\
\tau_4 & h'_4 \cdot u'_4 & k'_4 \cdot v'_4 & l'_4 \cdot w'_4 & -w'_4 & -v'_4 & -u'_4 & \sigma_x \\
\tau_5 & h'_5 \cdot u'_5 & k'_5 \cdot v'_5 & l'_5 \cdot w'_5 & -w'_5 & -v'_5 & -u'_5 & \sigma_y \\
\tau_6 & h'_6 \cdot u'_6 & k'_6 \cdot v'_6 & l'_6 \cdot w'_6 & -w'_6 & -v'_6 & -u'_6 & \sigma_z \\
\tau_7 & h'_7 \cdot u'_7 & k'_7 \cdot v'_7 & l'_7 \cdot w'_7 & -w'_7 & -v'_7 & -u'_7 & \tau_{xy} \\
\tau_8 & h'_8 \cdot u'_8 & k'_8 \cdot v'_8 & l'_8 \cdot w'_8 & -w'_8 & -v'_8 & -u'_8 & \tau_{zx} \\
\tau_9 & h'_9 \cdot u'_9 & k'_9 \cdot v'_9 & l'_9 \cdot w'_9 & -w'_9 & -v'_9 & -u'_9 & \tau_{yz} \\
\tau_{10} & h'_{10} \cdot u'_{10} & k'_{10} \cdot v'_{10} & l'_{10} \cdot w'_{10} & -w'_{10} & -v'_{10} & -u'_{10} & \\
\tau_{11} & h'_{11} \cdot u'_{11} & k'_{11} \cdot v'_{11} & l'_{11} \cdot w'_{11} & -w'_{11} & -v'_{11} & -u'_{11} & \\
\tau_{12} & h'_{12} \cdot u'_{12} & k'_{12} \cdot v'_{12} & l'_{12} \cdot w'_{12} & -w'_{12} & -v'_{12} & -u'_{12} & 
\end{array} = c \cdot \quad (3-30)$$

Solving Eq. 3-30 for the 12 primary systems:

$$\begin{array}{rcll}
\tau_1 & & & \\
\tau_2 & 1 & 0 & -1 & 1 & 0 & -1 \\
\tau_3 & 0 & -1 & 1 & -1 & 1 & 0 \\
\tau_4 & 1 & -1 & 0 & 0 & 1 & -1 \\
\tau_5 & -1 & 0 & 1 & 1 & 0 & -1 \\
\tau_6 & -1 & 1 & 0 & 0 & -1 & -1 \\
\tau_7 & 0 & 1 & -1 & -1 & -1 & 0 \\
\tau_8 & 1 & -1 & 0 & 0 & -1 & -1 \\
\tau_9 & 0 & 1 & -1 & -1 & 1 & 0 \\
\tau_{10} & 1 & 0 & -1 & -1 & 0 & -1 \\
\tau_{11} & 0 & -1 & 1 & -1 & -1 & 0 \\
\tau_{12} & -1 & 0 & 1 & -1 & 0 & -1 \\
\tau_{11} & -1 & 1 & 0 & 0 & 1 & -1 \\
\tau_{12} & & & & & & 
\end{array} = \frac{1}{\sqrt{6}} \cdot \quad (3-31)$$

The shear strains are calculated in the same way as the stresses outlined above:

$$\{\gamma\} = c[S]\{\epsilon\} \quad (3-32)$$

The stress and strain fields, fully resolved onto the primary octahedral slip systems, are now known and can be used to predict slip within a particular system.



## CHAPTER 4 NUMERICAL SOLUTION: FINITE ELEMENT METHOD

### Finite Element Model

Finite element software can be used to model the specific geometries and orientations of the tensile test specimens of interest (Figure 4-1). Using the ANSYS finite element software (Version 5.7), three different samples were modeled in order to predict slip activity and sectors around the notch. Two of the three orientations are based on previous work (Rice, 1987; Schulson and Xu, 1997; Crone and Shield, 2001) and all three correlate to collaborative work between the Mechanical Engineering and Materials Science Engineering (MSE) departments of the University of Florida (UF). As a stress-

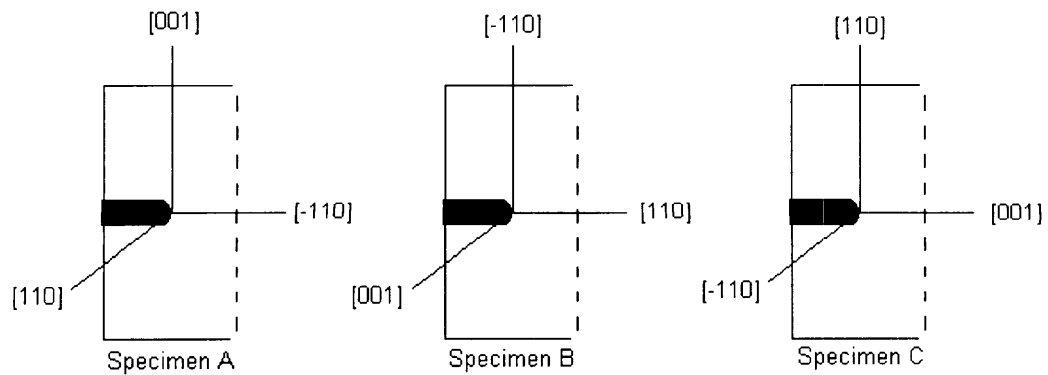


Figure 4-1 Finite element analysis specimens and orientations.

based process, slip deformation should be predicted by the numerical model's highest individual resolved shear stresses. The slip systems that are represented by the highest

resolved shear stresses should then be observable as slip lines in the experimental test samples.

A solid tensile specimen was first modeled with the given load conditions and then compared to the analytical solution outlined in Chapter 3, using MathCad 2000 Professional, to verify the numerical procedure and results. Two notches were then incorporated into the model to represent the experimental test specimens. The finite FEA component stresses were taken from the material coordinate system, around the notch, and then used in the transformation equations to calculate the individual resolved shear stresses. Data was analyzed over a wide range of radial and angular distances to create a complete stress field, later used to draw conclusions on sectors and slip activation.

#### Verifying the Finite Element Model

The complete tensile specimen, without any notches, can be analyzed according to the procedure outlined in Chapter 3 to verify the initial finite element model. Although any model size should result in a correct analytical solution, the same dimensions as those used for the actual specimens (minus notch geometry) were used for consistency. The applied load used for all numerical models is 100 lbs (7028 psi with the specimen cross-sectional area). This load will result in stresses well below the yield point of the material to ensure a purely elastic model. Since the stresses vary linearly with the load, the actual load is not important as long as the material remains in the elastic regime. The initial check gives excellent agreement between for the component stresses (Table 4-1);

Table 4-1 Analytical and numerical component stresses for Specimen A.

$\sigma$ (psi)	$\sigma_x$	$\sigma_y$	$\sigma_z$	$\sigma_{xy}$	$\sigma_{yz}$	$\sigma_{xz}$
Analytical	0	0	7027.9	0	0	0

Numerical	3.6642	3.6643	7028.4	-3.7176	4.86E-03	-2.49E-02
% Error			0.007%			

the percent error is well within acceptable limits, so the initial model affirms an accurate coordinate and stress transformation. Although the stresses attest to an accurate model, a better test of a correct anisotropic model is the component strains, which take the transformed stress tensor matrix into account (Table 4-2). The component strains in the

Table 4-2 Analytical and numerical component strains for Specimen A.

$\epsilon$	$\epsilon_x$	$\epsilon_y$	$\epsilon_z$	$\epsilon_{xy}$	$\epsilon_{yz}$	$\epsilon_{xz}$
Analytical	-1.83E-04	-1.83E-04	4.56E-04	0.00E+00	0.00E+00	0.00E+00
Numerical	-1.83E-04	-1.83E-04	4.56E-04	-2.37E-07	3.09E-10	-1.59E-09
% Error	0.016%	0.016%	0.044%			

material coordinate system again show nearly zero error, affirming a correct numerical model. Each orientation was validated, using the same procedure outlined above, to confirm correct stress and strain transformations before proceeding with the notched model. Incorporating the notch geometry into the existing model will now complete the actual specimen model.

#### Specimen Orientation and Geometry

The three numerical models all utilize the same geometry, including simplified notch geometry, to observe the effects of orientation without other defect/size considerations. The finite element model (FEM) is limited to the body of the specimen, rather than the entire geometry including the end grips. The reason for the abridged model is two-fold: First, the mechanics at the grips are considerably different from the center of the tensile specimen and include the effects of tensile rig contact pressure, loading rate, etc.. In the experimental model, different deformation mechanisms are seen at the grips, and the sample can even fracture there first. The goal here, however, is to

model those specimens which fail at the central area of the specimen and analyze those stresses of interest. Second, in an attempt to gain more accurate results grips may be changed or updated, as is the case currently in the MSE department. The numerical model will not be subject to the type of grip used or any variations it may cause.

The geometry for all three models is based on the experimental counterpart to Specimen A, and was modified to simplify the geometry. Table 4-3 shows the actual specimen geometry of Specimen A, as well as the modifications made for the simplified FEM (Figure 4-2). The notch is modeled as the combination of a perfect rectangle and a perfect semi-circle. In reality the notch will likely have some angular offset with the horizontal, as well as some y-displacement offset from the specimen's center. Also, the actual notch tip is not semicircular, but rather a smaller arc. In the numerical model,

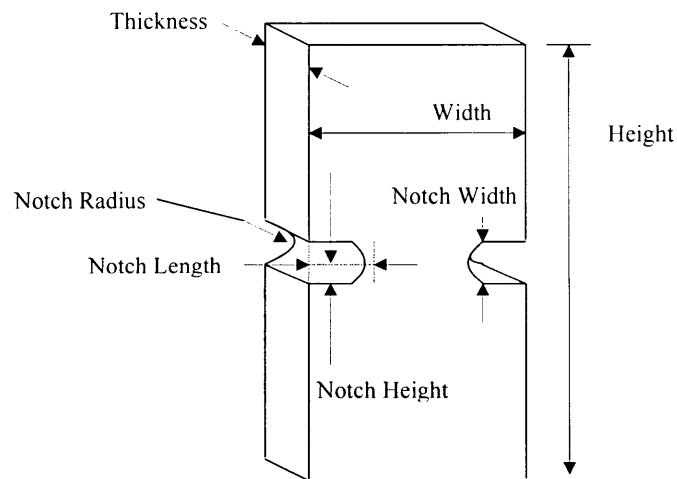


Figure 4-2 Specimen dimensions.

both notch lengths and heights were set equal to those of the largest actual dimension. Additionally, the notch radius was set equal to the notch height (i.e. one-half the width of

the notch) to form a perfect semi-circle. These geometrical simplifications can be easily removed for more specific test results, rather than our general focus on orientation.

Table 4-3 Actual (Specimen A) and finite element specimen geometry.

<b>Specimen Geometry</b>		
(mm)	Actual	FEM
Width	5.100	5.100
Height	19.000	19.000
Thickness	1.800	1.800
Right Notch Length	1.300	1.550
Left Notch Length	1.550	1.550
Right Notch Height	0.113	0.113
Left Notch Height	0.111	0.113
Right Notch Radius	0.045	0.113
Left Notch Radius	0.055	0.113

### Model Characteristics

#### Material Properties

The finite element model is a linear-elastic, orthotropic model. The ANSYS finite element software has several three-dimensional elements available to account for anisotropic or orthotropic material properties. Choosing these elements, and defining either the three necessary independent stress tensors ( $a_{11}$ ,  $a_{12}$ ,  $a_{44}$ ) or the three independent directional properties ( $E$ ,  $G$ , and  $\nu$ ), will accurately model a single crystal material. To calculate the stresses in any direction, the material properties must first be defined within the material coordinate system. In the FEM, the model is created around the global specimen coordinate system (Figure 4-3). Therefore, the proper direction cosines must be used to create the material coordinate system. ANSYS aligns material properties with the element coordinate system; therefore the element coordinate system is

aligned with the material coordinate system so that the directional material properties are suitably applied.

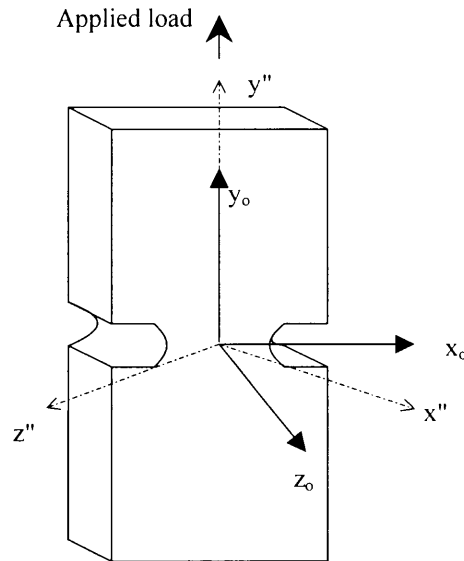


Figure 4-3 Global and material coordinate systems. The specimen is created around the global system  $(x_0, y_0, z_0)$  and the material system  $(x'', y'', z'')$  is later specified.

### Elements and Meshing

The ANSYS elements chosen for the FEM are PLANE2 and SOLID95. After the three-dimensional solid model is created, the front face is meshed with the PLANE2 elements (Figure 4-4). This front face has precise element sizing along the defined radial lines around the notch tip at  $5^\circ$  intervals. The PLANE2 element is a two-dimensional, six-node triangular structural solid. It models irregular structures well and uses accurate quadratic displacement functions (ANSYS 5.7 Elements Reference, 1999). The nodes also incorporate orthotropic material properties, however these nodes are later deleted after serving their sizing function and their material properties are not relevant.

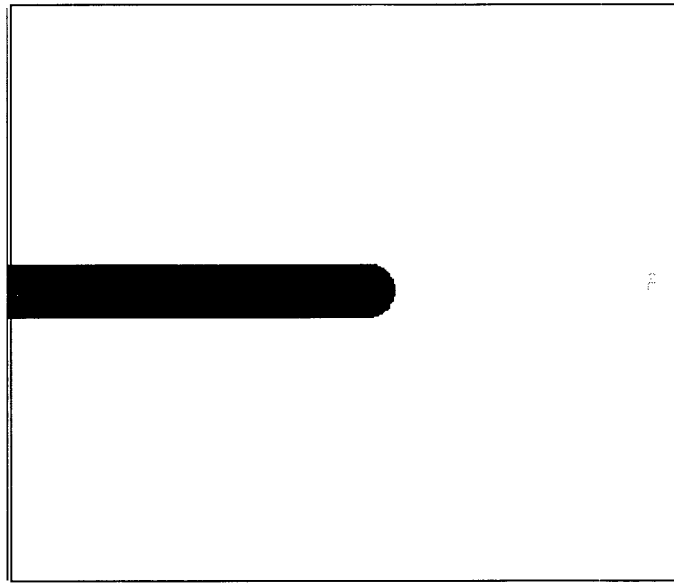


Figure 4-4 Finite element mesh about the notch tip.

Once the front face is meshed, three-dimensional elements are swept through the volume to complete the meshing of the model. Working in conjunction with the two-dimensional elements on the front face, the three-dimensional elements retain their sizing definitions on each of the x-y planes through the specimen's thickness (Figure 4-5). SOLID95 is a three-dimensional structural solid with 20 nodes; each node has three degrees of freedom with translation in the x, y, and z directions (Figure 4-6). It has the same basic structure as the ANSYS SOLID45, but the addition of mid-side nodes enables more accurate solutions near irregular shapes. SOLID95 is preferentially selected for this very reason, since the area around the notch is of the most interest. Also critical is the inclusion of orthotropic material properties, which again correspond to the element coordinate system. The original element structure is left intact, rather than enabling

pyramidal shapes to reduce the solution run time. Although the pyramidal option is less costly it may result in less accurate solutions, especially where there are large stress

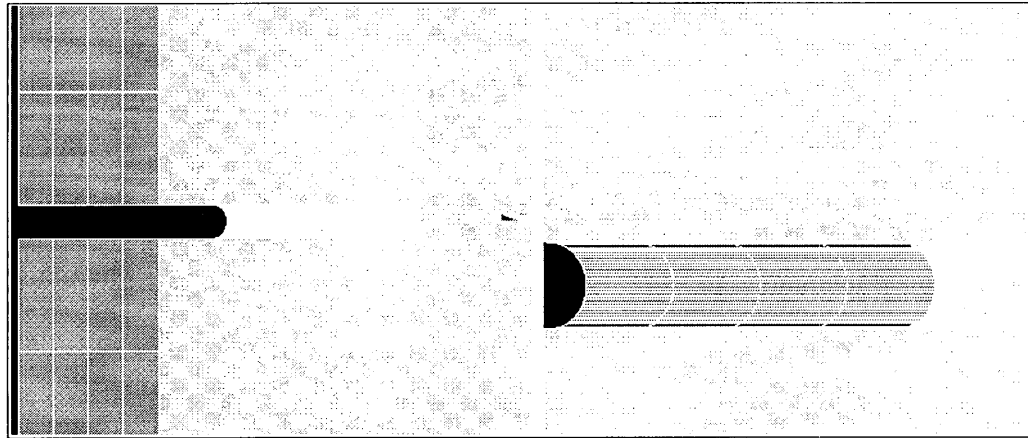


Figure 4-5 Element sizing on the front face and through the thickness. The two dimensional frontal elements are swept through the thickness of the sample to retain guidelines for the three-dimensional elements. Left, showing the edge of the specimen; right, showing the elements through the thickness.

gradients. SOLID95 also supports plasticity, creep, large deflections and large strains among others, and is well suited for further future development of the numerical model.

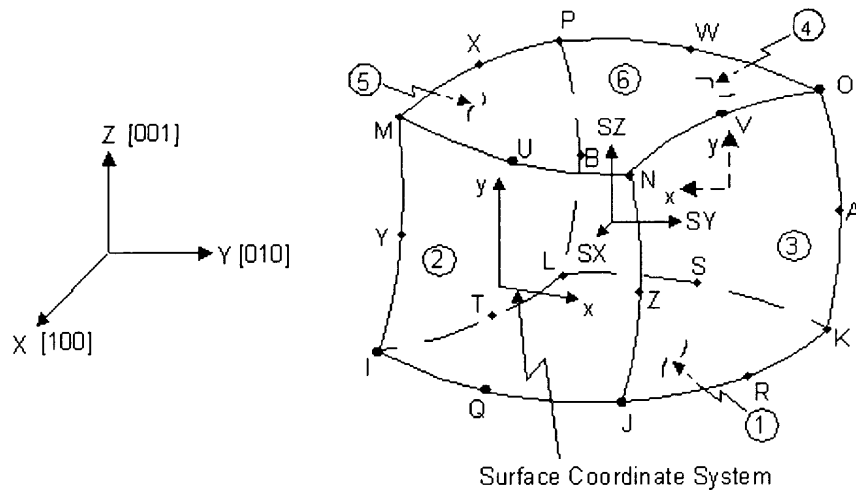


Figure 4-6 ANSYS SOLID95 element.



Source: ANSYS 5.7 Elements Reference, 1999.

As described previously, ANSYS aligns the material properties with the elements, which the model aligns with the material coordinate system. ANSYS then transforms the stress tensor matrix to any desired direction for stress or strain calculations. Due to a weighted nature in the nodal stress solutions, stress calculations are only available at the corner nodes, rather than all corner and mid-side nodes. To observe both the near-field state of stress and those stresses at larger distances from the notch (radial and angular), six concentric arcs were created at the following radii from the notch tip:  $0.25 \cdot \rho$ ,  $0.50 \cdot \rho$ ,  $1.00 \cdot \rho$ ,  $2.00 \cdot \rho$ ,  $3.00 \cdot \rho$ , and  $5.00 \cdot \rho$ ; where  $\rho$  is the notch radius (Figure 4-7 and Figure 1-5). (Note: Initially the  $3.00 \cdot \rho$  arc was not included and a  $10.0 \cdot \rho$  arc was present.

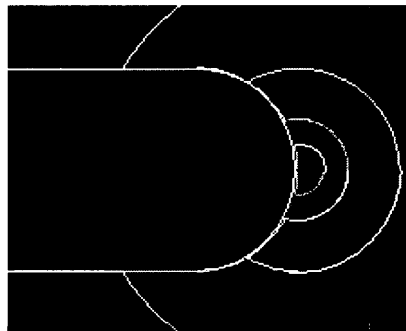


Figure 4-7 Radial arcs used for element location and sizing; centered at the notch tip.

However, the larger arc intersected with its counterpart around the opposing notch. The nodes selected at  $3.00 \cdot \rho$  were not created along a defined radius, but were carefully chosen by hand through the ANSYS Graphical User Interface (GUI).)

### Solution Location

The element sizing of the FEM allows data to be collected on any of five separate x-y planes (Figure 4-5), including the front, middle, and back planes. In the interests of our collaboration with the MSE department, the current focus is on the front surface of the specimen. Here, at the surface, we can observe slip lines and make comparisons to the numerical model. Unlike models that use a plane strain assumption, it is not critical to collect data on the central planes versus another location. The decision to examine the state of stress at the surface is practical both from a mechanics perspective (considering surface effects) and the desire for collaboration.

The nodes that lie on the concentric arcs around the notch tip are selected by first, manually viewing the arcs in the GUI and then, choosing the corresponding nodes from  $0^\circ$  to  $180^\circ$  from the x-axis (toward the y-axis). Calculations do not need to be performed from  $0^\circ$  to  $-180^\circ$ , because the superalloy, an FCC material, exhibits symmetry about the  $\langle 100 \rangle$  and  $\langle 110 \rangle$  axes (see Chapter 2). To check this assumption, stress calculations were performed on Specimen A for the  $0.25 \cdot p$  arc and confirmed the symmetry. For the negative angles, the particular resolved shear stresses change direction, along with the changing direction of shear deformation between the top and lower halves of the test specimen. However, the maximum values of the resolved shear stresses are consistent between the positive and negative angles, as are the planes with those stresses.

### Assumptions

A linear elastic model may predict the initial slip, but cannot precisely predict subsequent behavior due to plasticity around the notch tip. Some other modeling assumptions include low temperature deformation, no account of microstructural (i.e.

dislocation) mechanisms, and no crystal lattice rotation. Finite element analysis is capable of accounting for changing temperature effects. However, in order to simplify the model and collaborate more closely with the MSE department, the FEA applied material properties at a constant (room) temperature. The exclusion of microstructure has also been discussed. The last assumption, however, is valid for this elastic model; crystal lattice rotation generally requires a few percent strain in a single slip system to occur (Stouffer and Dame, 1996) and the load used here is extremely low. The FEA here assumes only elastic deformation, and seeks only elastic stress and strain trends rather than specific values at fracture. Future research can easily build from the current model to incorporate plasticity, as well as creep or other desired behaviors.

## CHAPTER 5 RESULTS AND DISCUSSION

The main purpose of using FEM was to determine the slip activation and resulting sectors for a notched single crystal tensile specimen. Results are presented here for an elastic stress response to the given load on the primary octahedral slip systems about a notch tip, with the RSS as a function of radial and angular position. The absolute values of the resolved shear stresses are used for easy comparison, since the direction is irrelevant for this analysis. As predicted, each of the three orientations shows different slip activation, and at different locations. The determination of sectors is a more complex question than initially indicated by the majority of the literature, and will first be defined as the dominant slip system at any theta (i.e. the system with the highest RSS at any theta). Each orientation will be presented individually at first and then compared with each other.

### Specimen A

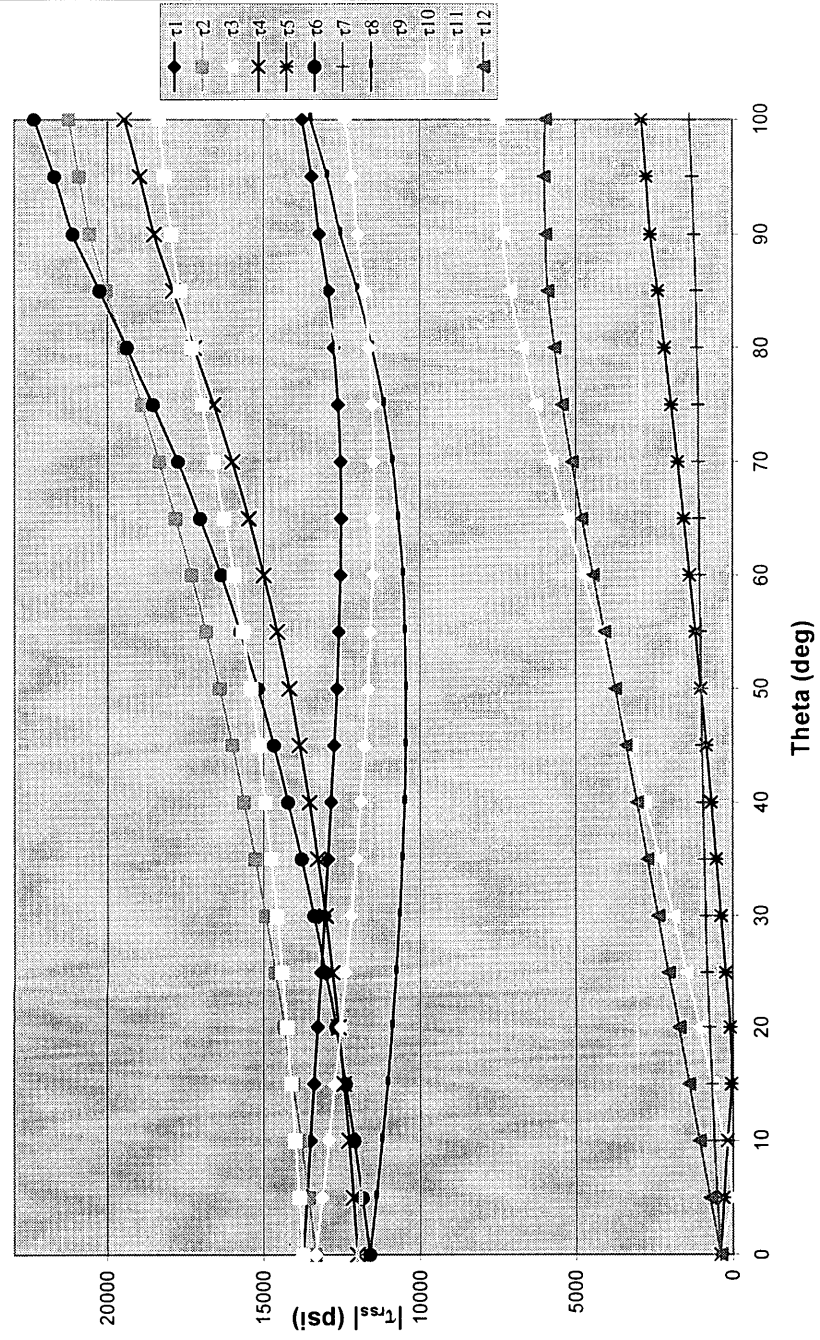
Recall, Specimen A was tested with a [001] load, a [-110] growth direction, and a [110] notch plane (Figure 4-1). The maximum RSS at any location is  $\tau_2=25,000$  psi at  $r = 0.5*\rho$  and  $105^\circ$ , or  $3.56*\sigma_{\text{applied}}$ . Results are presented for the 12 primary RSS values from  $0.25*\rho$  to  $5*\rho$  and from  $0^\circ$  to the top of the notch ( $100^\circ$  for  $0.25*\rho$  up to  $170^\circ$  for  $5*\rho$ ) (Figures 5-1 to 5-6). The slip system with the maximum RSS varies with radial and angular position; sectors were determined for each radius by the overall maximum RSS,

or the dominant slip system (Table 5-1). Notice that for a given angle the dominant system (and often the other activated systems) is not constant over the range of radii. As the state of stress changes away from the notch tip, the RSS also changes; however, each component stress does not change uniformly with the others, so their status relative to each other may change and shift with the magnitude of their stresses. Therefore the dominant slip system is likely to change one or more times for a given theta.

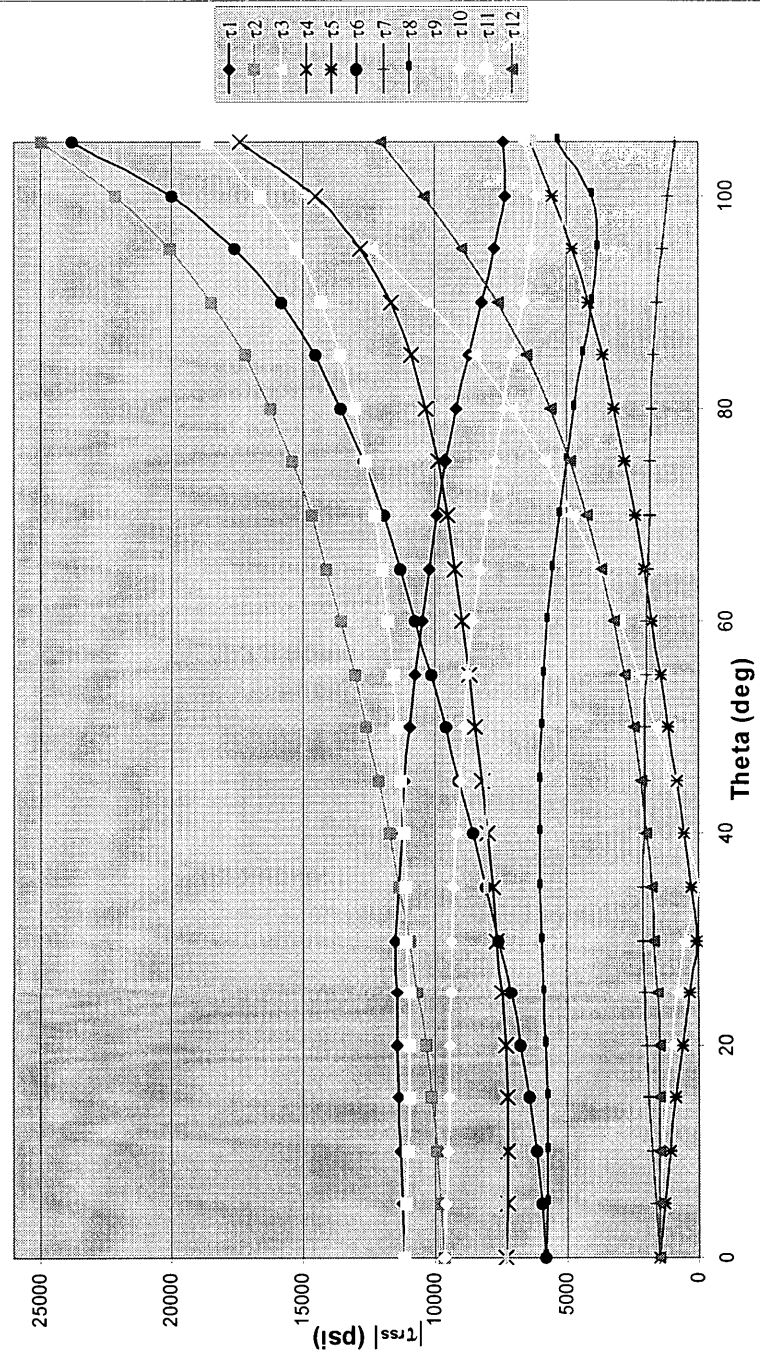
When the RSS is plotted against theta the effect of theta is clearly shown. The effect of radius, on the other hand, can be more clearly seen by combining the results in a single plot with the 12 primary stresses for the entire range of radii (Figure 5-7). The stresses at each radius have been scaled so they appear in ascending order (with respect to radial distance) from the origin. The amount of data can be difficult to interpret, but shows the overall changes well; for more detail the individual radial figures should be investigated. To observe the effect of radius at a given angle, let us look at the RSS changes along  $\theta = 85^\circ$  as an example: at  $r = 0.25 \cdot \rho$ ,  $\tau_6$  is the maximum RSS; however the largest stress quickly shifts to  $\tau_2$  from  $r = 0.5 \cdot \rho$  to  $3 \cdot \rho$ , and then back to  $\tau_6$  at  $r = 5 \cdot \rho$ . Some angles do maintain a single dominant slip system for all radii ( $\tau_2$  at  $57^\circ$ - $68^\circ$  here), but overall the slip systems and sectors are highly variable throughout the RSS field. Overall the RSS field for Specimen A is dominated by  $\tau_1$ ,  $\tau_2$ , and  $\tau_3$  on the (111) plane, and to a lesser extent  $\tau_6$  and  $\tau_{11}$ , both on  $\{-11-1\}$  planes.

Specimen A  
 $r = 0.25 \cdot p$

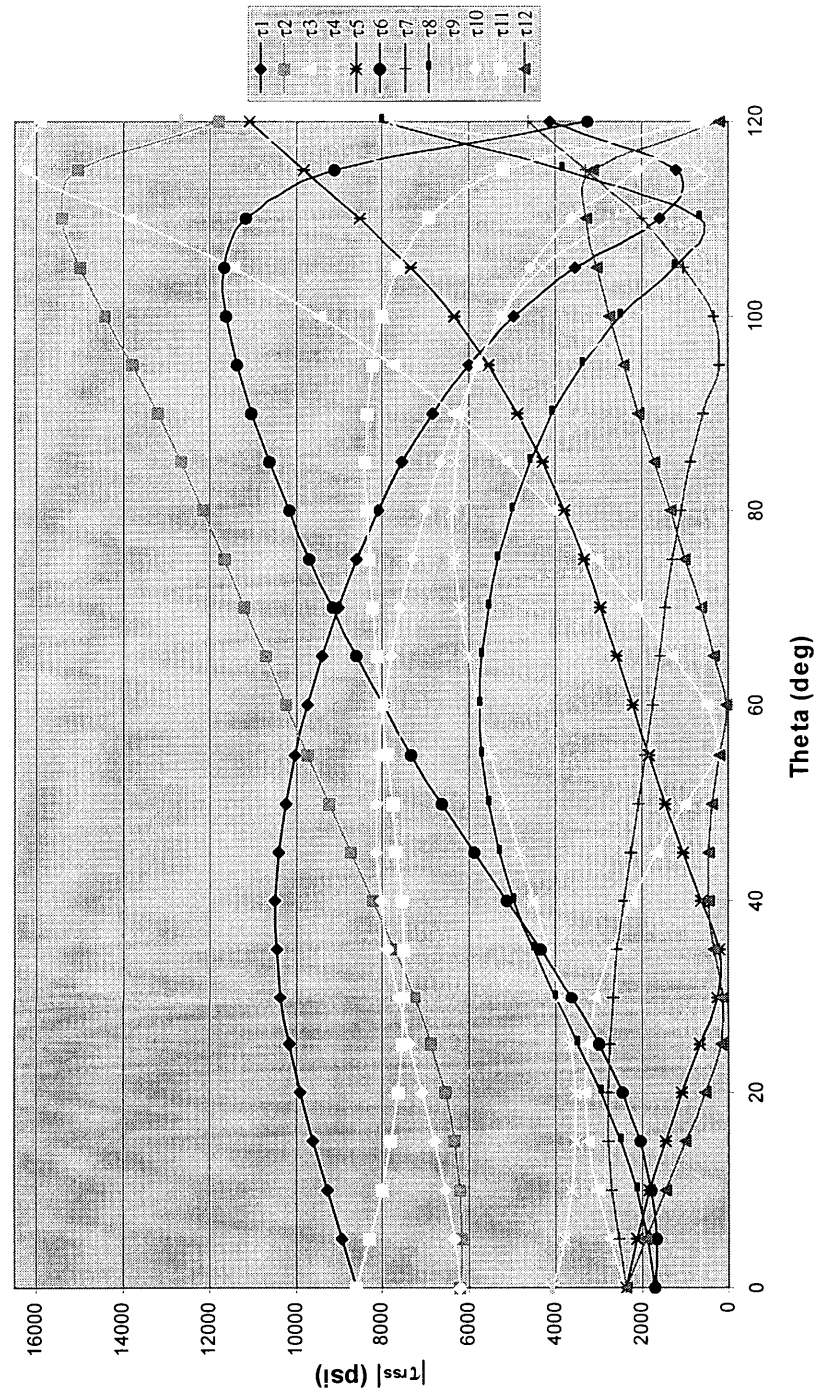
# Resolved Shear Stress v. Theta



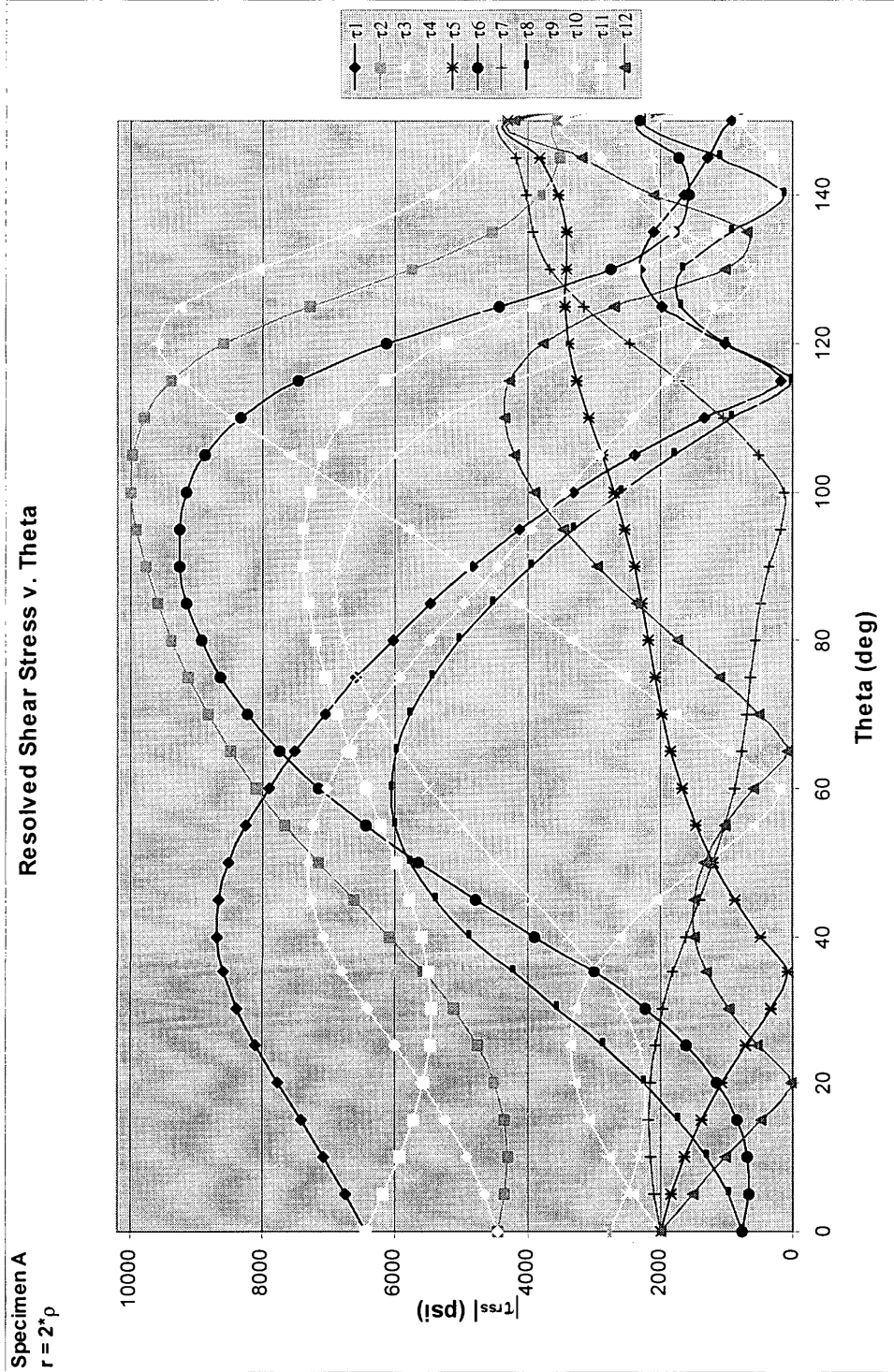
# Resolved Shear Stress v. Theta



Resolved Shear Stress v. Theta

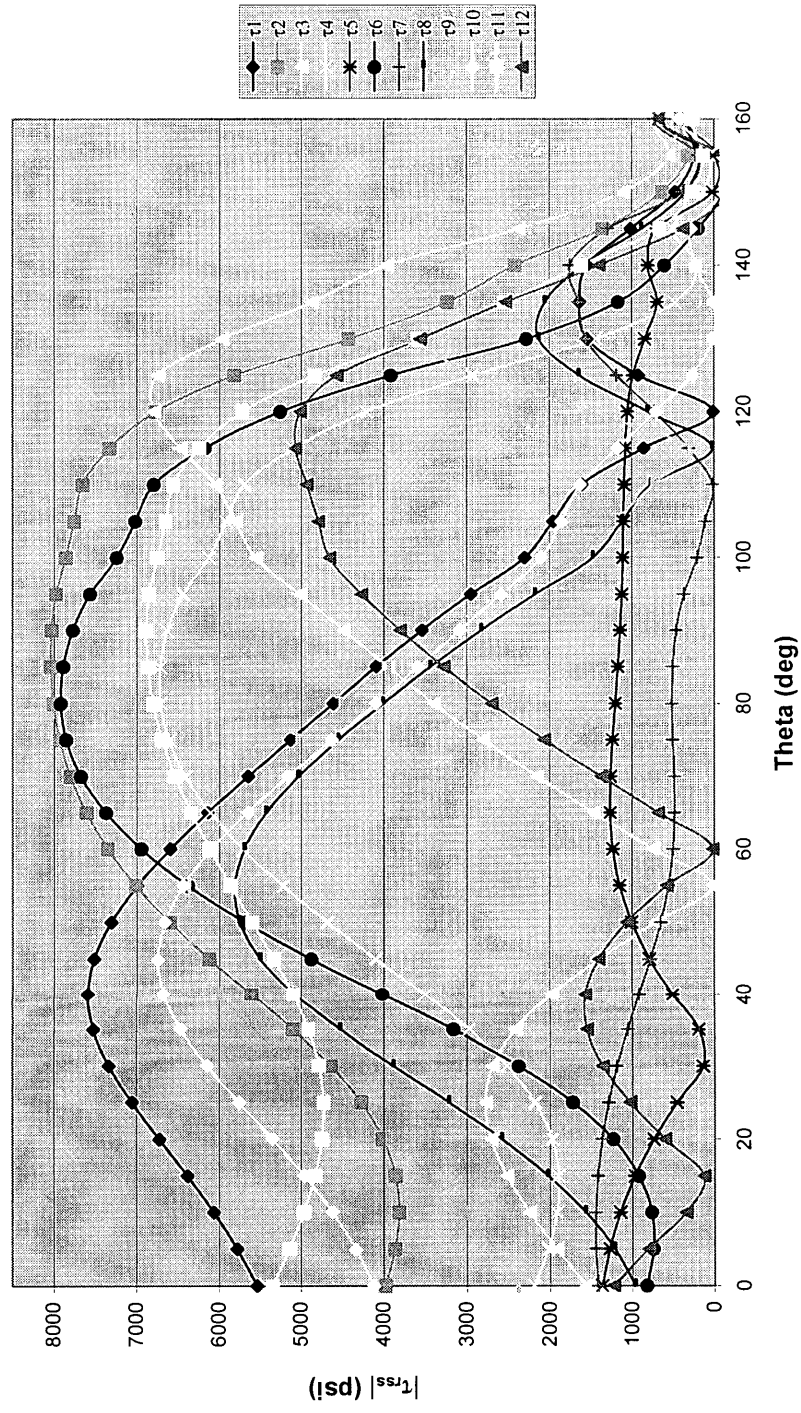






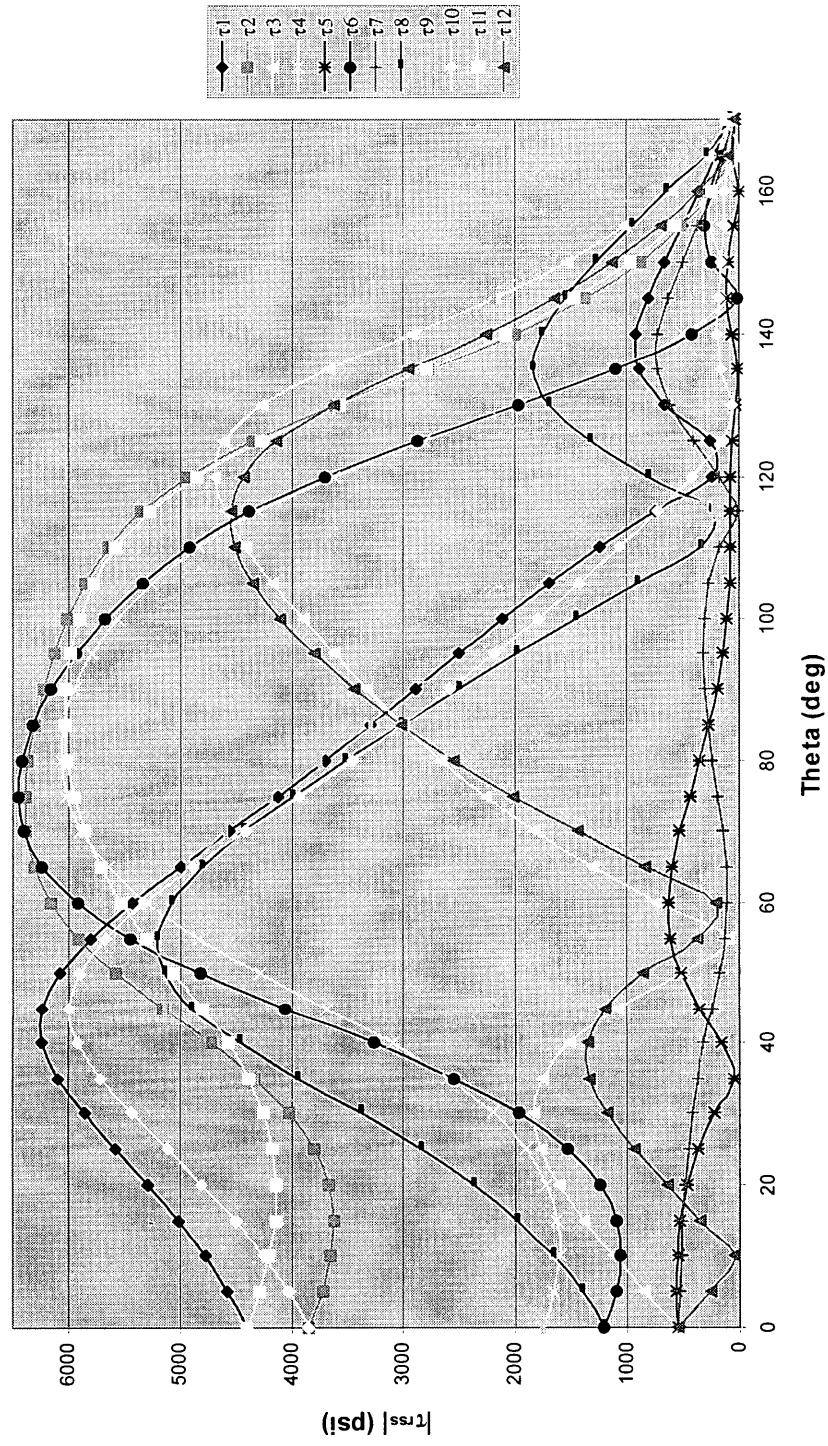
# Resolved Shear Stress v. Theta

Specimen A  
r = 3\*p

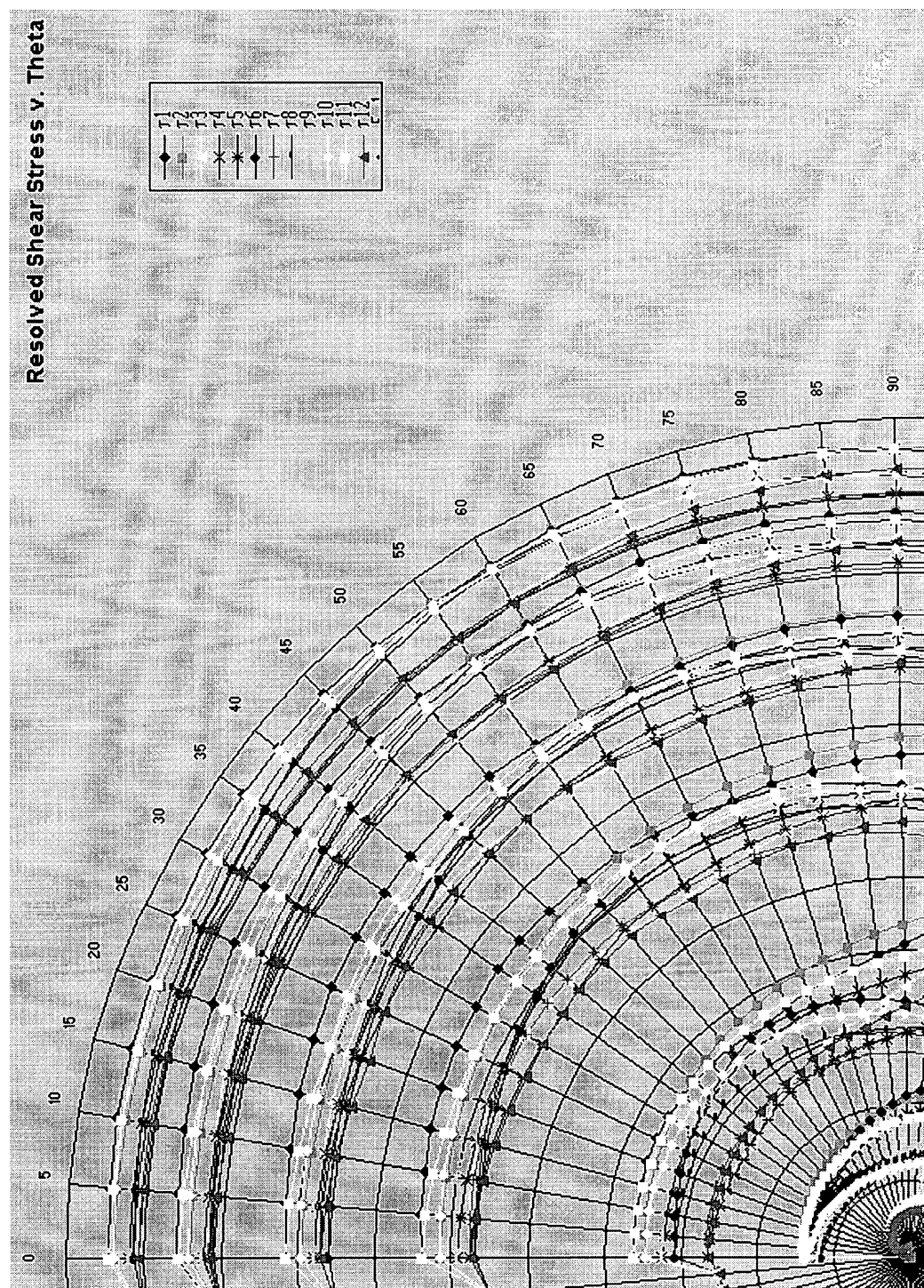


Specimen A  
 $r = 5^*p$

# Resolved Shear Stress v. Theta



Resolved Shear Stress v. Theta





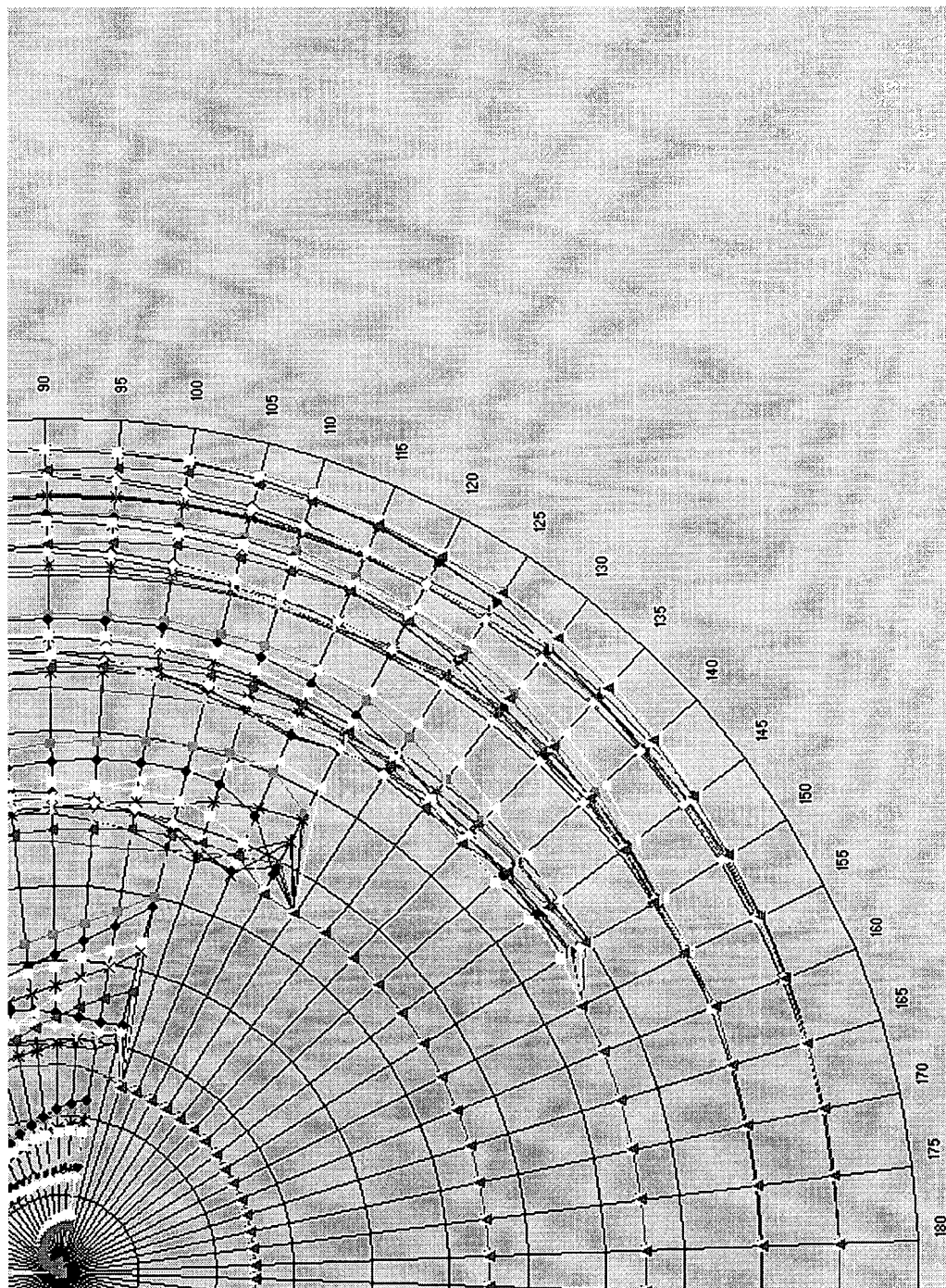




Table 5-1 Specimen A dominant slip system sectors.

Dominant Slip System Sectors Specimen A											
Sector	$r = 0.25^*p$			$r = 0.5^*p$			$r = 1.0^*p$				
	$\theta$	$\tau_{max}$	Slip System	$\theta$	$\tau_{max}$	Slip System	$\theta$	$\tau_{max}$	Slip System		
I	0-17	$\tau_{11}$	(-1-11)[101]	0-35	$\tau_1$	(111)[10-1]	0-57	$\tau_1$	(111)[10-1]		
II	17-82	$\tau_2$	(111)[0-11]	35-105	$\tau_2$	(111)[0-11]	57-113	$\tau_2$	(111)[0-11]		
III	82-100	$\tau_6$	(-11-1)[011]				113-120	$\tau_3$	(111)[1-10]		
IV											
V											
VI											
Sector	$r = 2.0^*p$			$r = 3.0^*p$			$r = 5.0^*p$				
	$\theta$	$\tau_{max}$	Slip System	$\theta$	$\tau_{max}$	Slip System	$\theta$	$\tau_{max}$	Slip System		
I	0-59	$\tau_1$	(111)[10-1]	0-55	$\tau_1$	(111)[10-1]	0-54	$\tau_1$	(111)[10-1]		
II	59-116	$\tau_2$	(111)[0-11]	55-120	$\tau_2$	(111)[0-11]	54-68	$\tau_2$	(111)[0-11]		
III	116-150	$\tau_3$	(111)[1-10]	120-148	$\tau_3$	(111)[1-10]	68-86	$\tau_6$	(-11-1)[011]		
IV				148-156	$\tau_9$	(-11-1)[011]	86-122	$\tau_2$	(111)[0-11]		
V							122-145	$\tau_3$	(111)[1-10]		
VI							145-165	$\tau_9$	(-11-1)[011]		

### Specimen B

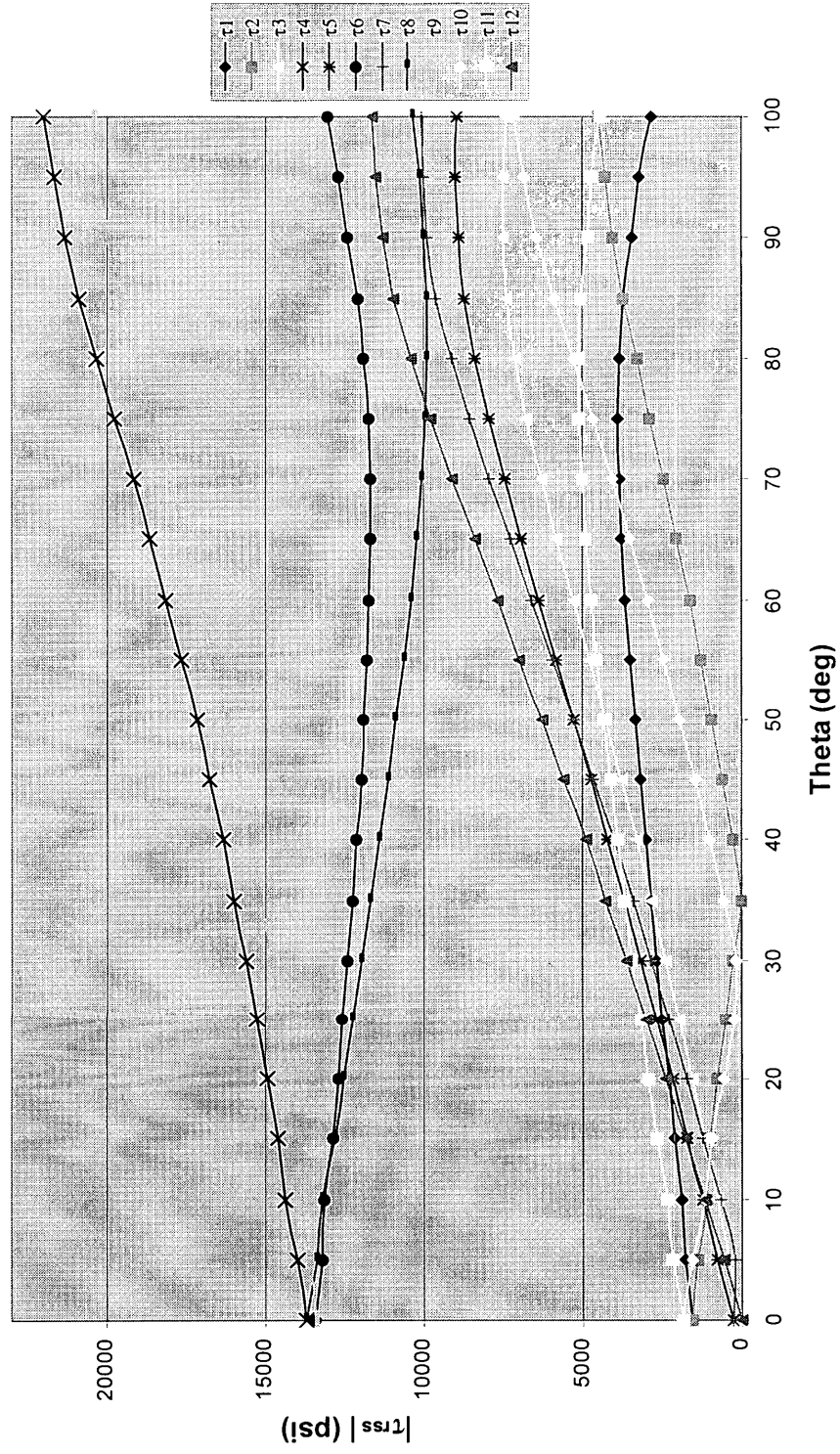
Specimen B was tested with a  $[-110]$  load, a  $[110]$  growth direction, and a  $[001]$  notch plane (Figure 4-1). The maximum RSS at any location is  $\tau_4=25,720\text{psi}$  at  $r=0.5*\rho$  and  $105^\circ$ , or  $3.66*\sigma_{\text{applied}}$ . Note, this stress is moderately higher than the maximum for Specimen A and is in a different slip system, however it does occur at the same location. Results are again presented for the 12 primary RSS values from  $0.25*\rho$  to  $5*\rho$  and from  $0^\circ$  to the top of the notch. Like Specimen A, the slip system with the maximum RSS varies with radial and angular position. The dominant slip system sectors at each radius show a larger number of sectors than Specimen A, especially for higher angles (Table 5-2). Again, the dominant system is not constant over the range of radii.

Like Specimen A, the resolved shear stresses change values and shift positions relative to each other with respect to theta. Combining and scaling the 12 primary stresses for the entire range of radii gives the entire RSS field (Figure 5-14). Although the number of activated slip systems is higher for Specimen B, the angular range that maintains a single dominant slip system for all radii is significant with  $\tau_4$  ranging from  $63^\circ$ - $100^\circ$ . Overall the RSS field is dominated by  $\tau_4$ ,  $\tau_6$ ,  $\tau_7$ , and  $\tau_8$  on the  $\{-11-1\}$  planes. The field also shows  $\tau_9$  and  $\tau_{12}$  briefly, again on the  $\{-11-1\}$  planes, as well as  $\tau_1$  and  $\tau_3$ , which emerge at high angles on the  $(111)$  plane.



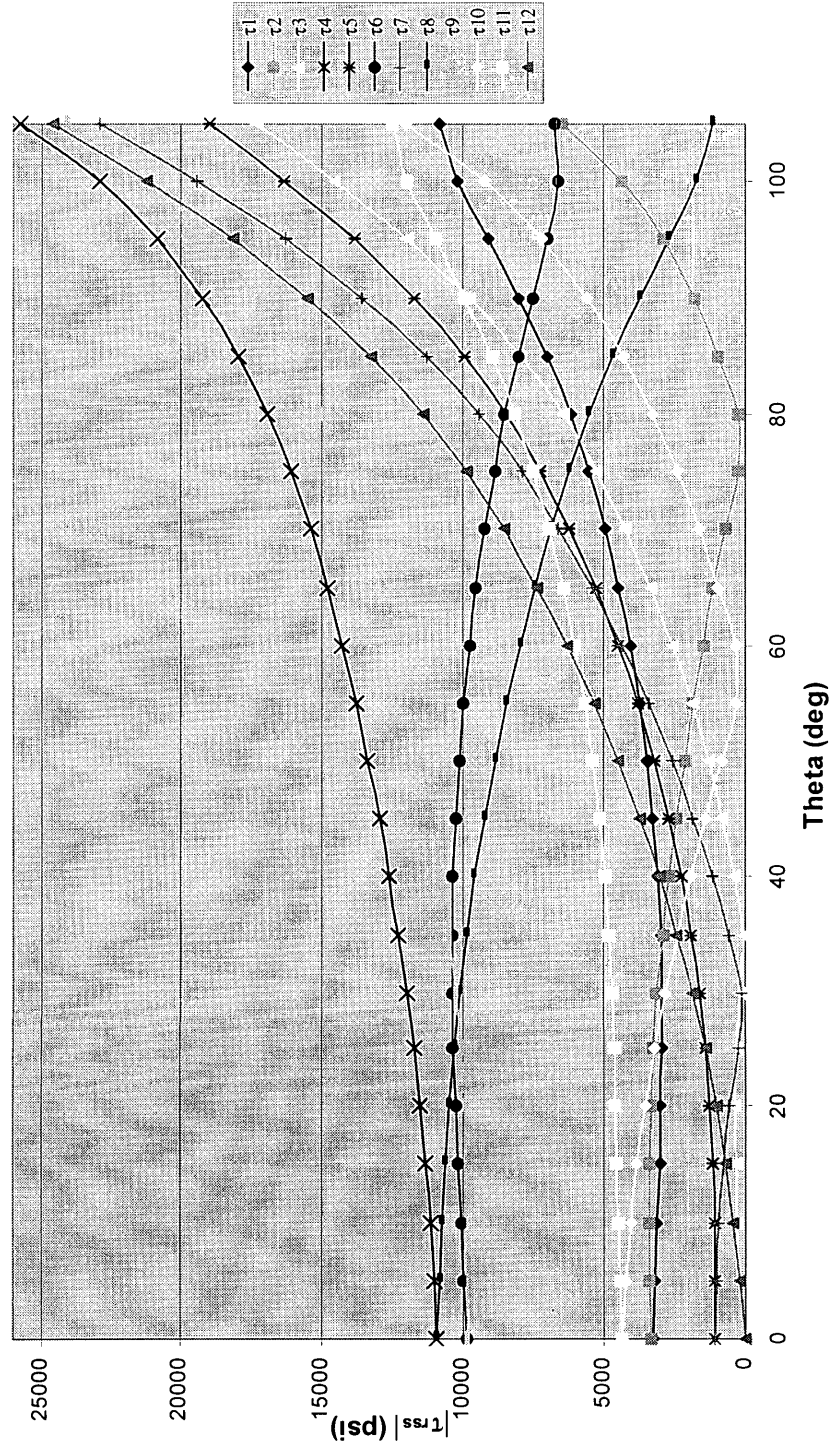
Specimen B  
 $r = 0.25^*p$

### Resolved Shear Stress v. Theta

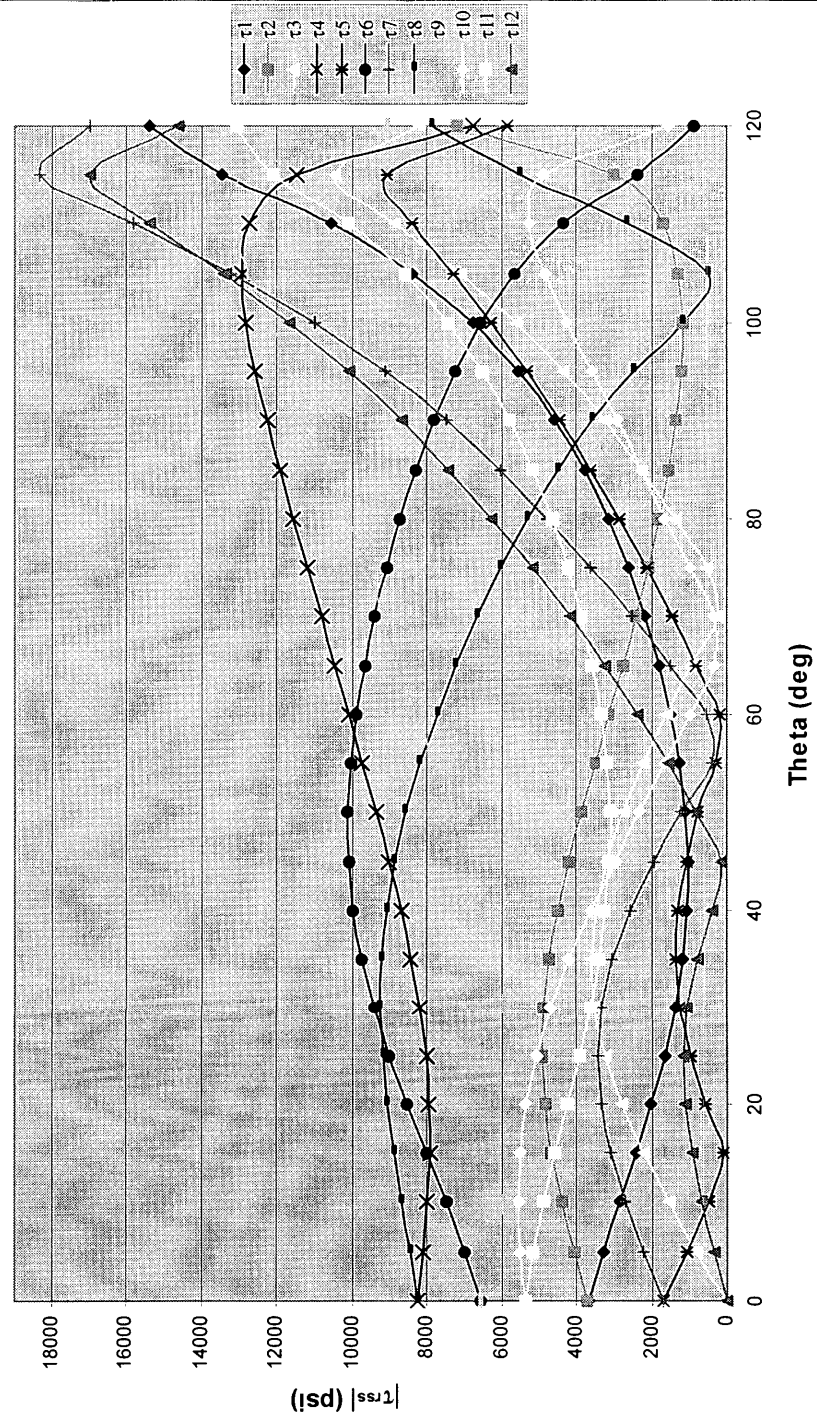


Specimen B  
 $r = 0.5^* \rho$

### Resolved Shear Stress v. Theta

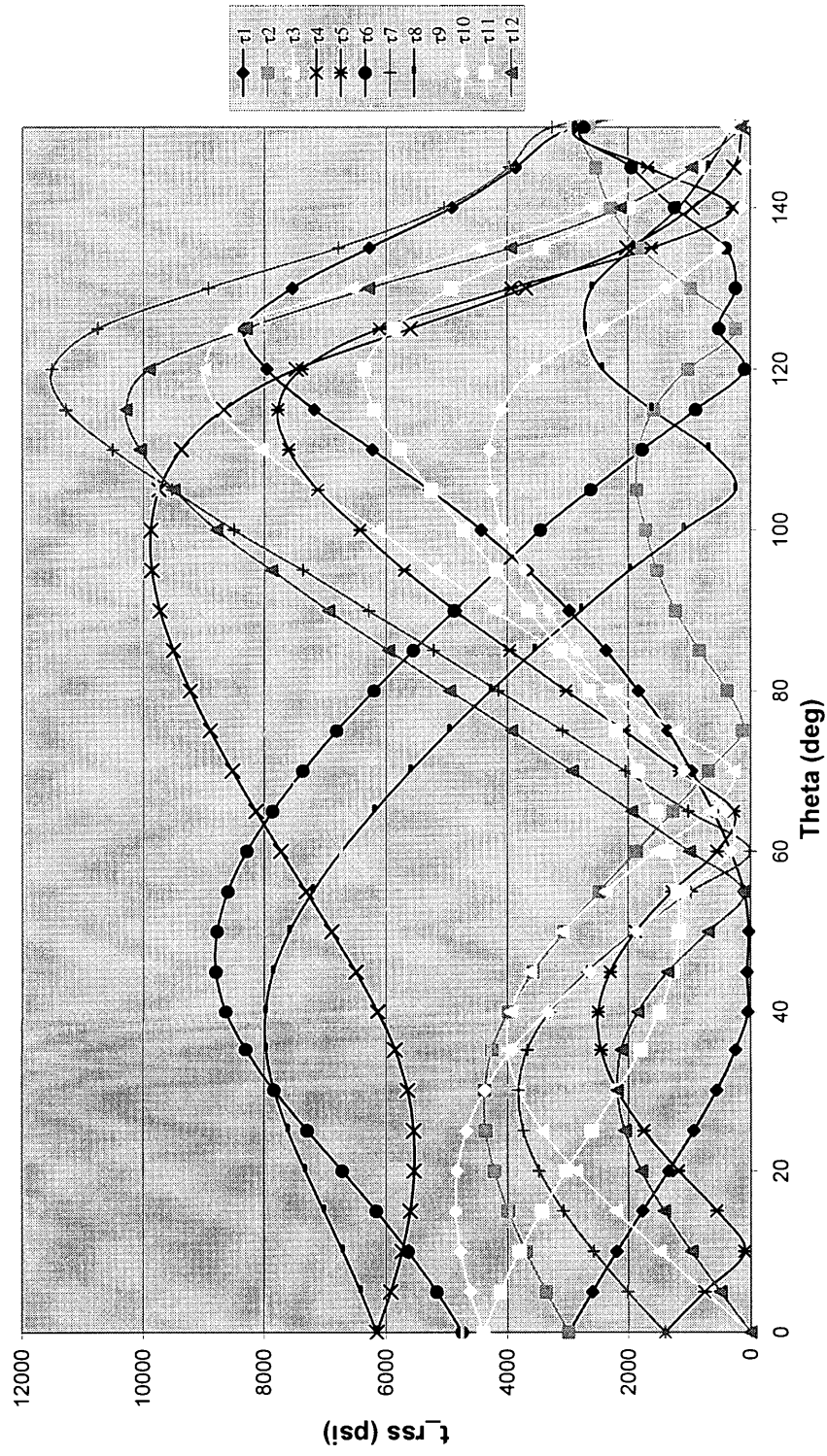


### Resolved Shear Stress v. Theta



Specimen B  
 $r = 2.0 \cdot p$

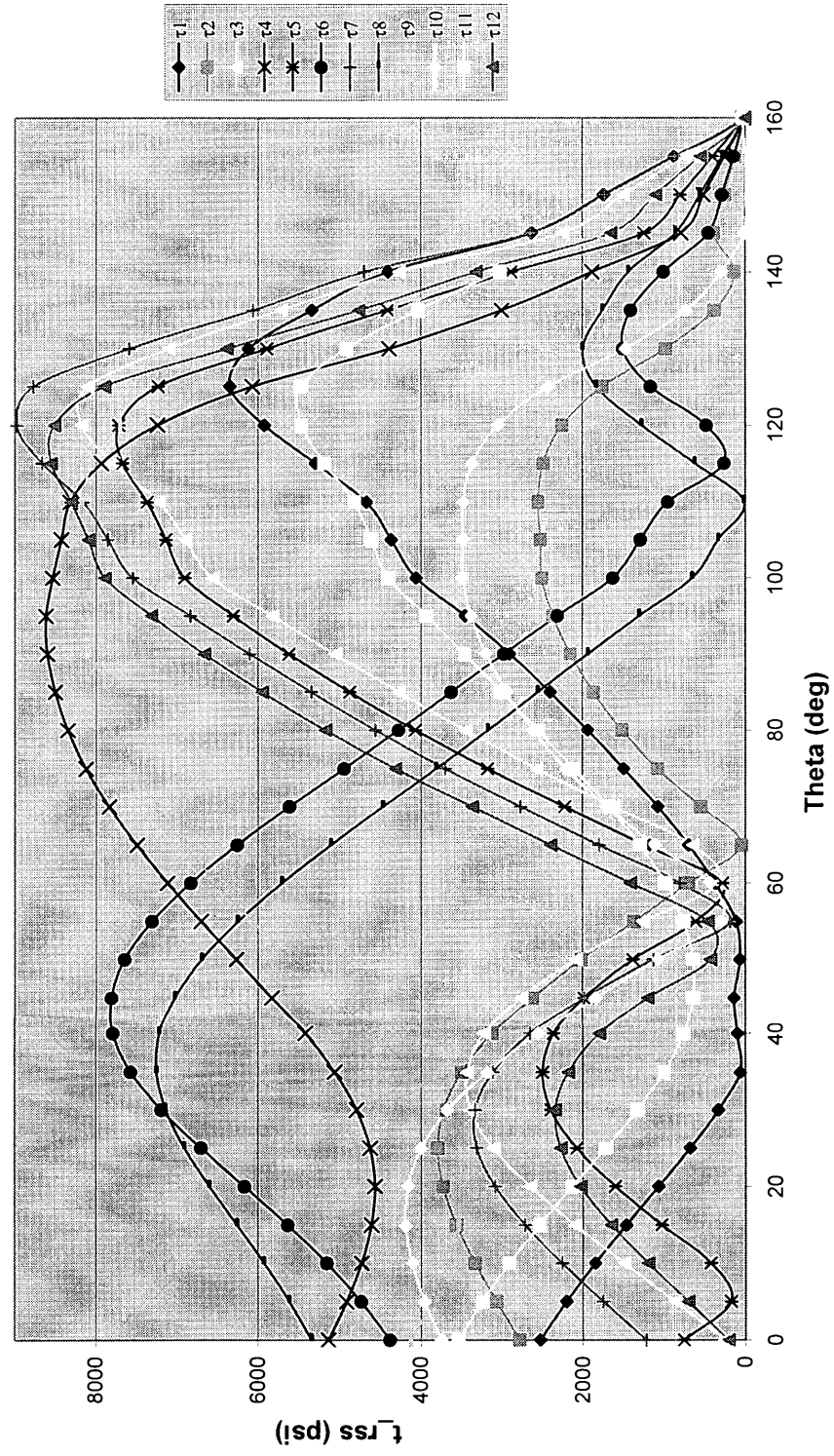
### Resolved Shear Stress v. Theta





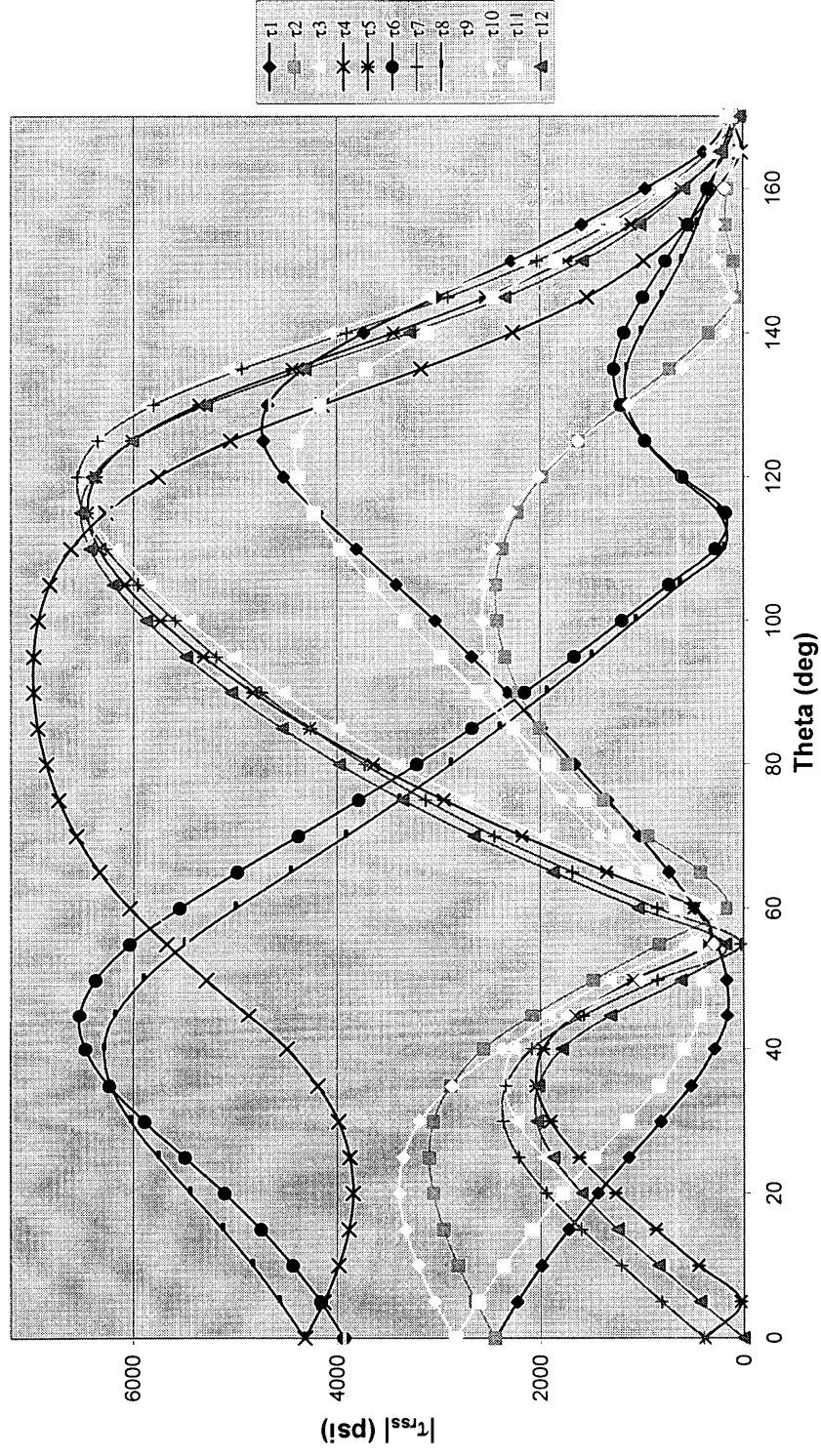
Specimen B  
 $r = 3.0 \cdot p$

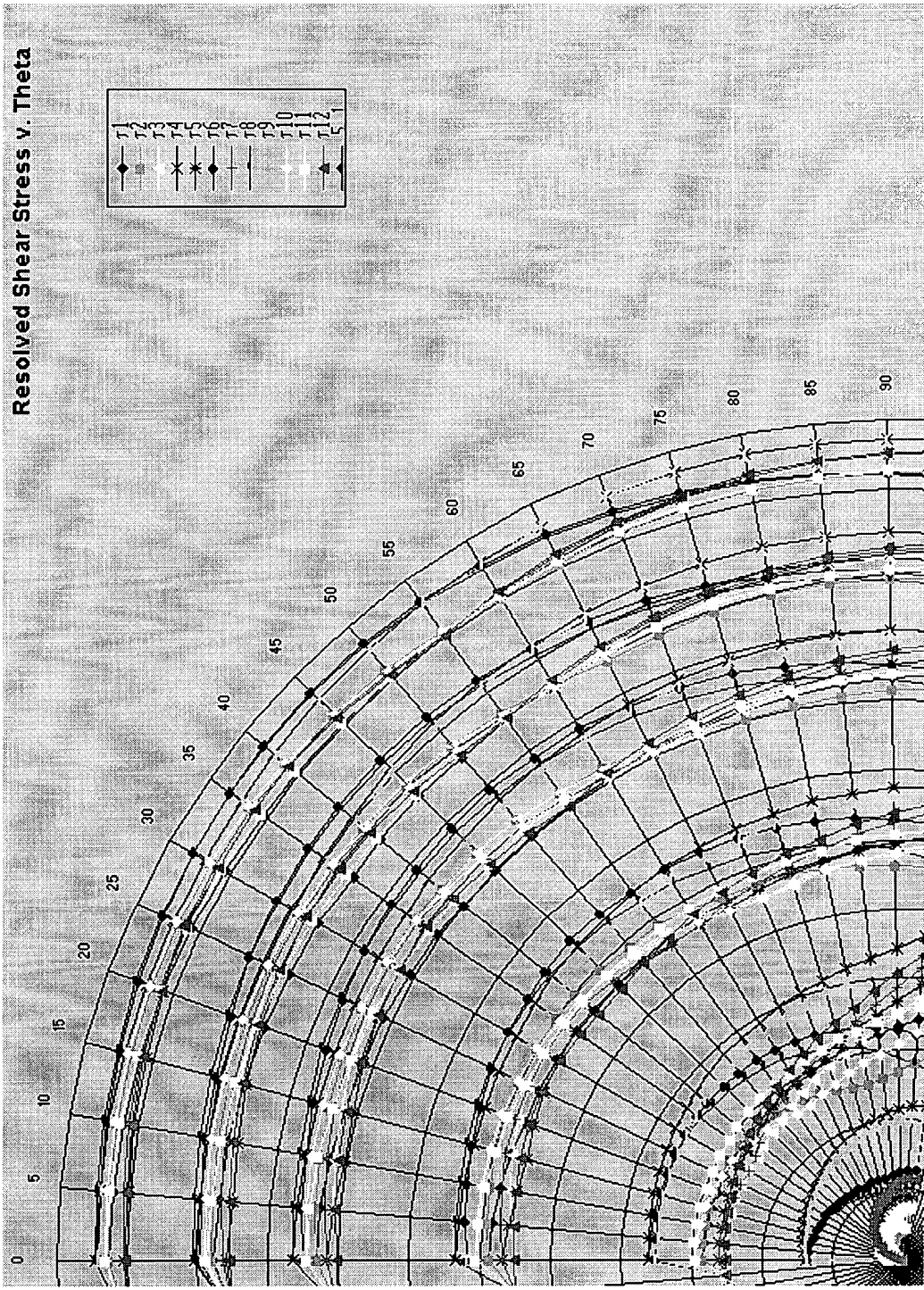
# Resolved Shear Stress v. Theta



Specimen B  
 $r = 5^*p$

Resolved Shear Stress v. Theta







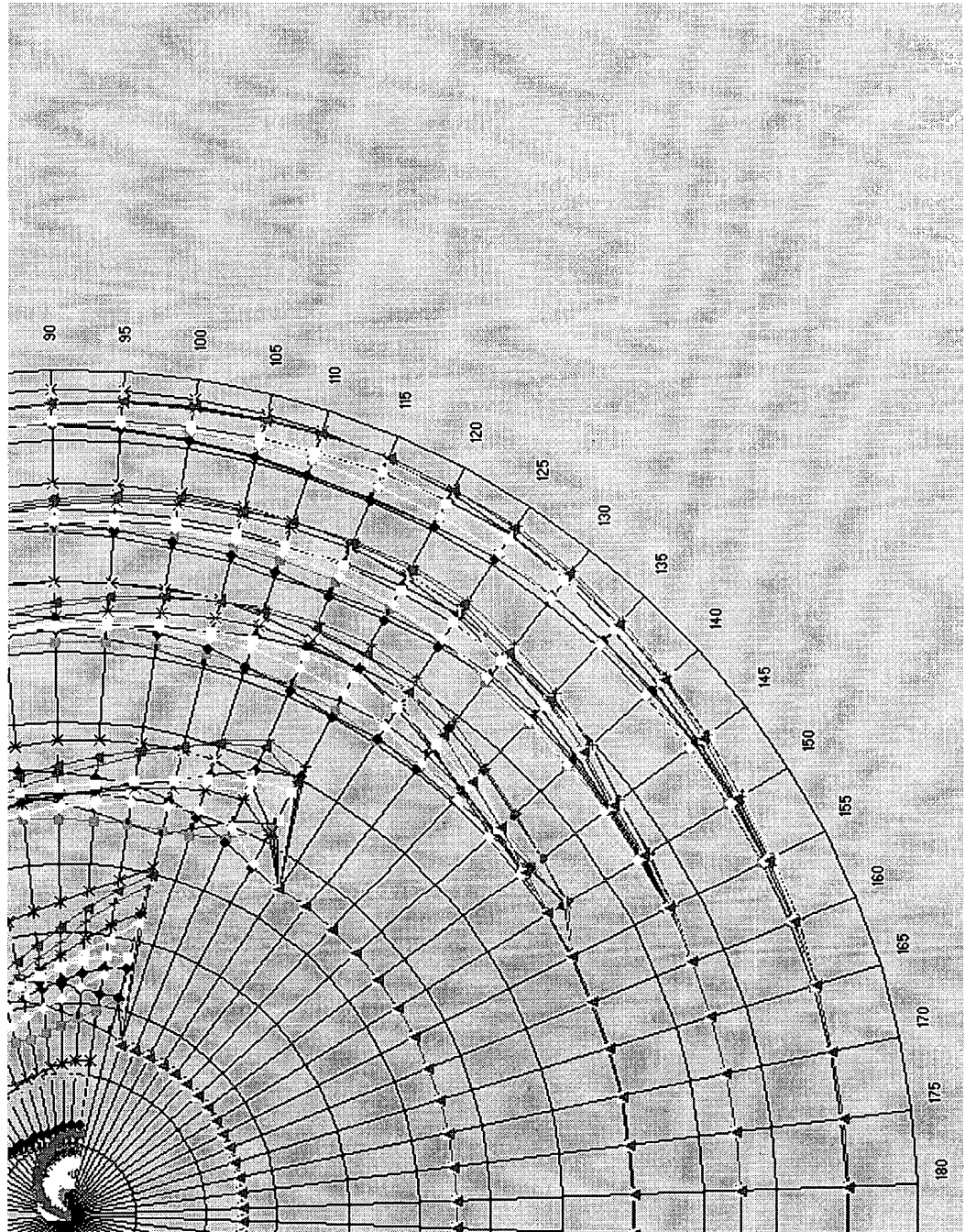




Table 5-2 Specimen B dominant slip system sectors.

Dominant Slip System Sectors Specimen B									
Sector	$r = 0.25^*p$			$r = 0.5^*p$			$r = 1.0^*p$		
	$\theta$	$\tau_{\max}$	Slip System	$\theta$	$\tau_{\max}$	Slip System	$\theta$	$\tau_{\max}$	Slip System
I	0-100	$\tau_4$	(-11-1)[10-1]	0-105	$\tau_4$	(-11-1)[10-1]	0-27	$\tau_8$	(1-1-1)[0-11]
II							27-58	$\tau_6$	(-11-1)[011]
III							58-104	$\tau_4$	(-11-1)[10-1]
IV							104-107	$\tau_{12}$	(-1-11)[1-10]
V							107-120	$\tau_7$	(1-1-1)[110]
VI									
VII									
Sector	$r = 2.0^*p$			$r = 3.0^*p$			$r = 5.0^*p$		
	$\theta$	$\tau_{\max}$	Slip System	$\theta$	$\tau_{\max}$	Slip System	$\theta$	$\tau_{\max}$	Slip System
I	0-30	$\tau_8$	(1-1-1)[0-11]	0-29	$\tau_8$	(1-1-1)[0-11]	0-35	$\tau_8$	(1-1-1)[0-11]
II	30-63	$\tau_6$	(-11-1)[011]	29-58	$\tau_6$	(-11-1)[011]	35-57	$\tau_6$	(-11-1)[011]
III	63-105	$\tau_4$	(-11-1)[10-1]	58-110	$\tau_4$	(-11-1)[10-1]	57-112	$\tau_4$	(-11-1)[10-1]
IV	105-106	$\tau_9$	(1-1-1)[101]	110-113	$\tau_{12}$	(-1-11)[1-10]	112-116	$\tau_{12}$	(-1-11)[1-10]
V	106-150	$\tau_7$	(1-1-1)[110]	113-145	$\tau_7$	(1-1-1)[110]	116-125	$\tau_7$	(1-1-1)[110]
VI				145-160	$\tau_7, \tau_1$	(1-1-1)[110] (111)[10-1]	125-147	$\tau_3$	(111)[1-10]
VII							147-160	$\tau_1$	(111)[10-1]

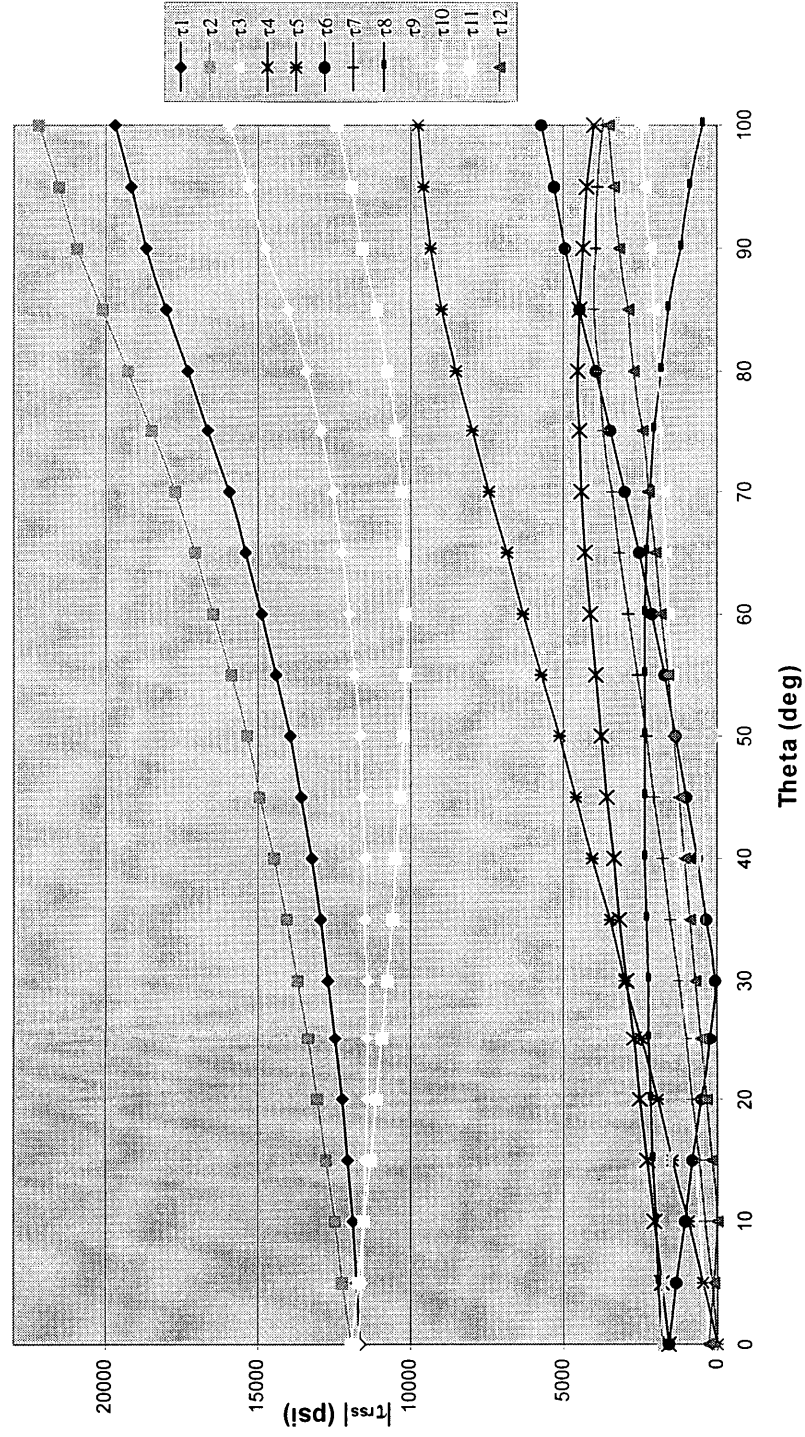
### Specimen C

Specimen C was tested with a  $[110]$  load, a  $[001]$  growth direction, and a  $[-110]$  notch plane (Figure 4-1). The maximum RSS at any location is  $\tau_2=22,200\text{psi}$  at  $r = 0.5*\rho$  and  $105^\circ$ , or  $3.16*\sigma_{\text{applied}}$ . This stress is lower than the maximum for either Specimen A or B, again occurring in a different slip system but at the same location in the RSS field. Results are again presented for the 12 primary RSS values from  $0.25*\rho$  to  $5*\rho$  and from  $0^\circ$  to the top of the notch. Like the two previous specimens, the slip system with the maximum RSS varies with radial and angular position. The dominant slip system sectors for each radius reveal a larger number of sectors than Specimen A at higher angles, but approximately the same as Specimen B (Table 5-3). Again, the dominant system is not constant over the range of radii.

Consistent with Specimens A and B, the resolved shear stresses change values and shift position relative to each other with respect to theta. Combining and scaling the 12 primary stresses for the entire range of radii gives the entire RSS field (Figure 5-21). Like Specimen B, although the number of activated slip systems is higher, the angular range that maintains a single dominant slip system for all radii is considerable with  $\tau_2$  ranging from  $64^\circ$ - $97^\circ$ . Overall, the RSS field is dominated by  $\tau_2$ ,  $\tau_4$ ,  $\tau_5$ ,  $\tau_{10}$ , and  $\tau_{11}$  on both the  $(111)$  and  $\{-11-1\}$  planes. At high angles  $\tau_3$ ,  $\tau_7$ , and  $\tau_8$  briefly appear, again on the  $(111)$  and  $\{-11-1\}$  planes. Specimen C, therefore, shows a dominant system on each of the four possible primary slip planes in the RSS field.

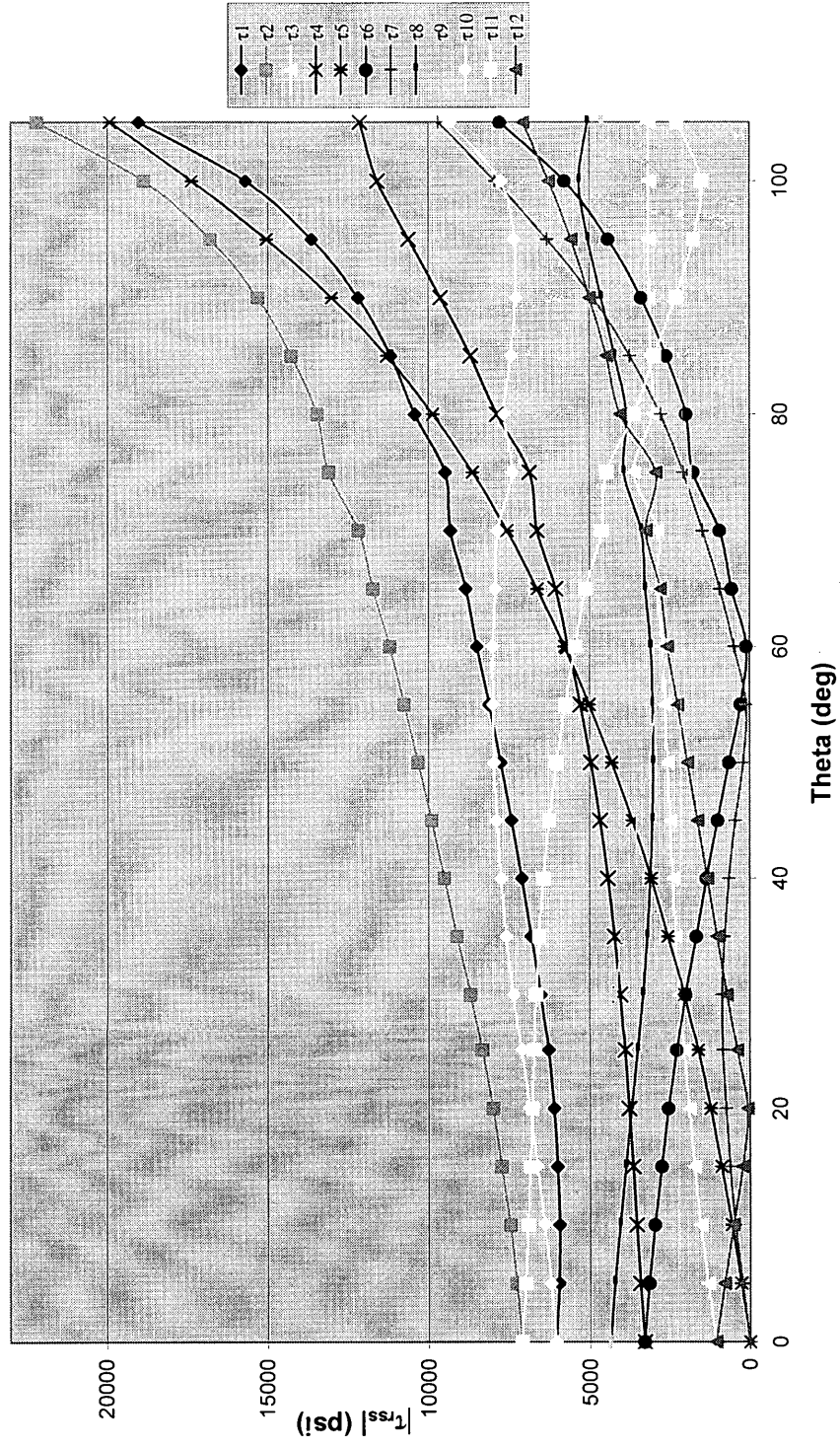
Specimen C  
 $r = 0.25 \cdot p$

### Resolved Shear Stress v. Theta



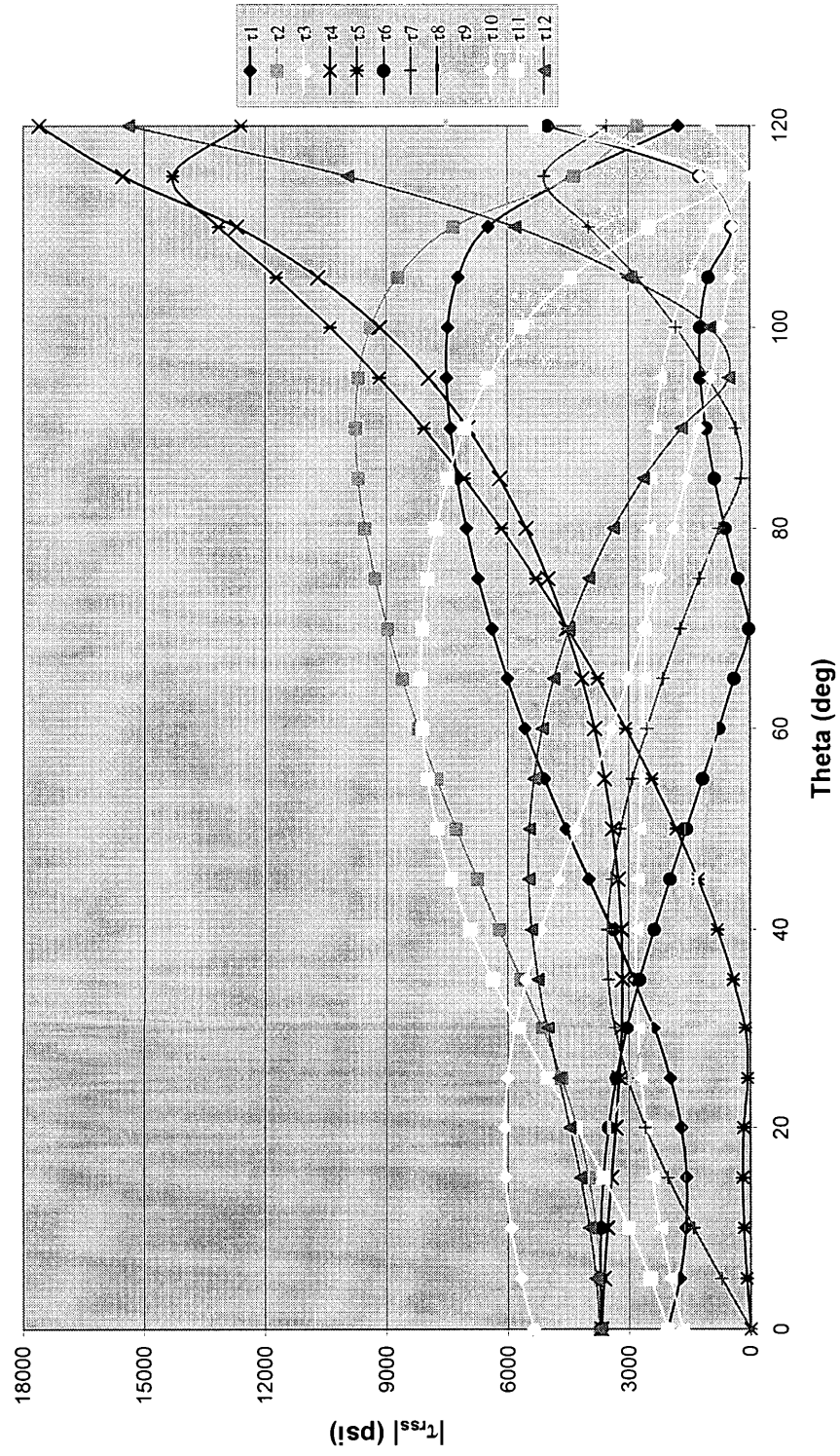
Specimen C  
 $r = 0.5^*p$

### Resolved Shear Stress v. Theta



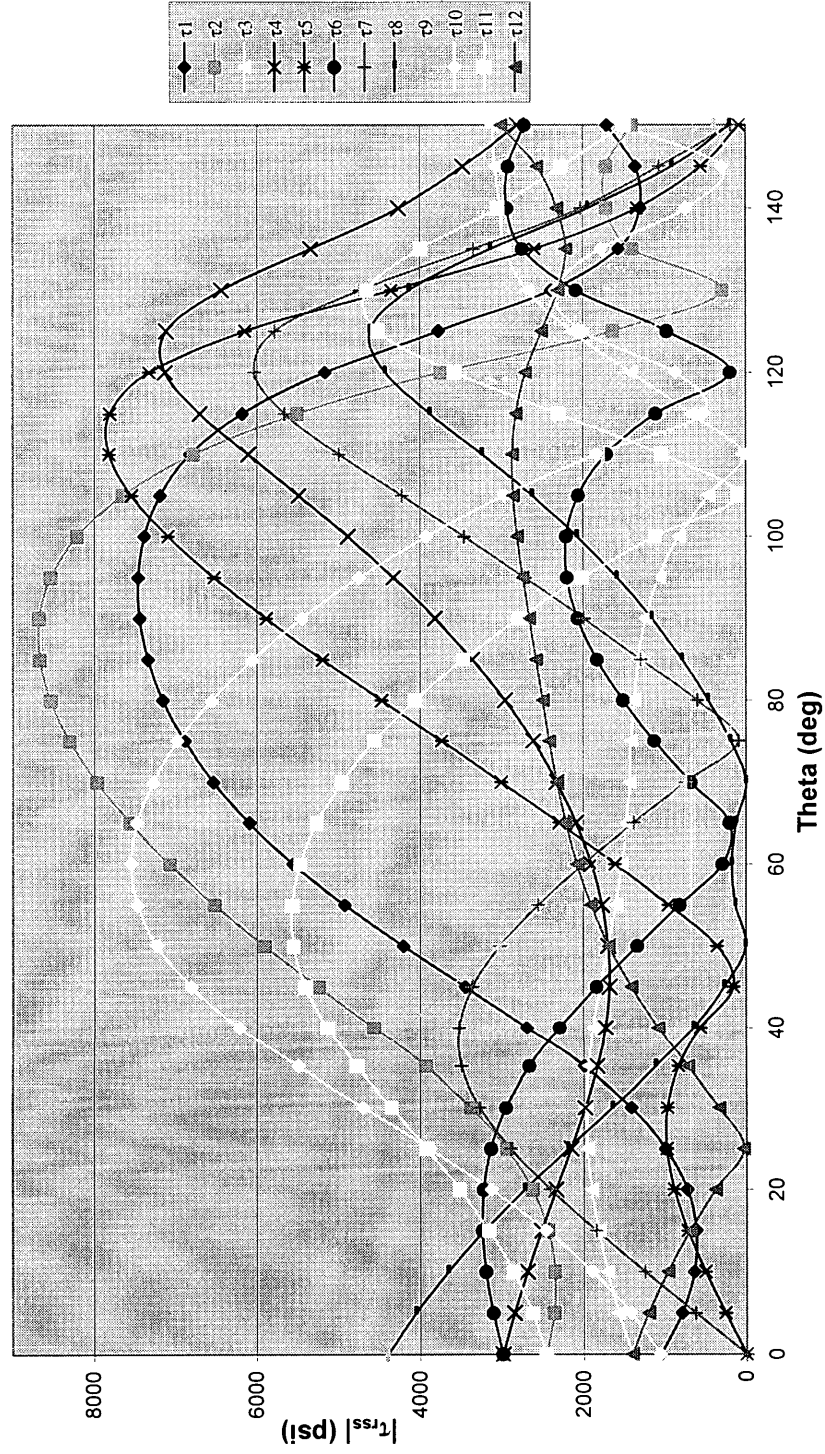
**Specimen C**  
 **$r = 1.0^* \rho$**

### Resolved Shear Stress v. Theta



Specimen C  
 $r = 2.0 \cdot p$

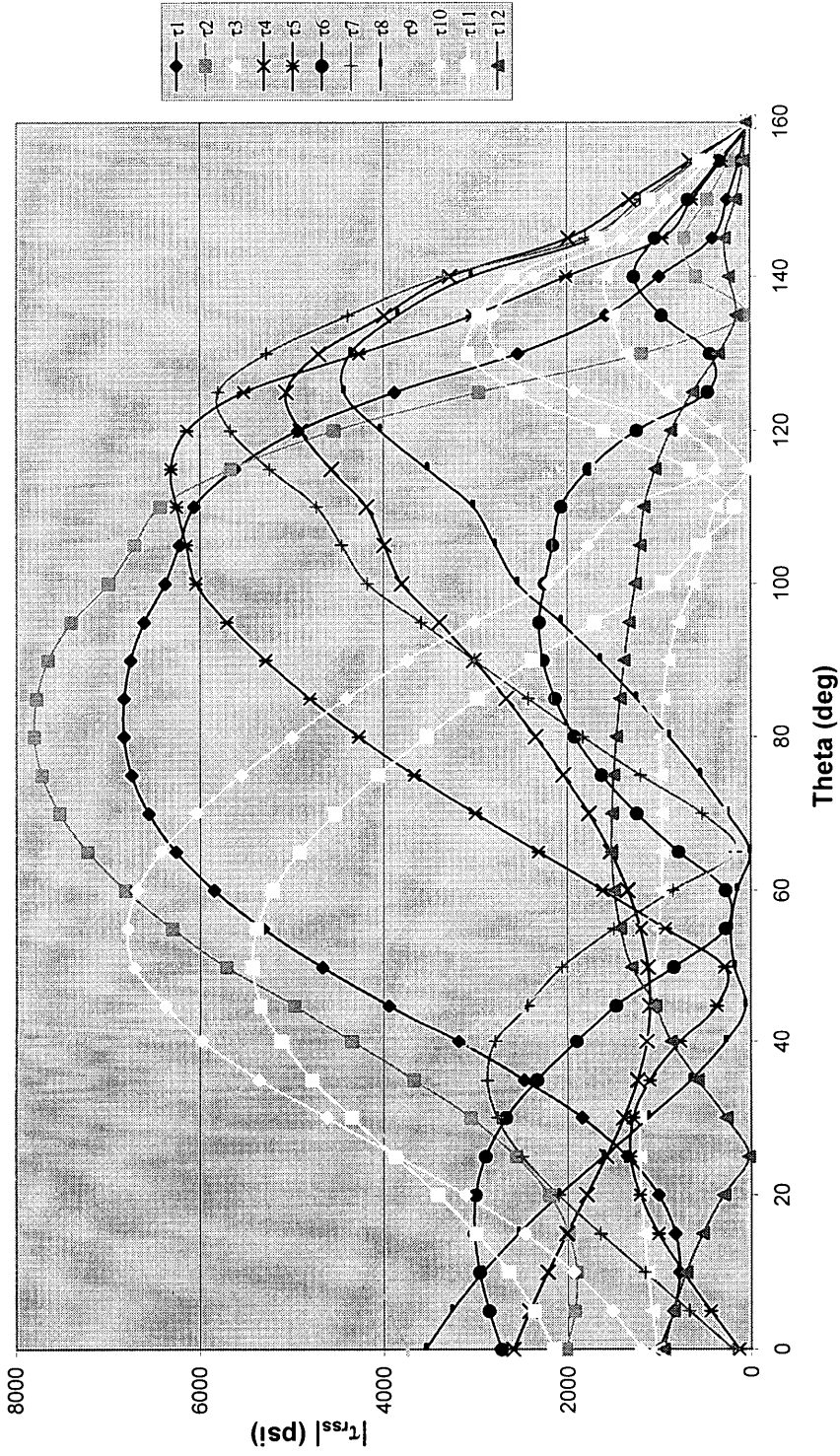
# Resolved Shear Stress v. Theta





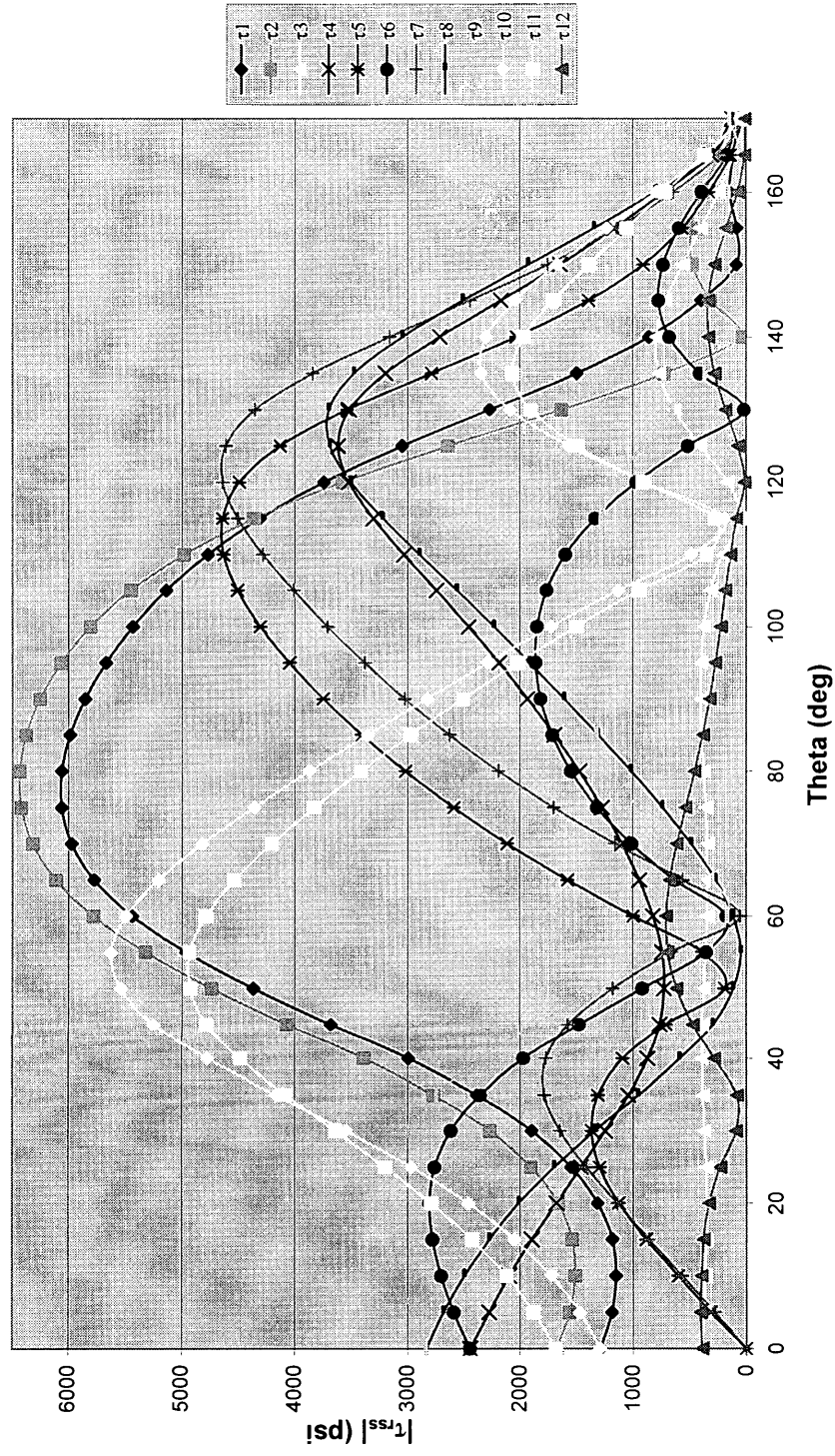
Specimen C  
 $r = 3.0^*p$

# Resolved Shear Stress v. Theta



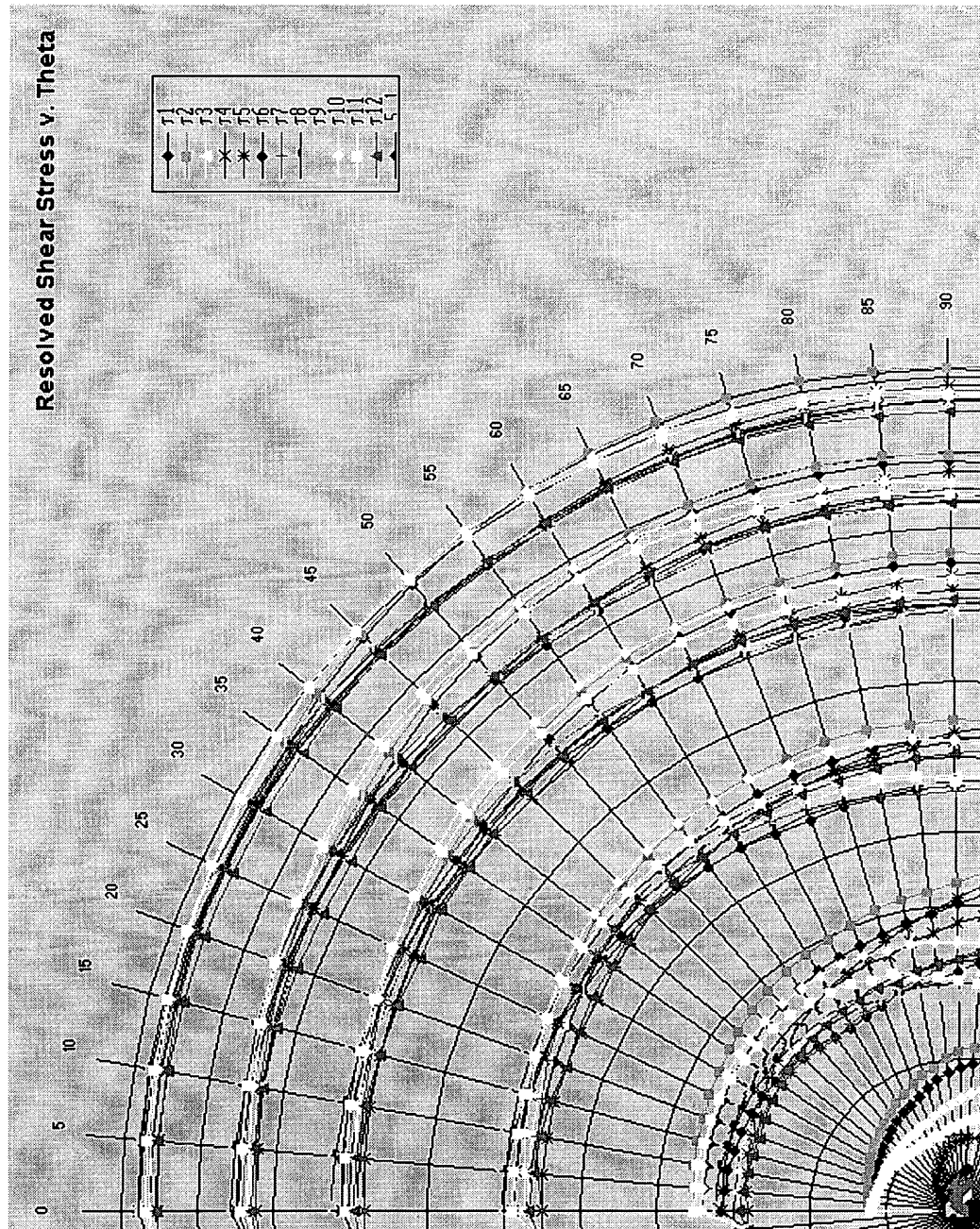
Specimen C  
 $r = 5.0^{\circ}p$

### Resolved Shear Stress v. Theta





# Resolved Shear Stress v. Theta



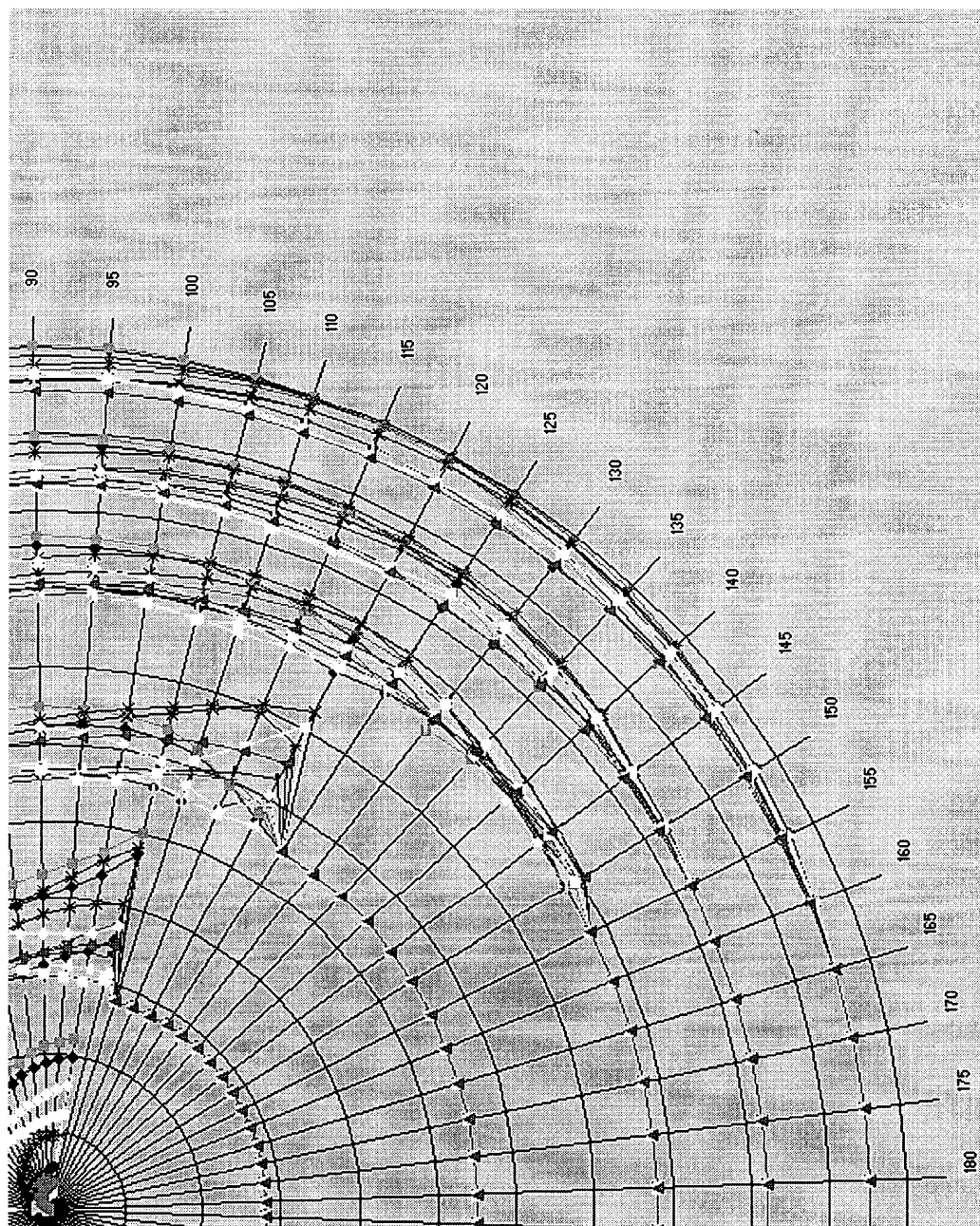


Table 5-3 Specimen C dominant slip system sectors.

Dominant Slip System Sectors Specimen C									
Sector	$r = 0.25^*p$			$r = 0.5^*p$			$r = 1.0^*p$		
	$\theta$	$\tau_{\max}$	Slip System	$\theta$	$\tau_{\max}$	Slip System	$\theta$	$\tau_{\max}$	Slip System
I	0-100	$\tau_2$	(111)[0-11]	0-105	$\tau_2$	(111)[0-11]	0-31	$\tau_{10}$	(-1-11)[011]
II							31-58	$\tau_{11}$	(-1-11)[101]
III							58-97	$\tau_2$	(111)[0-11]
IV							97-112	$\tau_5$	(-11-1)[110]
V							112-120	$\tau_4$	(-11-1)[10-1]
VI									
VII									
VIII									
Sector	$r = 2.0^*p$			$r = 3.0^*p$			$r = 5.0^*p$		
	$\theta$	$\tau_{\max}$	Slip System	$\theta$	$\tau_{\max}$	Slip System	$\theta$	$\tau_{\max}$	Slip System
I	0-31	$\tau_9$	(1-1-1)[101]	0-26	$\tau_9$	(1-1-1)[101]	0-24	$\tau_9$	(1-1-1)[101]
II	31-64	$\tau_{10}$	(-1-11)[011]	26-59	$\tau_{10}$	(-1-11)[011]	24-33	$\tau_{11}$	(-1-11)[101]
III	64-106	$\tau_2$	(111)[0-11]	59-111	$\tau_2$	(111)[0-11]	33-58	$\tau_{10}$	(-1-11)[011]
IV	106-121	$\tau_5$	(-11-1)[110]	111-123	$\tau_5$	(-11-1)[110]	58-113	$\tau_2$	(111)[0-11]
V	121-147	$\tau_4$	(-11-1)[10-1]	123-141	$\tau_7$	(1-1-1)[110]	113-118	$\tau_5$	(-11-1)[110]
VI	147-150	$\tau_3$	(111)[1-10]	141-150	$\tau_4$	(-11-1)[10-1]	118-147	$\tau_7$	(1-1-1)[110]
VII							147-160	$\tau_8$	(1-1-1)[0-11]
VIII							160-170	$\tau_{10}$	(-1-11)[011]
								$\tau_{11}$	(-1-11)[101]
								$\tau_{11}$	(-1-11)[10-1]
								$\tau_8$	(1-1-1)[0-11]

### Specimen/Orientation Comparison

For each of the three specimens, the [001] orientation occupies a different axis of the notch geometry: for Specimen A [001] is the load axis, for Specimen B it is the notch plane axis, and for Specimen C it is the growth axis. Comparing these three orientations is advantageous, because although [001] is the most common growth direction (and presumably load direction) a complex part like a turbine blade may have stress concentrations close to one of the specimen notch orientations.

The radius with the maximum RSS,  $r = 0.5 \cdot \rho$ , is a good location to begin to compare data. For all three orientations the number of dominant slip systems is very small at this radius: two for Specimen A and one for Specimens B and C. As noted above, Specimen B has the highest RSS overall, and it is also the only specimen with the maximum RSS not on the (111) plane. Of greater interest though, in terms of application, is that Specimen C has the lowest RSS. Not only does Specimen C have the overall lowest maximum RSS, but its second highest stress is significantly lower than the other two orientations as well. The “second maximum” for  $r = 0.5 \cdot \rho$  again occurs at  $105^\circ$  for all three orientations: For Specimen A  $\tau_6 = 23,800$  psi ( $3.39 \cdot \sigma_{\text{applied}}$ ), for Specimen B  $\tau_{12} = 24,570$  psi ( $3.50 \cdot \sigma_{\text{applied}}$ ), and for Specimen C  $\tau_5 = 19,930$  psi ( $2.84 \cdot \sigma_{\text{applied}}$ ).

Recall, Specimen C is the only specimen to eventually activate all four primary slip planes, though at its maximum it is still limited to only the (111) plane. From a mechanics perspective, it is unclear whether the slip plane itself has an effect on the desirability (or lack thereof) of one orientation over another. In fact, certain attributes (such as the second, third, and fourth maximum RSS values) may actually be a more desirable criteria as they determine whether mechanisms such as cross-slip will occur. These mechanisms, though they may result in more deformation, can also avoid fracture

by releasing energy through ductile deformation. Therefore, any propositions regarding the best orientation will be avoided here and left to those with a greater knowledge of dislocation and other atomic mechanisms to determine the most favorable design orientation. Nonetheless, from a merely stress-based approach Specimen C is the clear candidate to design for a larger load tolerance of the notched specimen.

### Experimental Results

As noted in the introduction, these experiments had a dual purpose of analyzing the orientations tested, and also providing a numerical analysis to compare experimental results to, specifically those obtained by the MSE department. As of the writing of this paper, the MSE department had tested Specimen A in a paper published by Forero and Ebrahimi (TMS Annual Meeting, 2002); those results will be compared here. Forero and Ebrahimi applied a 1100 lb tensile load to the specimen (exact geometry given in Chapter 2) whose orientation is the same as Specimen A. Although the specimen orientation is symmetric about the notch, some results vary between positive and negative theta (probably due to irregularities in the notch cutout); therefore all values are presented here. The 5\* $\rho$  radius will be used to minimize the effects of plasticity at the notch tip and correlate better with the elastic model. After scaling the numerical curves for the actual applied load, we can draw in the yield stress ( $\tau_{\text{yield}} \sim 47$  ksi) to see which slip systems are predicted to be activated (Figure 5-22). The FEA results predict slip activation from 0° to 135°, however, in the experimental test activation is only visible at the given radius up to 110°. Also, whereas several systems are predicted to be active in many locations, the experimental specimen generally shows a single dominant system in each sector (Figure 5-23). Recall, the exact slip system cannot be determined by the slip trace analysis alone

(Figure 5-24); nonetheless, correlating the known slip plane to the numerical prediction is still a good measure of the model's accuracy. The single dominant slip systems predicted for each sector by the FEA and those indicated by the experimental specimen do not match (Table 5-4); however, the visible systems are among those predicted to be activated by the applied stress level.

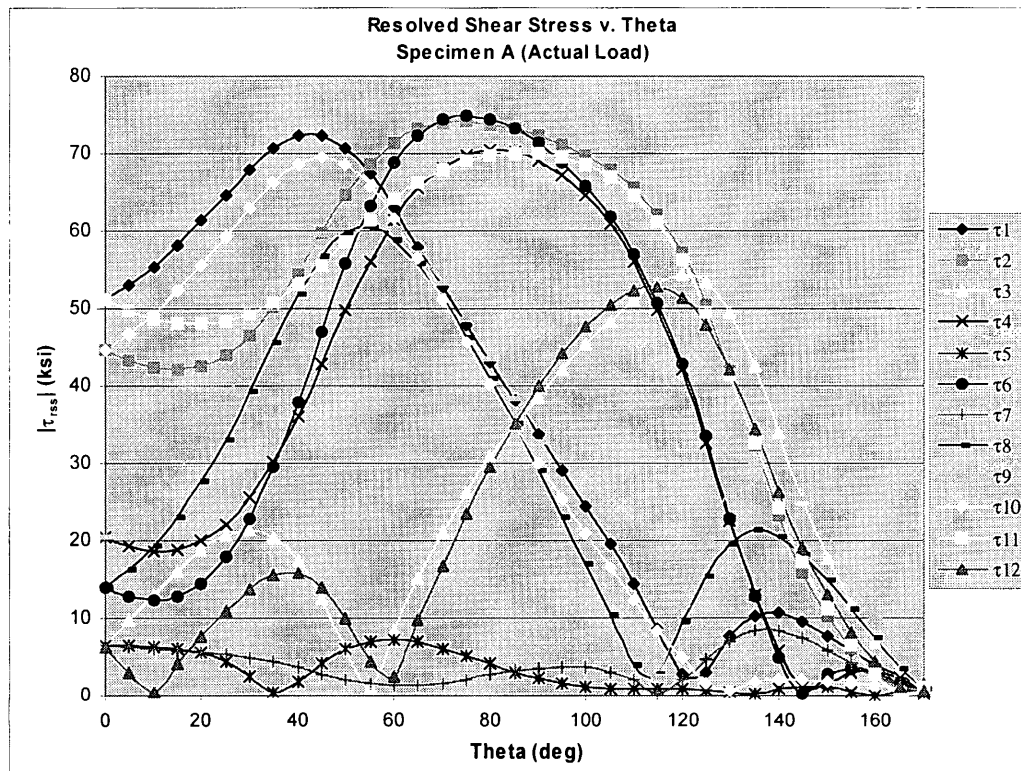


Figure 5-22 Experimental load for Specimen A. The dashed line indicates the yield stress of the material; any RSS curves above this line represent slip systems that should be activated.

Table 5-4 Specimen A experimental results.

Dominant Slip System Sectors					
Specimen A $r = 5.0^{\circ}\rho$					
	Numerical Solution			Experimental Results	
Sector	$\theta$	$\tau_{\max}$	Slip System	$\theta$	Slip Plane
I	0-54	$\tau_1$	(111)[10-1]	0-75 -(0-65)	(111) or (11-1) (111) or (11-1)
II	54-68	$\tau_2$	(111)[0-11]	75-90 -(65-100)	(-111) (1-11)
III	68-86	$\tau_6$	(-11-1)[011]	90-110 -(100-115)	(111) or (11-1) (111) or (11-1)
IV	86-122	$\tau_2$	(111)[0-11]		
V	122-145	$\tau_3$	(111)[1-10]		
VI	145-165	$\tau_9$	(1-1-1)[101]		

Note: The given plane will refer to either the “positive” or “negative” plane: i.e. (111) is analogous to (-1-1-1).

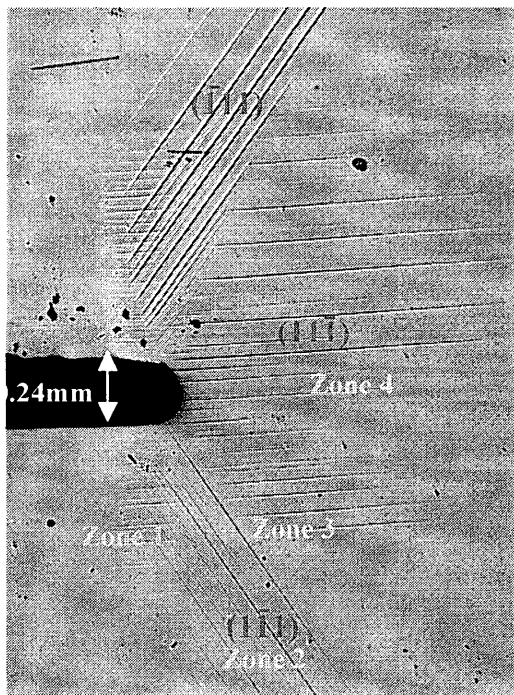


Figure 5-23 Experimental tensile test specimen Material A.  
Source: Forero and Ebrahimi, 2002.

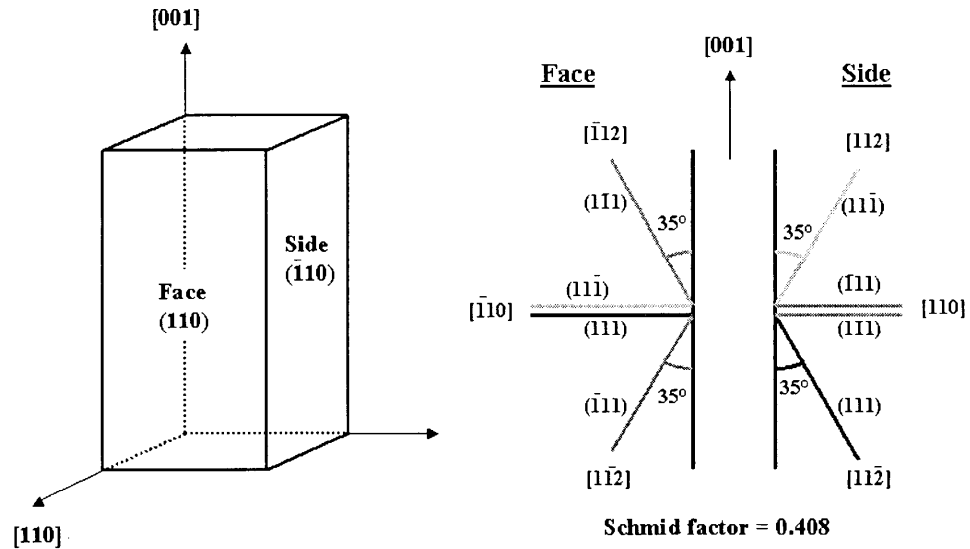


Figure 5-24 Tensile test specimen and surface slip lines.  
Source: Courtesy, Dr. Fereshteh Ebrahimi, UF.

### Application

As shown in the previous section, a set of charts giving the RSS as a function of both  $\theta$  and  $\rho$  about a notch tip can be used to predict the active slip systems and sectors for a given load and yield stress. Because the resolved shear stresses are linear, the charts can be modified for any desired load level by simply multiplying the original applied load (100 lb = 7028 psi) by some constant to reach the new load level. The sectors can be determined by drawing in the yield stress level and obtaining those angles where the resolved shear stresses intersect that yield level. Any resolved shear stresses above the “yield line” should be activated and the intersections determine the sectors.



### Example

A tensile test is conducted on a specimen with geometry and orientation identical to Specimen A. A 2 kip load is applied to the specimen, whose material is known to have a yield stress near 50 ksi. The original load, 100lb, is multiplied by 20 to reach the new load; an identical cross-section allows a similar multiplication of the originally applied 7028 psi to 140.6 ksi. The original chart can then be scaled by the same factor, giving a range from 0 to 450 ksi. The yield line is drawn in at 50 ksi (Figure 5-25); all individual RSS lines above the yield should be activated at the corresponding intersecting angles. This example shows eight separate slip systems being activated for the entire range of angles at the given radius (Figure 5-25). Two additional slip systems are initiated at 40° and 42°, giving essentially two sectors with different possible activations: 0°-40° and 40°-

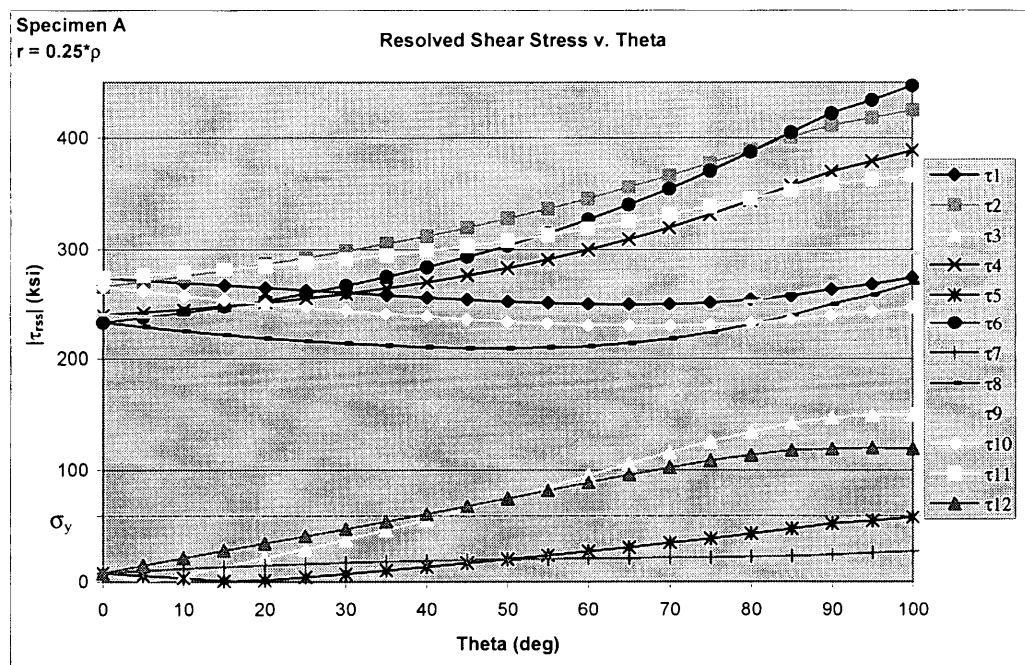


Figure 5-25 Numerical plot adjusted for example load; yield stress indicated.

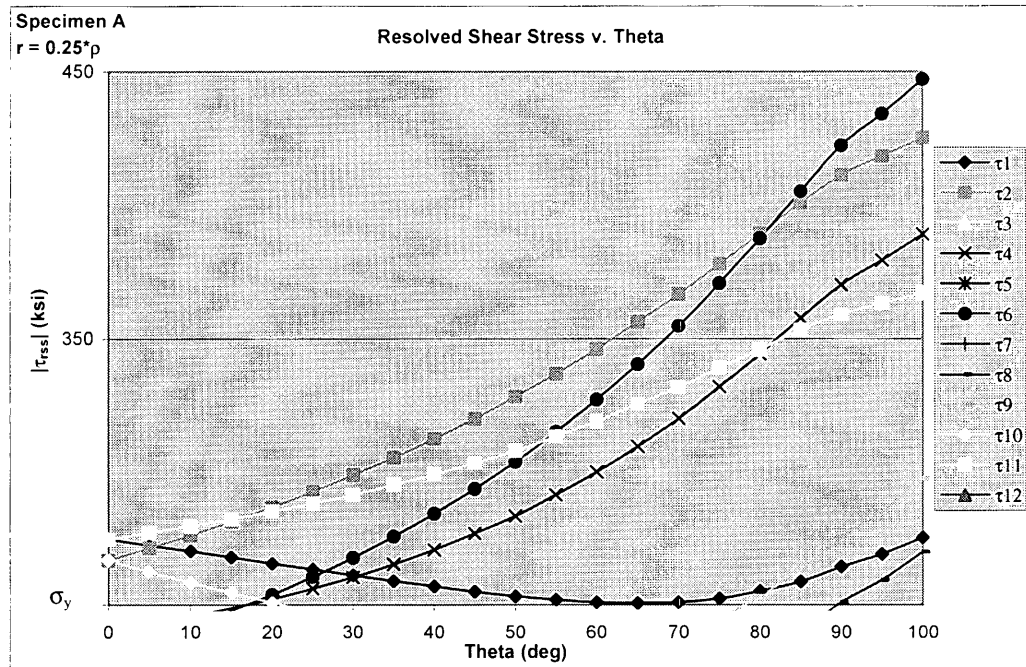


Figure 5-26 Numerical plot adjusted for example load; maximum RSS changes with theta.

100°. However, the maximum RSS varies along the radial line, and the dominant slip systems shifts from  $\tau_{11}$  (-1-11) to  $\tau_2$  (111) to  $\tau_6$  (-11-1), giving three sectors where the dominant system shifts: 0°-17°, 17°-82°, and 82°-100°. Although the total number of activated systems and their sector angles is subject to the specific applied load, the systems with the highest RSS should always be the ones that undergo visible deformation first. Beginning at high angles,  $\tau_6$  should initiate first, followed by  $\tau_2$  surrounding most of the notch, and finally  $\tau_{11}$  should initiate directly ahead of the notch.

#### General Material Slip Activation

Material A is a good experimental material to compare a simplified model to because it does not experience a large amount of strain hardening. Strain hardening, the result of cross-slip, and other deformation behaviors can inhibit analysis because the

evidence of the original dislocation motion may no longer be evident. This case is well illustrated with another superalloy, “Material B,” which undergoes a large amount of cross-slip; cross-slip dominates the surface and makes it difficult to determine the original slip activation. The model’s elastic simplification also better predicts slip activation for low strain hardened materials because these materials do not undergo a large stage of plastic deformation before they fail. Therefore, the current model should correlate well with other materials with similar behavior.

If the model is developed into an elastic-plastic model, then it should predict slip activation even more accurately in materials like Material A, and may even be applied to strain-hardened materials. However, since strain hardening is a result of dislocation mechanisms, whose scope exceeds the standard mechanics regime, it is unknown whether a model that does incorporate plasticity would accurately predict slip activation and sectors.

## CHAPTER 6

### CONCLUSIONS

1. A three-dimensional linear elastic finite element model that includes the effect of material anisotropy provides a good indication of active slip planes and sectors at the surface of a notched tensile test specimen.
2. Slip sectors determined by the stress field are not constant for a given material, as generally indicated by the literature, but are determined by the specific applied load and yield stress of the material.
3. Under tensile loading, a specimen with a  $[110]$  notch plane (primary) orientation and a  $[001]$  notch growth direction will have lower resolved shear stresses than one with  $[001]/[-110]$  or  $[-110]/[110]$  notch plane/notch growth directions, respectively.

## CHAPTER 7 RECOMMENDATIONS FOR FUTURE WORK

The elastic model presented here appears to predict slip accurately, and can be used to predict fatigue behavior based on equations that incorporate individual RSS values, such as fatigue life (Swanson and Arakere, 2000). The RSS values, even though based on an elastic model, are valid here because the fatigue life is determined from the stresses in the elastic regime. However, fracture mechanisms are also of great interest in this area of study, in which case a plastic model should be developed that can accurately incorporate the elastic regime predicted here, as well as plastic behavior near the notch tip. Upon entering the plastic regime, however, future work should be aware of the many added factors that come into play, including strain hardening, crystal lattice rotation, creep, etc..

The orientations presented here have been studied by others, with varying degrees of success, yet few have conducted tests deviating from the  $\langle 100 \rangle$  or  $\langle 110 \rangle$  orientations; although, there is some degree of work done for the  $\langle 111 \rangle$  orientation. Since the elastic model's simplicity makes it efficient, future research should entail testing for other orientations with a similar model, with the ultimate goal eventually being an accurate elastic-plastic model. Also, due to the variation in past research where sectors are determined by stress *or* strain fields, a study should be done to compare the stress *and* strain fields and the resulting sectors for the same load and model to confirm their correlation.

# APPENDIX A EXAMPLE COORDINATE TRANSFORMATION AND ACCURACY CHECKS

## Example Coordinate Transformation

$$\begin{array}{lcl} x' & \cos(\psi_1) & 0 \quad -\sin(\psi_1) \quad x \\ y' & 0 & 1 \quad 0 \quad y \\ z' & \sin(\psi_1) & 0 \quad \cos(\psi_1) \quad z \end{array} \quad \begin{array}{lcl} x'' & 1 & 0 \quad 0 \quad x' \\ y'' & 0 & \cos(-\psi_2) \quad -\sin(-\psi_2) \quad y' \\ z'' & 0 & \sin(-\psi_2) \quad \cos(-\psi_2) \quad z' \end{array}$$

$$\begin{array}{lcl} x'' & \alpha_1 & \beta_1 \quad \gamma_1 \quad x \\ y'' & \alpha_2 & \beta_2 \quad \gamma_2 \quad y \\ z'' & \alpha_3 & \beta_3 \quad \gamma_3 \quad z \end{array}$$

$$\begin{array}{lcl} \alpha_1 & \beta_1 & \gamma_1 \quad 1 \quad 0 \quad 0 \quad \cos(\psi_1) \quad 0 \quad -\sin(\psi_1) \\ \alpha_2 & \beta_2 & \gamma_2 \quad = \quad 0 \quad \cos(-\psi_2) \quad -\sin(-\psi_2) \quad 0 \quad 1 \quad 0 \\ \alpha_3 & \beta_3 & \gamma_3 \quad 0 \quad \sin(-\psi_2) \quad \cos(-\psi_2) \quad \sin(\psi_1) \quad 0 \quad \cos(\psi_1) \end{array}$$

$$\begin{array}{lcl} \alpha_1 & \beta_1 & \gamma_1 \quad \cos(\psi_1) \quad 0 \quad -\sin(\psi_1) \\ \alpha_2 & \beta_2 & \gamma_2 \quad = \quad \sin(\psi_2) \cdot \sin(\psi_1) \quad \cos(\psi_2) \quad \sin(\psi_2) \cdot \cos(\psi_1) \\ \alpha_3 & \beta_3 & \gamma_3 \quad \cos(\psi_2) \cdot \sin(\psi_1) \quad -\sin(\psi_2) \quad \cos(\psi_2) \cdot \cos(\psi_1) \end{array}$$

$$\psi_1 = \text{atan} \frac{2}{3} \quad \psi_1 = 33.69$$

$$\psi_2 = \text{atan} \frac{1}{\sqrt{13}} \quad \psi_2 = 15.50$$

$$\begin{array}{lcl}
\alpha_1 & \beta_1 & \gamma_1 \\
\alpha_2 & \beta_2 & \gamma_2 \\
\alpha_3 & \beta_3 & \gamma_3
\end{array}
:=
\begin{array}{lcl}
\cos(\psi_1) & 0 & -\sin(\psi_1) \\
\sin(\psi_2) \cdot \sin(\psi_1) & \cos(\psi_2) & \sin(\psi_2) \cdot \cos(\psi_1) \\
\cos(\psi_2) \cdot \sin(\psi_1) & -\sin(\psi_2) & \cos(\psi_2) \cdot \cos(\psi_1)
\end{array}$$

$$\begin{array}{lcl}
\alpha_1 & \beta_1 & \gamma_1 \\
\alpha_2 & \beta_2 & \gamma_2 \\
\alpha_3 & \beta_3 & \gamma_3
\end{array}
=
\begin{array}{lcl}
0.832 & 0 & -0.555 \\
0.148 & 0.964 & 0.222 \\
0.535 & -0.267 & 0.802
\end{array}$$

### Checks for Accuracy

All should equal zero:

$$\begin{array}{lll}
\alpha_1 \cdot \alpha_2 + \beta_1 \cdot \beta_2 + \gamma_1 \cdot \gamma_2 = 0 & \alpha_1 \cdot \alpha_3 + \beta_1 \cdot \beta_3 + \gamma_1 \cdot \gamma_3 = 0 & \alpha_3 \cdot \alpha_2 + \beta_3 \cdot \beta_2 + \gamma_3 \cdot \gamma_2 = 0 \\
\alpha_1 \cdot \beta_1 + \alpha_2 \cdot \beta_2 + \alpha_3 \cdot \beta_3 = 0 & \alpha_1 \cdot \gamma_1 + \alpha_2 \cdot \gamma_2 + \alpha_3 \cdot \gamma_3 = 0 & \beta_1 \cdot \gamma_1 + \beta_2 \cdot \gamma_2 + \beta_3 \cdot \gamma_3 = 0
\end{array}$$

All should equal one:

$$\begin{array}{lll}
\alpha_1^2 + \beta_1^2 + \gamma_1^2 = 1 & \alpha_2^2 + \beta_2^2 + \gamma_2^2 = 1 & \alpha_3^2 + \beta_3^2 + \gamma_3^2 = 1 \\
\alpha_1^2 + \alpha_2^2 + \alpha_3^2 = 1 & \beta_1^2 + \beta_2^2 + \beta_3^2 = 1 & \gamma_1^2 + \gamma_2^2 + \gamma_3^2 = 1
\end{array}$$

All checks affirm a proper transformation.

## REFERENCES

- Alden, D., "An Analysis of the Yield Phenomena in René N4+ Single Crystals with respect to Orientation and Temperature," Ph.D. dissertation, University of Cincinnati, 1990.
- Anderson, T., *Fracture Mechanics: Fundamentals and Applications*, 2<sup>nd</sup> Ed., CRC Press, Inc.; 1995, p.54.
- ANSYS Elements Reference, ANSYS Release 5.6; ANSYS, Inc. November 1999.
- Bickford, W., *Advanced Mechanics of Materials*, Addison-Wesley, 1998, pp.10, 280-1.
- Crone, W. and Shield, T., "Experimental Study of the Deformation near a Notch Tip in Copper and Copper-Beryllium Single Crystals," *Journal of the Mechanics and Physics of Solids*, **49**, 2001, pp.2819-2838.
- Cuitino, A. and Ortiz, M., "Three-Dimensional Crack Tip Fields in Four-Point Bending Copper Single-Crystal Specimens," *Journal of the Mechanics and Physics of Solids*, **44** (6), 1996, pp. 863-904.
- Davis, J.R., ed., *Heat Resistant Materials*, ASM Specialty Handbook, ASM International, 1997, pp.256-263.
- Deiter, G., *Advanced Mechanical Metallurgy*, 3<sup>rd</sup> Ed., McGraw-Hill, 1986, pp.106, 114.
- Deluca, D., Pratt and Whitney Aircraft, Inc., Personal Correspondence, 2001.
- Deluca, D. and Annis, C., "Fatigue in Single Crystal Nickel Superalloys," Office of Naval Research, Department of the Navy FR23800, August 1995.
- Ebrahimi, F. and Forero, L., Symposium on Fatigue of High Temperature Materials, TMS annual Meeting, Seattle, Feb 17-22, 2002.
- Lall, C.; Chin, S., and Pope, D., "The Orientation and Temperature Dependence of the Yield Stress of Ni<sub>3</sub>(Al, Nb) Single Crystals," *Metallurgical Transactions*, 10A, 1979, pp.1323-1332.
- Lekhnitskii, S.G., *Theory of Elasticity of an Anisotropic Elastic Body*, Holden-Day, Inc., 1963, pp. 1-40.



Miner, R.; Voigt, R.; Gayda, J. and Gabb, T., "Orientation and Temperature Dependence of Some Mechanical Properties of the Nickel Base Single Crystal Alloy René N4, Part 1: Tensile Behavior," *Metallurgical Transactions A*, **17A** (3), 1986, p.491.

Mohan, R.; Ortiz, M., and Shih, C., "An Analysis of Cracks in Ductile Single Crystals—II. Mode I loading," *Journal of the Mechanics and Physics of Solids*, **40** (2), 1992, pp.315-337.

Mollenhauer, D.; Ifju, P., and Han, B., "A Compact, Robust and Versatile Moiré Interferometer," *Optics and Lasers in Engineering*, **23**, 1995, pp. 29-40.

Moroso, J., Master of Science Thesis, University of Florida, 1999.

Nitz, A. & Nembach, E., "Anisotropy of the Critical Resolved Shear Stress of a  $\gamma'$  (47 vol. %)-Hardened Nickel-Base Superalloy and its Constituent  $\gamma$ - and  $\gamma'$ -Single-Phases," *Materials Science and Engineering*, A243-236, 1997, pp.684-686.

Rice, J.R., "Tensile Crack Tip Fields in Elastic-Ideally Plastic Crystals," *Mechanics of Materials*, **6**, 1987, pp.317-335.

Saeedvafa, M. and Rice, J.R., "Crack Tip Singular Fields in Ductile Crystals with Taylor Power-Law Hardening, II: Plane Strain," *Journal of the Mechanics and Physics of Solids*, **37** (6), 1989, pp.673-691.

Sass, V. and Feller-Kniepmeier, M., "Orientation Dependence of Dislocation Structures and Deformation Mechanisms in Creep Deformed CMSX-4 Single Crystals," *Materials Science and Engineering*, A245, 1988, pp.19-28.

Schulson, E. and Xu, Y., "Notch-Tip Deformation of  $\text{Ni}_3\text{Al}$  Single Crystals," *Materials Research Society Symposium Proceedings*, Vol. 460, 1997, pp.555-560.

Shield, T., "An Experimental Study of the Plastic Strain Fields near a Notch Tip in a Copper Single Crystal During Loading," *Acta Materialia*, **44** (4), 1996, pp.1547-1561.

Shield, T., "Microscopic Moiré Interferometry," Retrieved March 11, 2002 from the World Wide Web: <http://www.aem.umn.edu/people/faculty/shield/mm.html>.

Shield, T. and Kim, K., "Experimental Measurement of the Near Tip Strain Field in an Iron-Silicon Single Crystal," *Journal of the Mechanics and Physics of Solids*, **42** (5), 1994, pp.845-873.

Stouffer, D. and Dame, L., *Inelastic Deformation of Metals: Models, Mechanical Properties, and Metallurgy*, John Wiley & Sons, Inc.; 1996, pp.387-417.

Svoboda, J. and Lukáš, P., "Model of Creep in  $\langle 001 \rangle$ -Oriented Superalloy Single Crystals," *Acta Materialia*, **46** (10), 1998, pp.3421-3431.

Swanson, G. and Arakere, N., "Effect of Crystal Orientation on Analysis of Single-Crystal, Nickel-Based Turbine Blade Superalloys," *National Aeronautics and Space Administration-Marshall Space Flight Center Technical Publication*, February 2000, pp.1-63.

Xu, Y. and Schulson, E., "On the Notch Sensitivity of the Ductile Intermetallic  $\text{Ni}_3\text{Al}$  Containing Boron", *Acta Materialia*, **44**, 1996, p.1601.

Zhu, W.; Fort, D.; Jones, I., and Smallman, R., "Orientation Dependence of Creep of  $\text{Ni}_3\text{Al}$  at Intermediate Temperature," *Acta Materialia*. **46** (11), 1998, pp.3873-3881.

## BIOGRAPHICAL SKETCH

I was born in Phoenix, Arizona in 1978 and grew up in nearby Mesa. I was fortunate to live in the same place for nearly 18 years before I left to move cross-country to attend the United States Naval Academy. During my first four years of college and in the Navy I had the opportunity to travel many places, including Florida, California, Connecticut, Hawaii, Canada, Mexico, Spain, and Portugal. I received a B.S. in Ocean Engineering and a minor in Spanish, along with an opportunity to immediately pursue graduate school at the University of Florida. In May I will head to Pensacola, FL to return to the “real” Navy in flight school, to begin my career as a helicopter pilot.

I certify that I have read this study and that in my opinion it conforms to acceptable standards of scholarly presentation and is fully adequate, in scope and quality, as a thesis for the degree of Master of Science.

---

Nagaraj K. Arakere, Chairman  
Associate Professor of Mechanical  
Engineering

I certify that I have read this study and that in my opinion it conforms to acceptable standards of scholarly presentation and is fully adequate, in scope and quality, as a thesis for the degree of Master of Science.

---

John C. Ziegert  
Professor of Mechanical Engineering

I certify that I have read this study and that in my opinion it conforms to acceptable standards of scholarly presentation and is fully adequate, in scope and quality, as a thesis for the degree of Master of Science.

---

Fereshteh Ebrahimi  
Professor of Materials Science and  
Engineering

This thesis was submitted to the Graduate Faculty of the College of Engineering and to the Graduate School and was accepted as partial fulfillment of the requirements for the degree of Master of Science.

May 2002

---

Pramod P. Khargonekar  
Dean, College of Engineering

---

Winfred M. Phillips  
Dean, Graduate School

dislocation) mechanisms, and no crystal lattice rotation. Finite element analysis is capable of accounting for changing temperature effects. However, in order to simplify the model and collaborate more closely with the MSE department, the FEA applied material properties at a constant (room) temperature. The exclusion of microstructure has also been discussed. The last assumption, however, is valid for this elastic model; crystal lattice rotation generally requires a few percent strain in a single slip system to occur (Stouffer and Dame, 1996) and the load used here is extremely low. The FEA here assumes only elastic deformation, and seeks only elastic stress and strain trends rather than specific values at fracture. Future research can easily build from the current model to incorporate plasticity, as well as creep or other desired behaviors.